

UNIVERSIDAD POLITÉCNICA DE MADRID

**ESCUELA TÉCNICA SUPERIOR DE INGENIEROS
INDUSTRIALES**

**Multiscale modeling of the plastic behaviour in single crystal tungsten:
from atomistic to crystal plasticity simulations**

DOCTORAL THESIS

David Cereceda Señas

Ingeniero Industrial
by Universidad Politécnica de Madrid

2015

DEPARTAMENTO DE INGENIERÍA ENERGÉTICA

**ESCUELA TÉCNICA SUPERIOR DE INGENIEROS
INDUSTRIALES**

Multiscale modeling of the plastic behaviour in single crystal tungsten: from atomistic to crystal plasticity simulations

David Cereceda Señas

Ingeniero Industrial
by Universidad Politécnica de Madrid

Supervisors:

Dr. Jaime Marian de Diego

*Professor of Material Science and
Engineering*

University of California Los Angeles

Dr. José Manuel Perlado Martín

*Catedrático de Ingeniería Nuclear
Director Instituto de Fusión Nuclear*

Universidad Politécnica de Madrid

2015

**Tribunal nombrado por el Magfco. y Excmo. Sr. Rector de la Universidad
Politécnica de Madrid, el día ____ de _____ del 2015**

Presidente	Javier Segurado
Secretario	Antonio Rivera
Vocal	Maximo Victoria
Vocal	Marino Arroyo
Vocal	Mark Gilbert
Suplente	María José Caturla
Suplente	Javier Sanz

Opta a la mención de “Doctor Internacional”.

Realizado el acto de defensa y lectura de la tesis el día ____ de _____ del 2015 en la Escuela Técnica Superior de Ingenieros Industriales.

Calificación:

EL PRESIDENTE

LOS VOCALES

EL SECRETARIO

*“When you start on the way to Ithaca,
wish that the way be long,
full of adventure, full of knowledge.
The Laestrygonians and the Cyclopes,
Poseidon in his anger: do not fear them,
you’ll never come across them on your way
as long as your mind stays aloft, and a choice
emotion touches your spirit and your body.
To many Egyptian cities may you go
so you may learn, and go on learning, from their sages.
Keep Ithaka always in your mind.
Arriving there is what you are destined for.
But do not hurry the journey at all.
Better if it lasts for years,
so you are old by the time you reach the island,
wealthy with all you have gained on the way,
not expecting Ithaka to make you rich.
Ithaka gave you the marvelous journey.
Without her you would not have set out.
She has nothing left to give you now.
And if you find her poor, Ithaka won’t have fooled you.
Wise as you will have become, so full of experience,
you will have understood by then what the Ithakas mean.”*

Constatino Cavafis

Acknowledgements

During the journey of this PhD I have had the opportunity to learn, visit and work at outstanding research institutions, challenge myself when things were not going as I expected, travel around the world... but most importantly, I could meet people that one way or another helped me to write these lines today, both professionally and personally. Thank you all. It is not feasible to name everybody who has helped me in the course of this work but I would like to explicitly thank some of you.

My deepest gratitude goes to my advisors and mentors: Prof. José Manuel Perlado and Prof. Jaime Marian. The “grumete” is becoming a captain and your guidance has played a very important role in this progress. Manolo, GRACIAS for sharing with me the passion and conviction that I needed to start doing research, for your great enthusiasm, your emails from Japan, perpetual energy and valuable guidance in the distance during all these years. Jaime, GRACIAS for accepting me in your group after the CCMS summer school “cuando todavía me faltaba un hervor”, for all these years of great lessons, for being always available, for our instructive discussions, for your time and dedication, your confidence, your advice and for sharing with me the passion for the wind; I will never forget our sailing trip along the California coast.

During all these years I have had the opportunity to work at LLNL, UCLA, CCFE and MPIE where I was delighted to work with Maximo Victoria, Vasily Bulatov, Babak Sadigh, Tom Arsenlis, Tomas Oppelstrup, Sylvain Queyreau, Mark Gilbert, Dierk Raabe, Franz Roters, Martin Diehl, Giacomo Po and Nasr Ghoniem. Thank you all for your stimulating scientific discussions and good advice.

I am also indebted with Elena, Nuria, Marta, Karen, Lili and Charlene. Thank you for making our research groups more human, for your smiles and for being always ready to help during all these years.

I owe special acknowledgements to my officemates at Instituto de Fusion, LLNL and UCLA: Cj, Jesus, Nuria, Tuan, Marta and Nikhil. Thank you for our everyday conversations, support and very positive environment to work.

Living abroad has been an important challenge for me but it also gave me the opportunity to meet incredible people that are now friends. Thank you Celia, Jorge, Franck, Maude, Tomas, Antonio, Lucía, Luigi, Lucile, Chuchis, Sylvain, Annais, Jesus and Cj for all the adventures that we shared and for the future ones that are waiting for us. I

also want to extend my deepest and warmest gratitude to my family from California: Lesa, John and JJ.

Y ahora en español,

A vosotros que estáis a este lado del charco, GRACIAS por no perderme el rastro a pesar del tiempo y la distancia, por el tiempo compartido a través del skype, whatsapp y por recibirme siempre con los brazos abiertos al volver a casa. GRACIAS al foro, legendarios, Xis, Galilea, maraca, catecados y acompañados, pequeña alquimista, Andrea y Adrián, Carlos, Cris, Cheché y H. Alberto. Muy especialmente, a Ana y Sara, Cj, Andrea y Adrián, Escri y María; gracias por animaros a compartir conmigo unos días en California.

A pesar de estar casi al final, quiero dedicar esta tesis a mi familia: mis padres, mi hermana, mis abuelos y mi tía. Muy especialmente a mis padres, por vuestro incondicional apoyo, por no poder verme todos los días, por vuestras muestras de cariño, por vuestro ejemplo de vida y por compartir con vosotros tres de mis mejores semanas en California; nunca olvidaré aquel abrazo en Baker Beach.

Por último, GRACIAS a ti Celia, por ser sin ninguna duda el mayor descubrimiento y motivo de felicidad en estos años de investigación. Gracias por todo lo compartido y por lo que nos queda por compartir rumbo a Itaca.

Resumen

En una planta de fusión, los materiales en contacto con el plasma así como los materiales de primera pared experimentan condiciones particularmente hostiles al estar expuestos a altos flujos de partículas, neutrones y grandes cargas térmicas. Como consecuencia de estas diferentes y complejas condiciones de trabajo, el estudio, desarrollo y diseño de estos materiales es uno de los más importantes retos que ha surgido en los últimos años para la comunidad científica en el campo de los materiales y la energía.

Debido a su baja tasa de erosión, alta resistencia al sputtering, alta conductividad térmica, muy alto punto de fusión y baja retención de tritio, el tungsteno (wolframio) es un importante candidato como material de primera pared y como posible material estructural avanzado en fusión por confinamiento magnético e inercial. Sin embargo, el tiempo de vida del tungsteno viene controlado por diversos factores como son su respuesta termo-mecánica en la superficie, la posibilidad de fusión y el fallo por acumulación de helio. Es por ello que el tiempo de vida limitado por la respuesta mecánica del tungsteno (W), y en particular su fragilidad, sean dos importantes aspectos que tienen que ser investigados.

El comportamiento plástico en materiales refractarios con estructura cristalina cúbica centrada en las caras (bcc) como el tungsteno está gobernado por las dislocaciones de tipo tornillo a escala atómica y por conjuntos e interacciones de dislocaciones a escalas más grandes. El modelado de este complejo comportamiento requiere la aplicación de métodos capaces de resolver de forma rigurosa cada una de las escalas. El trabajo que se presenta en esta tesis propone un modelado multiescala que es capaz de dar respuestas ingenieriles a las solicitudes técnicas del tungsteno, y que a su vez está apoyado por la rigurosa física subyacente a extensas simulaciones atomísticas.

En primer lugar, las propiedades estáticas y dinámicas de las dislocaciones de tipo tornillo en cinco potenciales interatómicos de tungsteno son comparadas, determinando cuáles de ellos garantizan una mayor fidelidad física y eficiencia computacional. Las

grandes tasas de deformación asociadas a las técnicas de dinámica molecular hacen que las funciones de movilidad de las dislocaciones obtenidas no puedan ser utilizadas en los siguientes pasos del modelado multiescala. En este trabajo, proponemos dos métodos alternativos para obtener las funciones de movilidad de las dislocaciones: un modelo Monte Carlo cinético y expresiones analíticas. El conjunto de parámetros necesarios para formular el modelo de Monte Carlo cinético y la ley de movilidad analítica son calculados atomísticamente. Estos parámetros incluyen, pero no se limitan a: la determinación de las entalpías y energías de formación de las parejas de escalones que forman las dislocaciones, la parametrización de los efectos de no Schmid característicos en materiales bcc,etc.

Conociendo la ley de movilidad de las dislocaciones en función del esfuerzo aplicado y la temperatura, se introduce esta relación como ecuación de flujo dentro de un modelo de plasticidad cristalina. La predicción del modelo sobre la dependencia del límite de fluencia con la temperatura es validada experimentalmente con ensayos uniaxiales en tungsteno monocristalino. A continuación, se calcula el límite de fluencia al aplicar ensayos uniaxiales de tensión para un conjunto de orientaciones cristalográficas dentro del triángulo estándar variando la tasa de deformación y la temperatura de los ensayos. Finalmente, y con el objetivo de ser capaces de predecir una respuesta más dúctil del tungsteno para una variedad de estados de carga, se realizan ensayos biaxiales de tensión sobre algunas de las orientaciones cristalográficas ya estudiadas en función de la temperatura.

Abstract

Tungsten and tungsten alloys are being considered as leading candidates for structural and functional materials in future fusion energy devices. The most attractive properties of tungsten for the design of magnetic and inertial fusion energy reactors are its high melting point, high thermal conductivity, low sputtering yield and low long-term disposal radioactive footprint. However, tungsten also presents a very low fracture toughness, mostly associated with inter-granular failure and bulk plasticity, that limits its applications. As a result of these various and complex conditions of work, the study, development and design of these materials is one of the most important challenges that have emerged in recent years to the scientific community in the field of materials for energy applications.

The plastic behavior of body-centered cubic (bcc) refractory metals like tungsten is governed by the kink-pair mediated thermally activated motion of $\frac{1}{2} \langle 111 \rangle$ screw dislocations on the atomistic scale and by ensembles and interactions of dislocations at larger scales. Modeling this complex behavior requires the application of methods capable of resolving rigorously each relevant scale. The work presented in this thesis proposes a multiscale model approach that gives engineering-level responses to the technical specifications required for the use of tungsten in fusion energy reactors, and it is also supported by the rigorous underlying physics of extensive atomistic simulations.

First, the static and dynamic properties of screw dislocations in five interatomic potentials for tungsten are compared, determining which of these ensure greater physical fidelity and computational efficiency. The large strain rates associated with molecular dynamics techniques make the dislocation mobility functions obtained not suitable to be used in the next steps of the multiscale model. Therefore, it is necessary to employ mobility laws obtained from a different method. In this work, we suggest two alternative methods to get the dislocation mobility functions: a kinetic Monte Carlo model and analytical expressions. The set of parameters needed to formulate the kinetic Monte Carlo

model and the analytical mobility law are calculated atomistically. These parameters include, but are not limited to: enthalpy and energy barriers of kink-pairs as a function of the stress, width of the kink-pairs, non-Schmid effects (both twinning-antitwinning asymmetry and non-glide stresses), etc.

The function relating dislocation velocity with applied stress and temperature is used as the main source of constitutive information into a dislocation-based crystal plasticity framework. We validate the dependence of the yield strength with the temperature predicted by the model against existing experimental data of tensile tests in single-crystal tungsten, with excellent agreement between the simulations and the measured data. We then extend the model to a number of crystallographic orientations uniformly distributed in the standard triangle and study the effects of temperature and strain rate. Finally, we perform biaxial tensile tests and provide the yield surface as a function of the temperature for some of the crystallographic orientations explored in the uniaxial tensile tests.

Contents

Acknowledgements	v
Resumen	vii
Abstract	ix
Contents	xi
List of Figures	xv
List of Tables	xxi
Abbreviations	xxiii
Physical Constants	xxv
1 Introduction	1
1.1 Tungsten and tungsten alloys as candidates for fusion energy devices	1
1.2 Multiscale modeling in crystalline materials	4
1.2.1 A sequential multiscale model to study the plastic behavior of tungsten alloys	5
1.2.1.1 Interatomic potentials	6
1.2.1.2 Molecular statics	8
1.2.1.3 Molecular dynamics	9
1.2.1.4 Crystal plasticity	10
1.3 Dislocations	11
1.3.1 The concept of dislocation	11
1.3.2 The Burgers vector	13
1.3.3 Types of dislocations	14
1.3.4 Movement of dislocations in bcc crystals	14
1.3.4.1 Orowan's equation	16
1.3.4.2 Driving forces for screw dislocation motion	18

I ATOMISTIC SIMULATIONS	21
2 Assessment of interatomic potentials for atomistic analysis of static and dynamic properties of screw dislocations in tungsten	23
2.1 Introduction	23
2.2 Statical properties of interatomic potentials	25
2.3 Mobility of screw dislocations	29
2.3.1 Simulation setup	29
2.3.2 Techniques to accelerate convergence of stress-controlled MD simulations of dislocation motion	31
2.3.3 Results	36
2.4 Dislocation core structure at finite temperature	39
2.5 Impact of the dislocation core transition on dislocation mobility	46
2.6 Summary	48
3 Nudged Elastic Band simulations of kink pairs	49
3.1 Introduction	49
3.2 Computational details	51
3.3 Results	52
3.3.1 Enthalpy and Energy barriers	52
3.3.2 Kink-Pair Enthalphy	60
3.3.3 Kink-Pair Width	63
3.4 Summary	67
4 Atomistic simulations of non-Schmid effects in tungsten	69
4.1 The Schmid's law	69
4.2 The break down of Schmid's law in bcc crystals	72
4.2.1 Twinning/anti-twinning asymmetry	73
4.2.2 Non glide stresses	76
4.2.3 Projection tensor and non-Schmid effects	79
4.3 Parabolic and multiparametric implementation of the non-Schmid effects	81
4.4 Summary	83
II CRYSTAL PLASTICITY SIMULATIONS	85
5 Linking atomistic, kinetic Monte Carlo and crystal plasticity simulations of single-crystal tungsten strength	87
5.1 Introduction	87
5.2 Constitutive model	89
5.2.1 Dislocation velocity function	90
5.2.2 Dislocation density law	92
5.3 Simulation details	93
5.4 Results	94
5.5 Summary	99

6 Unraveling the temperature dependence of the yield strength in single-crystal tungsten using atomistically-informed Crystal Plasticity simulations	103
6.1 Introduction	103
6.2 Computational methods	106
6.2.1 Screw dislocation mobility law	107
6.3 Results	109
6.3.1 Yield criterion	110
6.3.2 Model validation and initial results	112
6.3.3 Uniaxial tensile tests	115
6.3.3.1 Dependence on temperature	115
6.3.3.2 Dependence on strain rate and strain rate sensitivity .	115
6.3.4 Biaxial loading tests and yield surfaces	118
6.4 Summary	121
III CONCLUSIONS	123
7 Conclusions	125
7.1 Conclusions of Part I	125
7.2 Conclusions of Part II	127
8 Publications and research activities	129
Bibliography	135

List of Figures

1.1	The illustration shows the cross-section of the torus of a tokamak. (1) The plasma-facing part of the blanket boxes – the so-called first wall. (2) The high heat flux cooling layout of the divertor. (3) The magnetic field lines which direct exhaust particles (mainly helium) to the divertor target plates (Rieth et al., 2013a)	2
1.2	Schematic representation of the sequential multiscale approach covered in this thesis.	5
1.3	(a) Burgers circuit round an edge dislocation with positive line sense into the paper, (b) the same circuit in a perfect crystal; the closure failure is the Burgers vector (Hull & Bacon, 1984).	13
1.4	(a) Burgers circuit round a screw dislocation with positive line sense in the direction shown, (b) the same circuit in a perfect crystal; the closure failure is the Burgers vector (Hull & Bacon, 1984).	15
1.5	Orientation of the {110} and {112} planes along the [1 1 1] zone (Hull & Bacon, 1984).	16
1.6	(a) A perfect crystal with simple cubic structure and dimension $L_x \times L_y \times L_z$. (b) The top surface is subjected to a traction force T_x while the bottom surface is fixed. An edge dislocation nucleates from the left surface. In (c) and (d) the dislocation moves to the right. In (e) the dislocation finally exits the crystal from the right surface. The net result is that the upper half of the crystal is displaced by \mathbf{b} with respect to the lower half (Bulatov & Cai, 2006)	17
1.7	A screw dislocation moving along the glide plane in a cubic crystal (Bulatov & Cai, 2006).	19
2.1	Peierls potential for all potentials tested here. DFT calculations from Ventelon <i>et al.</i> (Ventelon et al., 2013) are shown for comparison.	27
2.2	$(\bar{1}\bar{1}0)\gamma$ surface along the [111] direction for all the potentials considered in this work. DFT calculations from Ventelon <i>et al.</i> (Ventelon et al., 2013) are shown for comparison.	28
2.3	MD simulation setup.	30
2.4	Screw dislocation position as a function of time for a simulation at $T = 1500$ K and $\sigma = 1100$ MPa, both for the case of a step function and a linear function with a slope of 20 ps.	32
2.5	Screw dislocation velocity at $T=1200$ K using step function, linear function with $\theta = 10$ ps, and linear function with $\theta = 20$ ps.	33

2.6	Screw dislocation position as a function of time during a 300-ps simulation at 600K and 1400 MPa. Also shown is the evolution of the σ_{zx} component of the virial with time.	34
2.7	Percentage difference in screw dislocation velocity between step and linear stress function simulations. The data are plotted as a function of temperature and stress and the difference is computed as $(v_s - v_l)/v_l$	35
2.8	Screw dislocation velocity as a function of applied shear stress and temperature for the five interatomic potentials considered here. Note that the velocity and stress axes are not on the same scale for each case.	36
2.9	Line-averaged dislocation trajectories on the yz -plane for two combinations of σ and T and over 100 ps. Planes forming 0, 5, 15 and 30° with the $(11\bar{2})$ MRSS plane are represented with dotted lines (angles not to scale). Except for the TF-BOP potential, all the simulations yield small $<5^\circ$ deviations from MRSS motion.	38
2.10	Comparison of interatomic potentials for the data given in Fig. 2.8. The colored lines correspond to exponential fits obtained in Section 2.5 for potentials EAM1, EAM3 and MEAM.	40
2.11	Line-averaged dislocation trajectories on the yz -plane for the EAM3 potential at 500 MPa. Results for two 200-ps temperatures above and below the presumed core transformation temperature of around 1200 K are shown. Planes forming 0, 5, 15 and 30° with the $(11\bar{2})$ MRSS plane are represented with dotted lines (angles not to scale).	41
2.12	Time-averaged core structures for the five potentials tested here in the entire temperature range.	42
2.13	(a) Analysis of the favored core structure for the five different potentials as a function of temperature. A compact core is designated by a circle, and a non-compact by a diamond. The y -position of each point is the magnitude of distance of the inflection points in the 1NN string-interaction law (<i>i.e.</i> d^* , which is the distance at which $U_1''(d) = 0$) normalized to the quantity $b(T)/6$, where $b(T) = \sqrt{3}a(T)/2$. The dashed horizontal line separates the region of phase space where compact cores are favored (below) from the region where non-compact are favored (above). (b) The 1NN string-interaction law for EAM3 at 0 K. The red dashed vertical lines indicate the position of the inflection points in this curve. (c) Differential displacement map of the compact core predicted at 0 K for the U_1 function from EAM3. Each of the three strings closest to the core (red circles) are separated from their two closest secondary strings (blue circles) by $b/6$. In the figure the temperature dependence of b is omitted for the sake of clarity.	45
3.1	Position of the first d_1 and second d_2 dislocation with $(\bar{1}01)$ plane	51
3.2	Enthalpy barrier per Burgers vector for a straight screw dislocation with normal plane $(\bar{1}01)$, computed with the NEB method using the EAM potential under the full range of applied stress.	53
3.3	Energy barrier per Burgers vector for a straight screw dislocation with normal plane $(\bar{1}01)$ and EAM potential.	55

3.4	(a) Position of dislocations d_1 and d_2 when the screw is oriented with $(\bar{1}2\bar{1})$ as the normal plane. (b) Enthalpy barrier per Burgers vector for a straight screw dislocation with normal plane $(\bar{1}2\bar{1})$, computed with the NEB method using the EAM potential.	56
3.5	Energy barrier at 0 MPa for the $(\bar{1}01)$ and $(\bar{1}2\bar{1})$ planes versus the reaction coordinate in units of the glide direction, $[\bar{1}2\bar{1}]$ and $[10\bar{1}]$ respectively.	57
3.6	Enthalpy and energy barriers versus the reaction coordinate in units of the glide direction, $[\bar{1}2\bar{1}]$, for the MEAM potential.	58
3.7	Enthalpy barrier when the initial configurations of the intermediate replicas are straight dislocations, kink-pairs, and the resultant envelope of minimum enthalpy of this two cases for the EAM potential at 600 MPa.	59
3.8	Enthalpy barrier of the straight dislocation at 0 MPa and the envelope of minimum enthalpy for the full range of applied stress 0 - 1600 MPa and EAM potential.	61
3.9	Kink pair activation enthalpy as a function of stress. The data is fitted to the standard Kocks-Argon-Ashby expression that equals the energy of a pair of isolated kinks at zero stress and vanishes at $s = 1$ ($\tau = \sigma_p$).	62
3.10	Kink formation enthalpies as a function of the number of atoms per Burgers vector.	63
3.11	Atomistic visualization obtained via ovito (Stukowski, 2010) of different replicas along the final pathway of the NEB simulation at 1200 MPa.	64
3.12	Shape of kink pair for replica number 14 of the reaction pathway at 1200 MPa.	66
3.13	Shape of several replicas from the final pathway of the NEB simulation when applying 1200 MPa.	67
3.14	Kink pair width as a function of the applied stress.	68
4.1	Geometry of dislocation slip in crystallite materials. In general $(\phi + \lambda) \neq \pi/2$ (Hull & Bacon, 1984).	70
4.2	Schmid factor for 231 equally-spaced loading directions along the standard triangle. 5.3a represents the the slip family with maximum Schmid factor. 5.3b represents the envelope of maximum Schmid factor colored in red.	71
4.3	Schematic view of the glide planes of the $[111]$ axis zone. The orientation of the MRSSP is defined by the angle χ that it makes with the $(\bar{1}01)$ plane. The suffixes ‘T’ and ‘AT’ refer to the twinning and antitwinning senses, respectively.	71
4.4	Arrangement of atoms for a bcc lattice in planes with normal $[111]$	73
4.5	Dependence of the CRSS on the orientation of the MRSSP, i.e. angle χ , when applying shear stress parallel to the slip direction in the MRSSP.	75
4.6	(a) Dependence of the CRSS on the orientation of the MRSSP, i.e. angle χ , when applying pure shear stress τ (circles) and a combination of shear stress and non glide stresses σ in tension (down-triangles) and compression (up-triangles). (b) Compression loading scheme. (c) Tension loading scheme.	77

4.7	Crystallographic diagram of the [111] zone in the bcc lattice with each {110} and {112} clearly labeled. The picture also shows a mapping of the [111] zone to a schematic atomistic box containing a screw dislocation subjected to shear and nonglide stresses according to Vitek's convention. The glide n^α , auxiliary n_1^α and MRSS planes are labeled in each case. A [101] glide plane corresponds to $\alpha = 2$ in our CP calculations.	78
4.8	Stress projection factor P_{tot} for 231 uniformly-distributed crystallographic loading orientations in the standard triangle when $\langle 111 \rangle\{110\}$ slip systems are active. Three different scenarios are studied: (i) Schmid law, (ii) non-Schmid effects including only T/AT asymmetry, (iii) non-Schmid effects including both T/AT asymmetry and non glide stresses.	80
4.9	Dependence of the CRSS on the non glide stress perpendicular to the slip direction. In agreement with Fig.4.6, positive and negative values are assigned to compression and tension loading, respectively. The CRSS is also plotted at different orientations of the MRSSP, i.e. angle χ , in the twinning (T) and antitwinning (AT) regions.	82
4.10	Surface plot that captures the simultaneous dependence of the CRSS on both the orientation of the MRSSP, i.e. angle χ , and the non glide stress σ . The surface defined by eq. 4.23 is also plotted.	83
5.1	Predictor-corrector scheme to calculate the stress \mathbf{S} as a function of \mathbf{F}	93
5.2	Schematic diagram of the multiscale approach that links atomistic, kinetic Monte Carlo and crystal plasticity simulations. In step I we use semiempirical interatomic potentials to calculate the energetic of single dislocation motion. In step II we use kMC parameterized with atomistic data to fit a mobility function to the velocity vs. stress vs. temperature. Finally, in step III, we use those mobility functions to characterize the velocity gradient in CP.	94
5.3	Discretization of the standard triangle into a regular grid of 231 points representing different crystallographic orientations. 5.3a represents the the slip family with maximum Schmid factor. 5.3b shows the three dimensional surface of the Schmid factor. The envelope of maximum Schmid factor is colored coded according to Fig.5.3a.	97
5.4	Mechanical response of bcc W single crystal predicted by our constitutive model under conditions of uniaxial tension along different loading directions and slip systems. The stress-strain behavior is represented using the components of the <i>first Piola-Kirchoff stress</i> and the <i>Biot strain</i> along the loading direction z . Parameters from Table 5.2 are taken for (a) Schmid behavior and (b) non-Schmid behavior.	97
5.5	Temperature dependence of yield strength for different tensile loading orientations and active slip systems. 5.5a represents Schmid behavior and 5.5b represents non-Schmid behavior.	98
5.6	Loading directions corresponding to the five highest and lowest values of yield strength for uniaxial tensile tests at 300, 750 and 1200 K. The biggest blue circle represents the absolute minimum and the biggest red circle represents the absolute maximum.	99

5.7	Yield strength for uniaxial tensile tests along 231 uniformly distributed crystallographic orientations in the standard triangle at different temperatures. Schmid and non-Schmid behaviors are studied separately. $\{1\bar{1}0\}\langle111\rangle$ and $\{112\}\langle111\rangle$ slip systems are active. Fig. 5.7c represents the percentage difference between non-Schmid and Schmid.	100
6.1	Schematic depiction of a kink pair on a screw segment of length λ lying on a slip plane n^α (of the $\{110\}$ family). The vertical axis represents the potential energy, with the Peierls potential clearly marked. The dashed line represents the initial equilibrium line position.	108
6.2	Evolution of the stress P_{zz} with deformation B_{zz} during a CP simulation of a uniaxial tensile test with $[101]$ loading orientation (as depicted in the standard triangle). The first and second derivatives of the stress w.r.t. to the strain are also plotted to illustrate the method of identification of the yield point according to this criterion. Also shown is the intercept of the curve with the 0.2% strain offset criterion line.	111
6.3	Yield strength of W single crystals at the conditions used by Argon & Maloof (1966a) in tensile deformation tests under two different loading orientations. The experimental data is shown for comparison. The inset shows the results of CP calculations with different contributions of the projection tensor activated.	113
6.4	Yield strength of W single crystals under the conditions used by Brunner (2010) in uniaxial tensile tests. The experimental data is shown for comparison. The inset shows the results of CP calculations with different contributions of the projection tensor activated.	114
6.5	Contour maps of the yield strength from uniaxial tensile test simulations for 231 uniformly distributed crystallographic orientations in the standard triangle at different temperatures. Note that each map has its own distinct numerical scale to aid in the visualization of hard and soft regions.	116
6.6	Temperature path of the softest and hardest yield directions on the standard triangle as a function of strain rate.	117
6.7	(a) Stress-strain relations at three different strain rates and $T = 300$ K for a $[101]$ loading orientation. (b) Temperature dependence of the yield strength for the softest and hardest directions as a function of strain rate.	117
6.8	Dependence of yield strength with strain rate for loading along direction $[101]$ as a function of temperature. The inset represents the dependence of the strain rate sensitivity exponent m with temperature.	118
6.9	Yield curve for loading along directions $\mathbf{l}_y = [111]$ and $\mathbf{l}_z = [11\bar{2}]$ as a function of temperature.	120
6.10	Yield surface at 300 K for biaxial loading along directions belonging to the $[111]$ zone. By symmetry, only the 60° -arc need be explored.	120

List of Tables

2.1	Properties of potentials used: lattice parameter a_0 , shear modulus μ , Peierls stress σ_P , computational cost, core structure at 0 K, and thermal expansion coefficient α . Potentials EAM1, EAM2 and TF-BOP display a threefold symmetric (degenerate) core, while EAM3 and MEAM predict compact (non-degenerate) cores. The values of the volumetric thermal expansion coefficients, α , are used in Section 2.4.	26
2.2	Fitting parameters for the analytical mobility function 2.1. The average fitting error for A , H_0 , and V^* was, respectively, 6, 9 and 10%. Regular script: values from full temperature fits; bold script: values from low temperature (≤ 900 K) fits; in parentheses: percentage difference between both sets of fits.	47
5.1	CP constitutive models for bcc metals.	89
5.2	Fitting parameters of the mobility function defined in eq. 5.5 (obtained from (Stukowski et al., 2015)).	95
5.3	List of parameters for the constitutive model. The last row represents the six coefficients of the interaction matrix.	95
6.1	List of parameters and functional dependences for fitting the CP model. All of these parameters have been obtained using dedicated atomistic calculations. The parameter s represents the normalized shear stress: $s = \frac{\tau'^\alpha}{\sigma_P}$	109

Abbreviations

W	tungsten
bcc	body-centered cubic
BOA	Born-Oppenheimer approximation
MS	Molecular Statics
SD	steepest-descend
CG	conjugate-gradient
NR	Newton-Raphson
MD	Molecular Dynamics
kMC	kinetic Monte Carlo
CP	Crystal Plasticity
FEM	Finite Element Method
FFT	Fast Fourier Transform
b	Burgers vector
T/AT	Twinning/Anti-Twinning
NEB	Nudged Elastic Band
EAM	Embedded Atom Method
MEAM	Modified Embedded Atom Method
TB-BOP	Tight-Binding-based Bond Order Potential
MEP	Minimum Energy Path
DFT	Density Functional Theory
CRSS	Critical Resolved Shear Stress
MRSSP	Maximum Resolved Shear Stress Plane

Physical Constants

$$eV = 1.60212 \times 10^{-19} \text{ J}$$

$$\begin{aligned} \text{Boltzmann's constant } k_B &= 1.3807 \times 10^{-23} \text{ J / K} \\ &\quad 8.6173 \times 10^{-5} \text{ eV / K} \end{aligned}$$

$$\begin{aligned} \text{Planck's constant } h &= 6.6261 \times 10^{-34} \text{ J · s} \\ &\quad 4.1357 \times 10^{-15} \text{ eV · s} \end{aligned}$$

Chapter 1

Introduction

1.1 Tungsten and tungsten alloys as candidates for fusion energy devices

The cross-section of the torus of a tokamak, one of the two engineering designs suggested for magnetic fusion energy devices, is represented in Fig.1.1. Blanket boxes are used to cover most of its inner surface, transfer the energy of the neutrons released during the fusion reactions and produce tritium by neutron activation of lithium. The existence of peaks and off-normal events during the operation of the tokamak suggest the addition of a protective layer called *first wall* to avoid damage on the plasma facing surface of these blanket boxes. In order to maintain the plasma confined in a stationary regime the efficiency of the process can not be affected by the presence of products generated in previous nuclear fusion reactions. To make this possible, hydrogen isotopes, helium particles and impurities have to be redirected from the plasma to cooled target plates called *divertors* that operate as an exhaust system. These targets are situated near the intersection of the magnetic field lines. The high-energy plasma particles hit the components of the divertor creating sputtering and transforming their kinetic energy into extremely intense heat fluxes. These conditions make divertors the highest thermally loaded components of a fusion power plant (Rieth et al., 2013a).

Tungsten and tungsten alloys are being considered as leading candidates for first wall, plasma facing and structural divertor materials in magnetic fusion energy devices (Bolt et al., 2002; Hirai et al., 2009; Maisonnier et al., 2007; Norajitra et al., 2008; Pamela et al., 2009; Wittlich et al., 2009). Inertial fusion energy devices also study them as

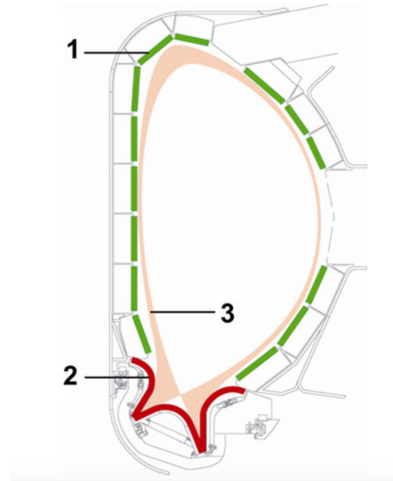


FIGURE 1.1: The illustration shows the cross-section of the torus of a tokamak. (1) The plasma-facing part of the blanket boxes – the so-called first wall. (2) The high heat flux cooling layout of the divertor. (3) The magnetic field lines which direct exhaust particles (mainly helium) to the divertor target plates ([Rieth et al., 2013a](#)).

candidates for first-wall armour materials ([Sethian et al., 2010, 2005](#)). The most attractive properties of tungsten for these applications are its high melting point, high thermal conductivity, low sputtering yield and low long-term disposal radioactive footprint ([Lassner & Schubert, 1999](#)). Ductility within the operation temperature range is one of the requirements for a structural material, while compatibility with the plasma-wall interactions ([Roth et al., 2009](#)) and high crack resistance under extreme thermal operation conditions are both requirements for armour materials ([Hirai et al., 2009; Wittlich et al., 2009](#)). Due to the nature of fusion nuclear reactions, stability with respect to high neutron fluxes and high helium production rates is also one of the desired properties for both type of materials¹.

Detailed reviews of the tungsten program for inertial and magnetic fusion technologies can be found in the literature ([Rieth et al., 2011, 2013a,b; Sethian et al., 2010, 2005; Wurster et al., 2013](#)). The purpose of this section is to give an overview of the current research status on the tungsten material program for fusion applications, with special interest on the existing limitations for its use as a structural material. The main requirements of tungsten materials for structural divertor applications comprise properties like

¹Irradiation effects in tungsten are not studied in this thesis. We are aware that they play an important role in the evolution of the properties of the materials, but even without these effects, there are still unsolved mechanical problems related to the use of tungsten and tungsten alloys for these applications.

high thermal conductivity, high temperature strength and stability, high recrystallization temperature, and enough ductility for an operation period of about two years under enormous neutron load ([Rieth et al., 2013a](#)). Among these requirements, the brittleness of tungsten materials is the main constrain for their use as structural materials. Moreover, in the presence of neutron irradiation the ductile-to-brittle transition temperature (DBTT) can be shifted to the range of several hundreds degrees. Then, the most limiting question to answer is: How can DBTT be significantly decreased? Three different approaches have been suggested for this purpose: alloying/solid solution, nanostructuring, and producing composite materials. The most common alloys for tungsten ductilisation include transition metals from groups IV, V, VI and VII like tantalum, vanadium, molybdenum, titanium and rhenium. Charpy tests in the temperature range of 400–1100 °C (in vacuum) have shown that compared to pure tungsten the DBTT of most alloys is higher, i.e. they are more brittle; only rhenium is known to improve the ductility of tungsten by solid solution. Nanostructuring of tungsten and tungsten alloys by severe plastic deformation like high pressure torsion has been investigated in the past but these processes are not suitable for producing industrial-scale semi-finished products. Chemical powder metallurgical methods have also been used as an alternative route to fabricate nanostructured tungsten-based materials with results extremely uniform with respect to morphology as well as composition but the process to limit grain growth need some further investigation. Tungsten composites can be obtained when the brittle tungsten matrix is reinforced by short fibres of tantalum. Since tantalum is more ductile than tungsten it can therefore divert or stop cracks propagating in the tungsten matrix. Another type of composites to improve fracture toughness consider tungsten laminate material which is fabricated from tungsten foils brazed by copper ([Rieth et al., 2013a](#)).

It is still not clear what are the most promising strategies to increase ductility in tungsten materials. In this context, this thesis is focused on the study of the mechanical properties in pure tungsten, from atomistic to engineering level scales. Based on this multiscale knowledge in pure tungsten the final goal is to provide enough information to find new strategies that could increase ductility in tungsten materials.

1.2 Multiscale modeling in crystalline materials

A problem in science is considered to be “multiscale” when it involves phenomena at different length and/or time scales covering several orders of magnitude. More importantly, all these phenomena involved in the problem play key roles in the behavior studied, so that we cannot correctly formulate the model without explicitly accounting for these different scales.

Egon Orowan suggested in 1944 a visual example to justify the interest on the multiscale nature of physical problems when he compared the working of a pocket watch and the complex mechanisms underlying the well known uniaxial tensile test ([Orowan, 1944](#)). In that work Orowan states: “The tensile test is very easily and quickly performed, but it is not possible to do much with its results, because one does not know what they really mean. They are the outcome of a number of very complicated physical processes taking place during the extension of the specimen. The extension of a piece of metal is, in a sense, more complicated than the working of a pocket watch, and to hope to derive information about its mechanism from two or three data derived from measurements during the tensile test is perhaps as optimistic as would be an attempt to learn about the working of a pocket watch by determining its compressive strength”. In other words, what Orowan is trying to say is that studying a material from only the largest of scales is like studying a pocket watch with only a hammer; neither method will likely show us why things behave as they do. Instead, we need to approach the problem from a variety of observational and modeling perspectives and scales.

Multiscale approaches can be classified into two groups depending on the procedure they use to integrate the methods and scales embedded in the model. These two broad categories are: *sequential* and *concurrent*. Sequential multiscale approaches integrate the fine-scales and coarse-scales models independently in the sense that the fine-scale model is no longer required after providing the initial information to the coarse-scale model. In these approaches, fine-scale simulations are viewed as a ”pre-processing step”, generating for example parameters that are needed to complete the governing equations in the coarse-scale model. On the other hand, in concurrent approaches the models are integrated simultaneously at two or more length (or time) scales. Concurred approaches can also be classified into two sub-categories based on the methodology they use to study the physical problem. In partitioned-domain concurrent approaches, the system is divided into two or more regions, and fine-scale or coarse-scale models are used to study each region. In hierarchical concurrent approaches, the system is not

divided into regions and both fine-scale and coarse-scale models are used everywhere (Tadmor & Miller, 2011).

1.2.1 A sequential multiscale model to study the plastic behavior of tungsten alloys

Fig. 1.2 summarizes the structure of the sequential multiscale model presented in this thesis. Each block represents different scales that are going to be discussed in more detail in the following chapters. These blocks used to build the multiscale approach are:

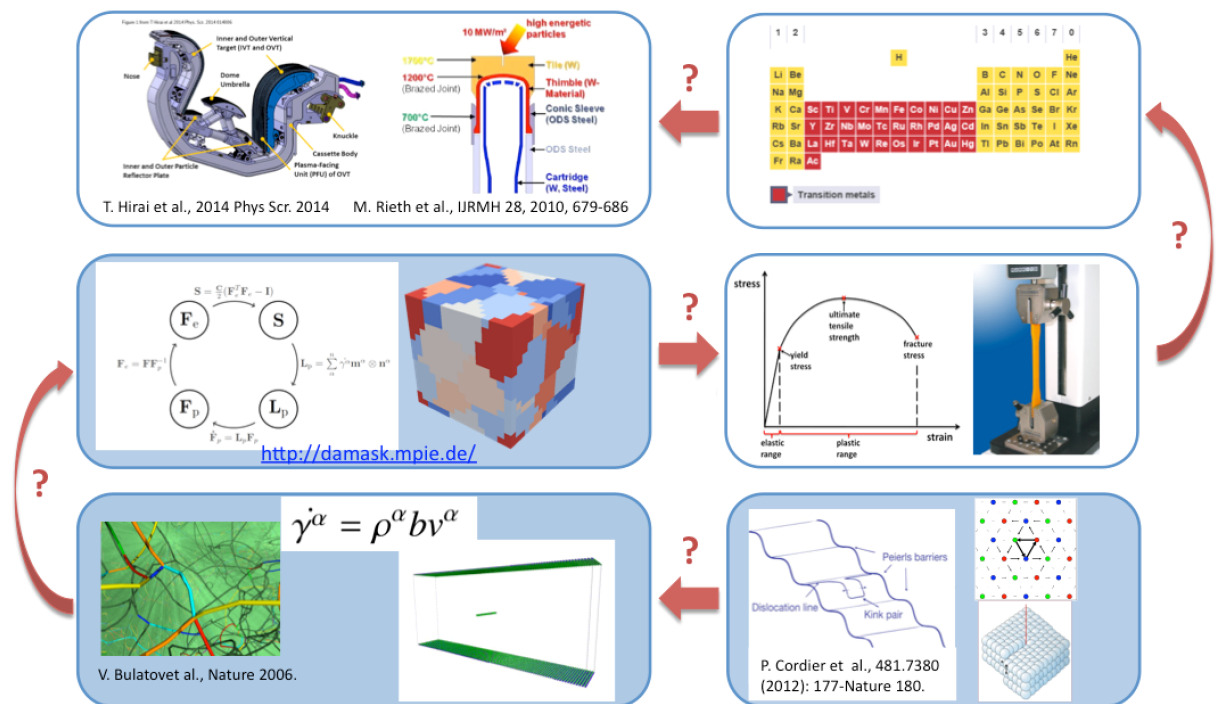


FIGURE 1.2: Schematic representation of the sequential multiscale approach covered in this thesis.

1. The main goal of this multiscale approach is to obtain engineering level responses to the technical specifications given by the design of the components. In this case for fusion energy devices, the design specifications of the divertor are high thermal fluxes, temperatures, irradiation damage, etc.

2. With these boundary conditions and based on the well known general properties of materials a group of chemical components are selected as potential candidates.
3. Applying a variety of loading conditions the stress-strain behavior can be obtained, filtering the candidates with a most favorable response.
4. The material is divided in grains and its plasticity is studied by looking at different measures of stress and strain.
5. Plastic deformation in crystalline metals is governed by dislocations, martensite transformation and mechanical twinning. Among these contributions dislocations are the most important lattice defects and they are usually the main carriers of plastic deformation. In particular, the plastic behavior of body-centered cubic (bcc) metals like tungsten is governed by the motion of $\frac{1}{2} \langle 111 \rangle$ screw dislocations, the dominant mechanism in the slip process, so it is needed to look at this level to understand better the plasticity of each of the grains in the material.
6. Finally, it is needed a set of atomistic parameters to define properly the density and velocity of the dislocations.

Even though the formulation of the problem goes from top to bottom the sequential multiscale model presented in this thesis is built from the bottom, from atomistic calculations, to the top, to the engineering level responses. Below follows a brief description of each of these blocks, more or less thoroughly utilized in this thesis. Excellent reviews on this models and methods can be found in the literature ([Frenkel & Smit, 2001](#); [Roters et al., 2011, 2010](#); [Tadmor & Miller, 2011](#)).

1.2.1.1 Interatomic potentials

One of the main consequences of the Born-Oppenheimer approximation (BOA) ([Born, 1927](#)), which states that the electronic and nuclei motion in a molecule can be separated, is that the Hamiltonian for the nuclei does not depend directly on the electrons and then the effect of the electrons can be included in a single potential energy function U that only depends of the positions of the nuclei \mathbf{r} , $U = U(\mathbf{r})$. Moreover, if the *de Broglie thermal wavelength*² is much smaller than the average interatomic spacing, the nuclei can be treated as classical particles and then the potential field $U(\mathbf{r})$ becomes a classical

²The *de Broglie thermal wavelength* is defined as $\Lambda = \frac{h}{\sqrt{2\pi m k_B T}}$, where m is the mass of the particle, T the temperature, h is the Planck's constant and k_B is Boltzmann's constant.

interatomic model $V(\mathbf{r})$. This potential energy of the system V can be partitioned into an internal contribution V^{int} and a external contribution V^{ext} . The external potential energy V^{ext} takes into account the effects of external fields and contact with atoms outside the system, while the internal potential energy V^{int} , commonly called the *interatomic potential energy*, considers only the short-range interactions between the atoms in the system and it can be defined as the potential energy of the system when there are no other atoms outside it and when the system is also isolated from external fields. Since the interatomic potentials are the result of an approximation, their formulation always include parameters that need to be fitted to some reference values. The formulation of the interatomic potential and its accuracy to describe the interactions between the atoms in the system play a key role in the results of the atomistic and multiscale simulations.

A first broad group of interatomic potentials are called *cluster potentials* because they formulate the potential energy of a system of N atoms as a series of n-body terms, each of which depends on the positions of a cluster of n atoms. Pair potentials are examples of this category, and they formulate the internal potential energy as

$$V^{int} = \frac{1}{2!} \sum_{\substack{\alpha, \beta \\ \alpha \neq \beta}} \phi_{\alpha\beta}(r^{\alpha\beta}) \quad (1.1)$$

where α and β are the two species of atoms existing, $r^{\alpha\beta}$ is the distance between the particles and $\phi_{\alpha\beta}$ is the potential function. The most common and used pair potential is the *Lennard-Jones potential*, which is only physically realistic for studying solidified ideal gases. An example of cluster potential to study ionic crystals is the *Born-Mayer potential*. When modeling materials with strong covalent-bonding character cluster potentials that include third and/or fourth body interactions are needed. However, cluster potentials are not efficient when the bonding in the material is such that the series of n-body terms converges far more slowly.

A second broad group of interatomic potentials are called *functionals*, and they can also be subdivided into two categories: *pair functionals* and *cluster functionals*. Pair functionals represent the simplest method of incorporating an environmental dependence into the strength of each bond and they can be formulated to have a computational cost similar to pair potentials but being a more accurate for the case of simple metals. Examples of these pair functionals are the *embedded atom method (EAM) potentials* and the *Finnis-Sinclair potential*. The most general formulation of the empirical atomistic models are the cluster functionals, because they can depend on groups of three or more

atoms through any general functional dependence. Examples of these cluster functionals are the *Bond order potential* and the *modified embedded atom method (MEAM) potentials* among others.

A detailed description of the BOA, its implications and the formulation of different types of interatomic potentials can be found in Chapter 5 of the book “Modeling materials: continuum, atomistic and multiscale techniques” from Tadmor and Miller ([Tadmor & Miller, 2011](#)).

1.2.1.2 Molecular statics

Molecular statics (MS) is a computational method used to explore the energy landscape defined by a given atomistic model. Acquiring knowledge about these potential energy landscapes can help to understand different phenomena in materials science. Finding equilibrium structures through energy minimization, or finding saddle points and transition paths between two local energy minima are some of the main goals to achieve when exploring the potential energy landscape.

The purpose of energy minimization is to find stable structures of materials at 0 K. It is based on the fact that a particle is in equilibrium when the forces acting upon it are zero. The generalization of this result for N particles in three dimensions is that the equilibrium structure can be found by all the forces on all the atoms. However, the process of finding confidently and quickly local and global minima in a $3N$ dimensional energy landscape is one of the great open challenges in computational mathematics. The most commonly used methods in the field of energy minimization are: the steepest-descent (SD) method, the conjugate-gradient (CG) method and the Newton Raphson (NR) method.

The SD method is one of the simplest algorithms of minimizing a $3N$ dimensional function and it is a good choice when concerned with reliability than speed. Due to its lack of memory from previous steps this algorithm could generate an inefficient zig-zag tendency through the parameter space and may require many iterations to converge on a minimum. As its own name suggests, the idea is to choose the search direction at each iteration to be the steepest “downhill” direction along the direction of the forces at that particular point in the energy landscape.

The CG and NR methods are frequently called “local” minimization methods since there is no guarantee that the minimum located is the global minimum. These methods retain

a limited memory of previous iterations and therefore they are more efficient than the SP. Some of the differences between these “local” minimization methods come from the source of information they use. While the CG algorithm works using only information about the energy and the forces, the NR method utilizes the stiffness matrix or Hessian of the system (i.e. the second derivative of the energy with respect to the independent variables) or an approximation to it. In atomistic systems, the computational cost associated with the second order derivatives often makes methods like CG that only require first order derivatives more suitable. However, the rapid convergence of NR algorithms makes them more convenient in other situations where the stiffness matrix is relatively easy to compute and store.

1.2.1.3 Molecular dynamics

“Molecular dynamics (MD) is a method to simulate the simultaneous motion of a set of interacting atoms or molecules governed by their mutual interactions. In MD the evolution of a system of atoms is governed by classical Newtonian mechanics, so for each atom i in the system the following equation must be solved:

$$m_i \frac{d^2 r^i}{dt^2} = f_i = -\nabla_{r_i} \phi \quad (1.2)$$

where m_i is the mass, r^i is the position vector and f_i is the force on atom i . The atomic forces f_i are calculated as the negative gradient of the effective potential ϕ . Interacting particles (atoms in our case) are enclosed in the simulation box (which represent a piece of matter) and initial conditions including coordinates and velocities have to be set in order to initiate the simulation procedure. The velocities and the coordinates of the atoms at any subsequent moment of time can be obtained by solving the above-mentioned second-order differential equations 1.2 for all of the atoms in the simulation box. An MD simulation requires therefore a proper integration scheme, which must be numerically stable on the one hand and computationally efficient on the other.

Each iteration corresponds to a certain increment of time called *time step*. During this time nothing is known about motion of particles in the system. The corrector is needed to guide the conservation of the total energy and hence the convergence of the calculations. But even with the application of the corrector, if the time step is too large, a leakage or an injection of total energy can occur. Thus, the choice of the time step is delicate. On the one hand it must not be too large, because of the above-mentioned

problem, on the other, if it is too small the computing time needed to reach a meaningful simulation time becomes proportionally longer. The use of a variable time step is a frequent procedure to optimize the computing time, based on the idea that the time step can increase in equilibrium situations and must decrease to deal with situations out of equilibrium.

In MD, the system to be studied is represented by a virtual simulation box, in which all of the interacting atoms are enclosed. The atoms located near the boundary of the simulation box are specially treated by applying additional conditions. To perform physically meaningful simulations in the bulk and save computational time periodic boundary conditions (PBC) are used in all directions. The boundary of the simulation box in this case is not a real interface between atoms and vacuum, but rather an edge between the simulation cell and its image. However, when using this approach to simulate situations out of equilibrium, the size of the box must be big enough to prevent an effect of overlapping and self-interaction via PBC, which may lead to incorrect results.

In general MD is able to simulate trajectories in different statistical ensembles. The *microcanonical ensemble* (N, V, E), where the number of particles N , the volume V and the energy E of the system are conserved is the system 'naturally' simulated by MD. The *canonical ensemble* (N, V, T), where the number of particles N , the volume V and the temperature T of the system are conserved, can be simulated, provided that algorithms to control temperature are used. The *isothermal-isobaric ensemble* (N, P, T) where the number of particles N , the pressure P and the temperature of the system are conserved, can also be simulated with adequate algorithms" ([Terentyev, 2006](#)).

1.2.1.4 Crystal plasticity

The mechanically anisotropic nature of crystalline materials makes their deformation a process that depends on the direction of the mechanical loads and boundary conditions imposed. The first reason for this behavior is the anisotropy of the elastic tensor and second, the orientation dependence of the crystallographic deformation mechanisms activated (dislocations, twins and martensitic transformations).

The first attempts found in the literature to describe anisotropic plasticity under simple boundary conditions considered the importance of the anisotropic nature of mechanisms that can create shear and the possibility of different orientations of the crystal(s) with respect to the boundary conditions applied. Examples of these approaches are given

by Sachs ([Sachs, 1928](#)), Taylor ([Taylor, 1938](#)), Bishop-Hill ([Bishop & Hill, 1951a,b](#)) and Kroner ([Kroner, 1961](#)). However, these early approaches can not be applied to study possible interactions between individual grains of the polycrystal nor to analyze more complex internal or external boundary conditions since they are constructed using assumptions that simplify the stress and/or strain homogeneity existing in a polycrystal. To overcome these limitations, variational methods in the form of finite element approximations were formulated. These methods, commonly called *crystal plasticity finite element (CPFE) methods*, are based on the variational solution of the equilibrium of the forces and the compatibility of the displacements using a weak form of the principle of virtual work in a given finite-volume element. The fundamental step in these crystal plasticity (CP) models is the formulation of the velocity gradient in a dyadic form because it captures the tensorial crystallographic nature of the underlying defects that lead to shear and, consequently, to both shape changes and lattice rotations.

In this context it is important to emphasize the difference between a method and a model. A method is generally understood as a numerical or mathematical procedure, while a model frequently includes some physics. In particular, in the field of solid mechanics a model comprises the geometry, the mechanical boundary conditions and most important, a type of material model as crystal plasticity. Therefore, the finite element method (FEM) itself is just one of the numerical methods to solve nonlinear partial differential equations. In fact, there are more alternatives for solving the system of nonlinear partial differential equations resulting from compatibility and static equilibrium for the same CP model. One of these alternatives is for example the *Spectral method*, initially formulated by Moulinec and Suquet ([Moulinec & Suquet, 1994, 1998](#)) and recently extended by Lebensohn ([Eisenlohr et al., 2013](#); [Lebensohn, 2001](#); [Lebensohn et al., 2012](#)). This spectral method operates in fourier space and is very efficient compared to FEM due to the repetitive use of a fast fourier transforms (FFT) as part of an iterative solution algorithm.

1.3 Dislocations

1.3.1 The concept of dislocation

In the early part of the twentieth century two puzzles towered over the field of plastic deformation of crystallite materials:

- The stress required to deform plastically a crystal is much less than the stress one calculates from considering a defect-free crystal structure.
- Materials work-harden: when a material has been plastically deformed it subsequently requires a greater stress to deform further.

The concept of *dislocation* was postulated independently by Orowan ([Orowan, 1934a,b,c](#)), Taylor ([Taylor, 1934a,b](#)) and Polanyi ([Polanyi, 1934](#)) in 1934 as a response to these two key observations. The existence of dislocations was experimentally verified in 1947. It took another ten years before electron microscopy techniques were advanced enough to show dislocations moving through a material.

In 1926, Frenkel constructed a model to estimate the strength of a perfect crystal in shear ([Frenkel, 1926](#)). According to this model, i.e. in the absence of dislocations, the process of slide between two adjacent planes in a perfect crystal would be a rigid co-operative movement of all the atoms in one plane from the initial position to the next one in the perfect lattice. The shear stress required to move the atoms of one plane in this way is given by the sinusoidal relation:

$$\tau = \frac{\mu b}{2\pi a} \sin\left(\frac{2\pi x}{b}\right) \quad (1.3)$$

where τ is the applied shear stress, μ is the shear modulus, b the spacing between atoms in the direction of the shear stress, a the spacing of the rows of atoms and x is the shear translation of the two rows away from the low-energy equilibrium position.

The maximum value of τ , which represents the theoretical critical shear stress that a crystal can sustain before exhibiting permanent deformation is:

$$\tau_{th} = \frac{b}{a} \frac{\mu}{2\pi} \quad (1.4)$$

with a and b being, in general, nearly equal, so that $\tau_{th} \approx \mu/2\pi$. This value is many orders of magnitude larger than the experimental values of the resolved shear stress for slip measured in real crystals, commonly in the range between $10^{-4}\mu$ and $10^{-2}\mu$.

In 1934, Orowan, Taylor and Polanyi suggested a concept that reunifies experimental and theoretical values of the applied shear stress required to deform plastically a single crystal. Their suggestion was that there are defects inside the real crystals which

served as stress concentrations facilitating plastic flow. The nucleation, interaction and multiplication of these defects should explain hardening. The basic idea postulated was described in one of the publications from Taylor ([Taylor, 1934b](#)): "It seems that the whole situation is completely changed when the slipping is considered to occur not simultaneously over all atoms in the slip plane but over a limited region, which is propagated from side to side of the crystal in a finite time". Then a *dislocation* was defined as the defect separating the slipped region from the unslipped region in the crystal.

1.3.2 The Burgers vector

The *Burgers vector* is one of the most important properties of a dislocation, and it represents the magnitude and direction of the lattice distortion resulting from the presence of a dislocation in the crystal lattice. Two circuits need to be made to determine the Burgers vector associated with a dislocation. First, an atom-to-atom close loop is taken in a crystal containing dislocations with each step of the circuit connecting lattice sites that are fully coordinated. If the same atom-to-atom sequence is made in a perfect crystal and the circuit does not close, then the first circuit must contain one or more dislocations. These two circuits are illustrated in Fig.1.3 and Fig.1.4. The closure failure vector QM is the Burgers vector of the dislocation.

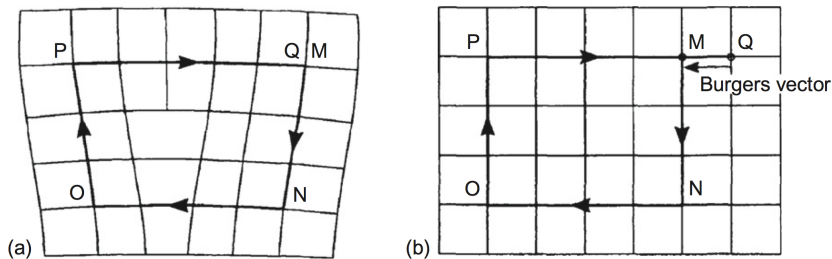


FIGURE 1.3: (a) Burgers circuit round an edge dislocation with positive line sense into the paper, (b) the same circuit in a perfect crystal; the closure failure is the Burgers vector ([Hull & Bacon, 1984](#)).

The direction and magnitude of the Burgers vector associated with a dislocation have specific crystallographic forms. If the burgers vector is a primitive lattice vector or a vector that is the sum of primitive lattice vectors, *i.e* if the vector connects equivalent atom sites in the perfect crystal lattice, then the misfit energy is mainly localized near the core of the dislocation. If the Burgers vector can not be decomposed to a sum of primitive lattice vectors there is a long-range, divergent misfit energy contribution caused by the mismatch of atoms. In order to reduce this misfit energy, all dislocations

in crystals are expected to be perfect dislocations, meaning that their burgers vectors are perfect lattice displacements ([Hirth & Lothe, 1982](#)). The elastic energy associated with a dislocation is also proportional to b^2 . Moreover, the Peierls stress, the minimum stress needed to overcome the lattice resistance to the movement of a dislocation at zero temperature, is least for the dislocations with the smallest-magnitude Burgers vector (see eq.1.6), so that these should slip more easily than the larger ones among all stable Burgers vectors. Finally, according to Frank's criterion ([Frank & van der Merwe, 1949](#)), if a perfect dislocation with Burgers vector \mathbf{b}_1 can dissociate into perfect dislocations $\mathbf{b}_2 + \mathbf{b}_3$, dissociation will occur if $b_1^2 > b_2^2 + b_3^2$, meaning that any dislocation with a Burgers vector which is a multiple of a perfect-dislocation Burgers vector is unstable. Therefore, between all the perfect dislocations only those with the shortest Burgers vector are stable. In body-centered cubic crystals like tungsten this implies that $\mathbf{b} = \frac{1}{2}[1\ 1\ 1]$, the shortest possible lattice translation vector in the lattice.

1.3.3 Types of dislocations

Dislocations can be classified by the geometrical relation between their dislocation line ξ and the Burgers vector \mathbf{b} :

- If the dislocation line and the Burgers vector are perpendicular as in Fig. 1.3, there is an *edge dislocation*.
- If the dislocation line and the Burgers vector are parallel as in Fig. 1.4, there is a *screw dislocation*.
- If the dislocation line lies at an arbitrary angle to its Burgers vector, there is an *mixed dislocation*.

1.3.4 Movement of dislocations in bcc crystals

There are two basic types of mechanisms to explain dislocation motion: dislocation glide and dislocation climb. *Glide* is a conservative type of movement where the dislocation moves along a surface, called *slip plane*, containing both the dislocation line and its Burgers vector. *Climb* is a non-conservative type of movement where the dislocation moves out of the glide surface. Between these mechanisms, *slip*, the result of

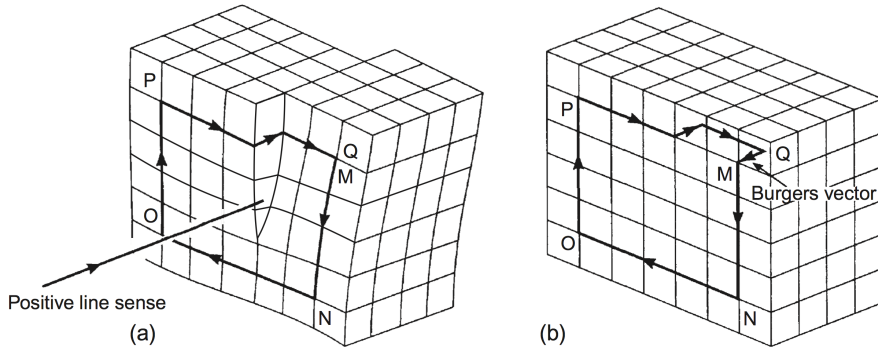


FIGURE 1.4: (a) Burgers circuit round a screw dislocation with positive line sense in the direction shown, (b) the same circuit in a perfect crystal; the closure failure is the Burgers vector ([Hull & Bacon, 1984](#)).

gliding many dislocations, is the most common manifestation of plastic deformation in crystalline solids ([Hull & Bacon, 1984](#)).

The process of slip occurs along *slip systems*, which are defined by a *slip plane* and a *slip direction*. Because the Burgers vector and the dislocation line are parallel in a screw dislocation, the glide plane with normal defined by $\mathbf{b} \times \boldsymbol{\xi}$ is not restricted to a specific plane. Any plane for which \mathbf{b} is a zone axis³ is a possible glide plane for a screw dislocation. For an edge dislocation, where the Burgers vector and the dislocation line are perpendicular, the glide plane is limited to a specific plane.

The slip planes and slip directions in a crystal are not arbitrary. The slip planes are normally the planes with the highest density of atoms, i.e those with a larger interplanar spacing, and the slip direction is a direction in the slip plane with one of the shortest lattice vector, i.e the Burgers vector. Details about these affirmations can be found in ([Hirth & Lothe, 1982](#)), but the main idea is that the distance between planes of the family $\{hkl\}$ in cubic crystals is defined as

$$d_{hkl} = \frac{a_0}{\sqrt{h^2 + k^2 + l^2}} \quad (1.5)$$

where a_0 is the lattice parameter of the perfect crystal, and the Peierls stress is given by

$$\sigma_p = \frac{2\mu}{1-\nu} \exp\left(-\frac{2\pi d_{hkl}}{b(1-\nu)}\right) \quad (1.6)$$

³A zone axis is the line of intersection of a set of planes ([Barrett & Massalski, 1966](#)).

where μ is the shear modulus and ν is the Poisson's ratio. One can easily see that the planes which are most widely spaced have a lower Peierls stress and then they are more favorable for slip.

In bcc metals like tungsten the slip direction is then $\frac{1}{2} \langle 111 \rangle$ and the crystallographic slip planes are $\{110\}$, $\{112\}$ and $\{123\}$. Dislocation slip in bcc metals has been reported in the literature on $\{110\}$, $\{112\}$ and $\{123\}$ planes with some uncertainty. While some authors have suggested that the temperature range determines the activation of slip planes ($\{110\}$ and $\{112\}$ planes at lower temperatures, $\{123\}$ planes at higher temperatures) (Ma et al., 2007; Raabe, 1995a; Sestak & Seeger, 1978), other works propose the decomposition of $\{112\}$ and $\{123\}$ planes on two alternating $\{110\}$ planes to justify the activation of $\{110\}$ slip planes at room temperature(Brunner, 2010; Christian, 1983; Madec & Kubin, 2004; Spitzig & Keh, 1970; Van Petegem et al., 2013). The particular geometry of the bcc lattice guarantees that there are three $\{110\}$, three $\{112\}$ and six $\{123\}$ planes intersecting along the same $\langle 111 \rangle$ direction, see Fig.1.5 , increasing the possibilities for screw dislocations to move by cross slip.

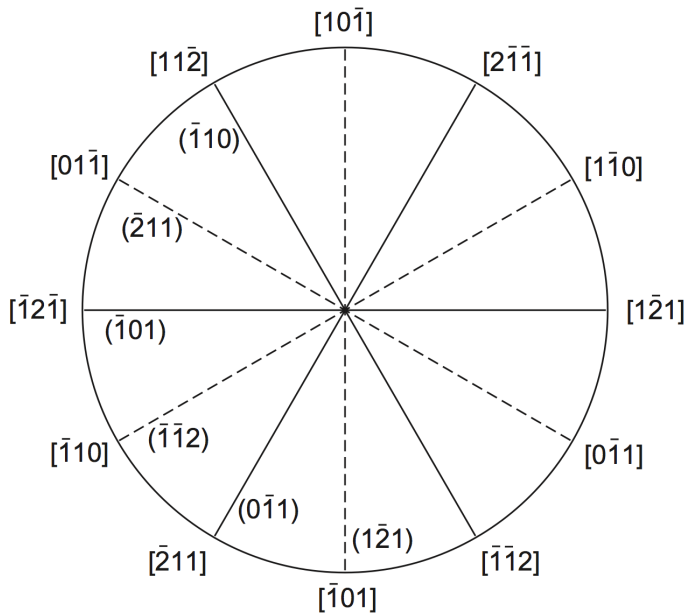


FIGURE 1.5: Orientation of the $\{110\}$ and $\{112\}$ planes along the $[111]$ zone (Hull & Bacon, 1984).

1.3.4.1 Orowan's equation

Orowan not only defined the concept of *dislocation* in 1934 (Orowan, 1934a,b,c) but he also established in 1940 (Orowan, 1940) the relation between the plastic strain and the

product of the density, the Burgers vector and the velocity of dislocations.

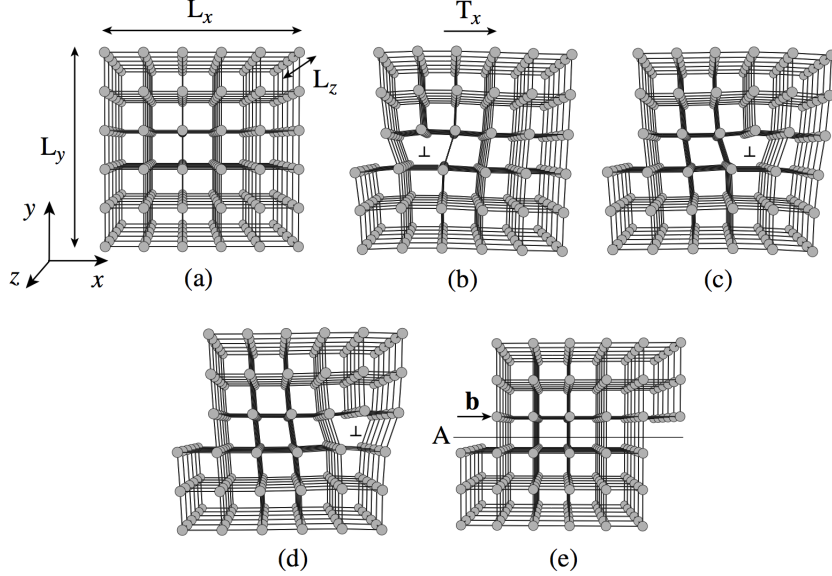


FIGURE 1.6: (a) A perfect crystal with simple cubic structure and dimension $L_x \times L_y \times L_z$. (b) The top surface is subjected to a traction force T_x while the bottom surface is fixed. An edge dislocation nucleates from the left surface. In (c) and (d) the dislocation moves to the right. In (e) the dislocation finally exits the crystal from the right surface. The net result is that the upper half of the crystal is displaced by \mathbf{b} with respect to the lower half (Bulatov & Cai, 2006).

If we consider the mechanism of motion of an edge dislocation illustrated in Fig. 1.6, the plastic shear strain added when one dislocation glides through the entire crystal is

$$\gamma_p = \frac{b}{L_y} . \quad (1.7)$$

When one dislocation glides only a distance x in the crystal (Fig. 1.6.c and Fig. 1.6.d), the plastic shear strain added is

$$\gamma_p = \frac{x}{L_x} \frac{b}{L_y} , \quad (1.8)$$

and when N dislocations glide through a distance x in the crystal, the plastic shear strain is

$$\gamma_p = N \frac{x}{L_x} \frac{b}{L_y} = \frac{N L_z x b}{V} \quad (1.9)$$

where $V = L_x \cdot L_y \cdot L_z$ is the volume of the perfect crystal. If we define the dislocation density as dislocation line per unit of volume, $\rho = \frac{NL_z}{V}$, then we can express the plastic strain accumulated by N dislocations as $\gamma_p = \rho bx$. When we take temporal derivatives in this last expression we obtain

$$\dot{\gamma}_p = \frac{\delta\gamma}{\delta t} = \frac{\delta(\rho bx)}{\delta t} = \rho b \frac{\delta x}{\delta t} = \rho bv \quad , \quad (1.10)$$

the *Orowan's equation*, which relates the plastic strain rate, the dislocation density ρ , the magnitude of the Burgers vector b , and the average velocity of the dislocation v .

The velocity of edge and screw dislocations has been experimentally reported in the literature. These results reflect that edge dislocations move many times faster than screw dislocations. According to Orowan's equation, a lower velocity of dislocation implies a lower plastic strain and then a more brittle behavior of the material. This is one of the reasons why our research mainly focuses on the study of the mobility of screw dislocations.

1.3.4.2 Driving forces for screw dislocation motion

The force per unit length \mathbf{f} acting on a dislocation is defined by the *Peach-Koehler formula* ([Hirth & Lothe, 1982](#)),

$$\mathbf{f} = (\boldsymbol{\sigma} \cdot \mathbf{b}) \times \boldsymbol{\xi} \quad (1.11)$$

where $\boldsymbol{\sigma}$ is the local stress field and \mathbf{b} , $\boldsymbol{\xi}$ are the dislocation line and Burgers vectors, respectively. This expression guarantees that the force is always perpendicular to the dislocation line.

In the particular case of the screw dislocation represented in Fig. 1.7, where $\mathbf{b}=[b\ 0\ 0]$ and $\boldsymbol{\xi}=[1\ 0\ 0]$, the Peach-Koehler force is

$$\mathbf{f} = \left(\begin{bmatrix} \sigma_{xx} & \sigma_{xy} & \sigma_{xz} \\ \sigma_{yx} & \sigma_{yy} & \sigma_{yz} \\ \sigma_{zx} & \sigma_{yz} & \sigma_{zz} \end{bmatrix} \cdot \begin{bmatrix} b \\ 0 \\ 0 \end{bmatrix} \right) \times \begin{bmatrix} 1 \\ 0 \\ 0 \end{bmatrix} = \begin{bmatrix} 0 \\ \sigma_{xz}b \\ 0 \end{bmatrix} \quad (1.12)$$

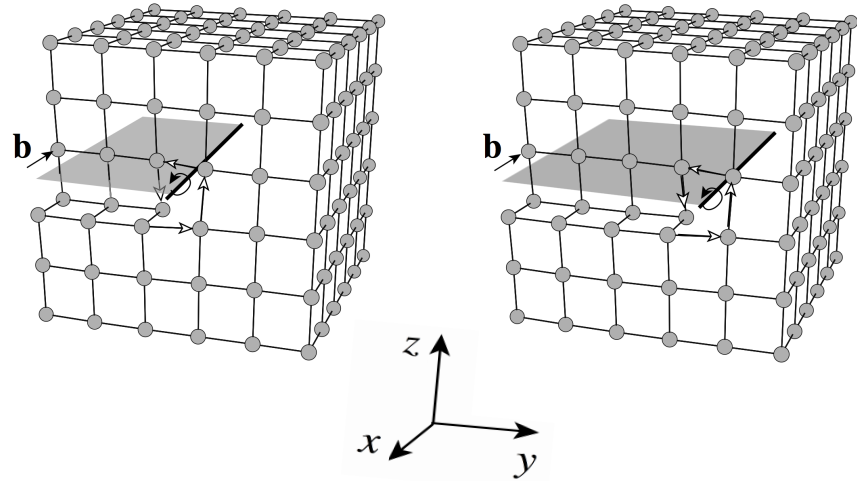


FIGURE 1.7: A screw dislocation moving along the glide plane in a cubic crystal
[\(Bulatov & Cai, 2006\)](#).

and then the component of the force f_y in the direction of motion of the dislocation only depends on the σ_{xz} component of the local stress. This implies that we only have to apply the stress σ_{xz} to move the dislocation in the direction of slip y .

Part I

ATOMISTIC SIMULATIONS

Chapter 2

Assessment of interatomic potentials for atomistic analysis of static and dynamic properties of screw dislocations in tungsten

2.1 Introduction

Transgranular plasticity in refractory metals, including W, is governed by the temperature dependence of screw dislocation motion. W is typically alloyed with 5~26 at.% Re to increase low temperature ductility and improve high temperature strength and plasticity ([Lassner & Schubert, 1999](#)). The physical origins behind the Re-induced ductilization have been discussed in the literature ([Li et al., 2012](#); [Romaner et al., 2010](#); [Wurster et al., 2010](#)) and point in some way or another to alterations in the core structure of $\frac{1}{2}\langle 111 \rangle$ screw dislocations, which both reduce the effective Peierls stress σ_P and extend the number of possible slip pathways. A direct consequence of a reduced Peierls stress, *e.g.* as via Re alloying, is an enhanced dislocation mobility at low temperatures. Recent electronic structure calculations of σ_P in pure W give values between 1.7 and 2.8 GPa ([Romaner et al., 2010](#); [Samolyuk et al., 2013](#)). This means that, under most conditions relevant to technological applications, where stresses are of the order of only a few hundred MPa, a reduction in σ_P of a few hundred MPa may not be significant to the plastic behavior of W and W alloys. Instead, it is the thermally-activated and

three-dimensional character of screw dislocation motion, the associated solution softening behavior, as well as the temperature dependence of the core structure, that control bulk ductility.

None of these aspects can be studied in atomistic detail using current experimental capabilities. By contrast, atomistic methods based on semiempirical potentials have enabled large-scale molecular dynamics (MD) simulations, so that, at present, calculations of single-dislocation mobility, core structure and transformations, etc., can be obtained with reasonable accuracy. However, care must be exercised when choosing from the dozen or so W potentials available in the literature. Semiempirical force fields with both pair and cohesive contributions (*e.g.* following the embedded atom method formalism) are typically considered to achieve an optimum balance between efficiency and accuracy. These are typically fitted to reproduce some basic bulk and defect properties such as lattice parameter, elastic constants, vacancy formation energy, surface energies, etc., but generally not dislocation properties. Of these, it is known that the screw dislocation core structure at 0 K should be non-degenerate (also known as *compact*), as revealed by density functional theory (DFT) calculations ([Li et al., 2012](#); [Romaner et al., 2010](#); [Samolyuk et al., 2013](#)).

Previous atomistic calculations on screw dislocations in W have been performed by Mrovec *et al.* ([Mrovec et al., 2007](#)), Fikar *et al.* ([Fikar et al., 2009](#)) and Tian and Woo ([Tian & Woo, 2004](#)). Mrovec *et al.* ([Mrovec et al., 2007](#)) studied the dislocation core structure and calculated the Peierls stress at 0 K using a tight-binding-based bond-order potential (TB-BOP)¹. They predicted a non-degenerate core structure and a Peierls stress of 4.3 GPa. For their part, Fikar *et al.* studied core structures and energies of screw dislocations using three different interatomic potentials, all of which display dissociated cores. Lastly, Tian and Woo examined the mobility of screw dislocations also with an embedded-atom potential that predicts a dissociated core structure. They were able to obtain dislocation velocities at stresses above the Peierls stress at 0 K. However, no systematic study of dislocation motion in W at finite temperature has been conducted. Characterizing dislocation motion in the stress-temperature space is important to parameterize the so-called mobility functions used in higher-level methods such as dislocation dynamics. The purpose of the mobility functions is to provide a quantitative measure of the response of dislocations to applied and internal stresses.

¹BOP potentials include non-central atomic interactions to represent the effect of *d*-electrons in transition metals

Unfortunately, one of the most important difficulties associated with such studies is the scale-dependent nature of MD simulations, which require exceedingly high strain rates to drive the system over time scales accessible computationally, of the order of a few tens of ns. Because of these limitations, MD is incapable at present of properly capturing the thermally-activated motion of screw dislocations at low stresses. However, MD simulations can still provide valuable input in intermediate-to-high stress conditions and in situations where the deformation rates are high. The objective of this chapter is to compare five different interatomic potentials –that have not been fitted against screw dislocation data– and assess their performance in terms of static and dynamic screw dislocation properties. By static properties we mean several reference parameters at 0 K as obtained with DFT calculations. The dynamic behavior is evaluated in terms of screw dislocation mobility as a function of stress and temperature. Due to the absence of ‘reference’ mobility data against which to compare the potentials, we will simply draw several general conclusions based on the inter-comparison among potentials.

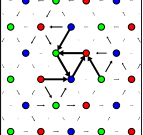
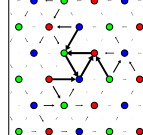
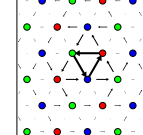
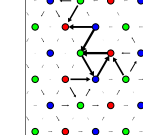
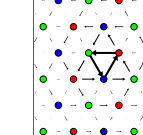
The chapter is organized as follows. First, we discuss the distinctive features of each potential and calculate the structure of a screw dislocation core. The Peierls potential and the γ surface are then calculated and verified against existing DFT and TB-BOP calculations. Following this, we introduce the computational setup for the dynamic mobility simulations and calculate dislocation velocities as a function of temperature and stress. Subsequently, a study of the core trajectories in the plane defined by the glide and normal directions is carried out. We finish by analyzing the causes of the temperature-dependent behavior of each potential and emphasizing the insufficiency of static calculations to fully characterize dislocation motion at finite temperatures.

2.2 Statical properties of interatomic potentials

Our calculations have been performed with the parallel MD code LAMMPS ([Plimpton, 1995](#)). Table 2.1 gives basic information about the five different potentials considered here, among which there are three embedded-atom method (EAM) potentials, one Tersoff-Brenner-type bond-order potential (TF-BOP), and one modified EAM (MEAM). Note that the TB-BOP used by Mrovec *et al.* ([Mrovec et al., 2007](#)) was deemed not suitable for dynamics simulations by its authors ([Mrovec et al., 2011](#)) and has thus not been considered here. Hereafter they are referred to in the text by the identifiers given in the table header. This selection of W potentials, from the dozen or so available in the

literature, is not meant to be an implicit assessment of the quality of those not employed here.

TABLE 2.1: Properties of potentials used: lattice parameter a_0 , shear modulus μ , Peierls stress σ_P , computational cost, core structure at 0 K, and thermal expansion coefficient α . Potentials EAM1, EAM2 and TF-BOP display a threefold symmetric (degenerate) core, while EAM3 and MEAM predict compact (non-degenerate) cores. The values of the volumetric thermal expansion coefficients, α , are used in Section 2.4.

Potential	EAM1	EAM2	EAM3	TF-BOP	MEAM
Ref.	^b	^c	^d	^e	^f
a_0 (Å)	3.165	3.165	3.143	3.165	3.188
μ (GPa) ^g	160	163	161	170	161
σ_P (GPa) ^h	4.0	3.9	2.0	1.1	3.2
Computational cost relative to EAM1 ⁱ	1.0	0.4	0.9	5.4	9.1
Core structure at 0 K ^j					
$\alpha (\times 10^{-5} \text{ K}^{-1})^k$	1.40	2.42	1.76	2.38	1.64

^b(Zhou et al., 2001)

^c(Ackland & Thetford, 1987)

^d(Marinica et al., 2013)

^e(Juslin et al., 2005)

^f(Park et al., 2012)

^gW is isotropic elastic and, thus, the value of μ given is equally valid for {110} and/or {112} slip.

^hFor consistency, our Peierls stress calculations use the same geometry as the DFT calculations by Romaner et al. (Romaner et al., 2010) and Samolyuk et al. (Samolyuk et al., 2013), which reveal a value of σ_P between 1.7 and 2.8 GPa.

ⁱThe computational cost was evaluated using the cutoff radii specified in the original reference for each potential.

^jDFT calculations predict a compact, non-degenerate core.

^kThe experimental value for α is $1.45 \text{ to } 1.91 \times 10^{-5} \text{ K}^{-1}$ in the 1000 to 2000 K temperature interval (Knibbs, 1969).

Two important quantities for characterizing screw dislocation cores at 0 K are the Peierls potential, defined as the energy path from one equilibrium position to another on a {110} plane, and the γ surface along the [111] direction also on {110} planes. The Peierls potential governs the morphology of kinks (e.g. (Gordon et al., 2010)) while workers such as Duesbery and Vitek (Duesbery & Vitek, 1998) have provided evidence for a direct correspondence between the shape of the $\frac{1}{2}\langle 111 \rangle\{110\}$ gamma surface and the screw dislocation core structure. These are plotted, respectively, for all potentials in

Figs. 2.1 and 2.2 on the $(\bar{1}\bar{1}0)$ plane. DFT data for both calculations are also shown for comparison.

The Peierls potential was obtained using the nudged elastic band method (Henkelman & Jónsson, 2001) (see Chapter 3) in the manner proposed by Gröger and Vitek (Gröger & Vitek, 2012), whereas the DFT calculations in both cases were obtained using a *plane wave self-consistent field* code as described in Refs. (Ventelon & Willaime, 2007) and (Ventelon et al., 2013).

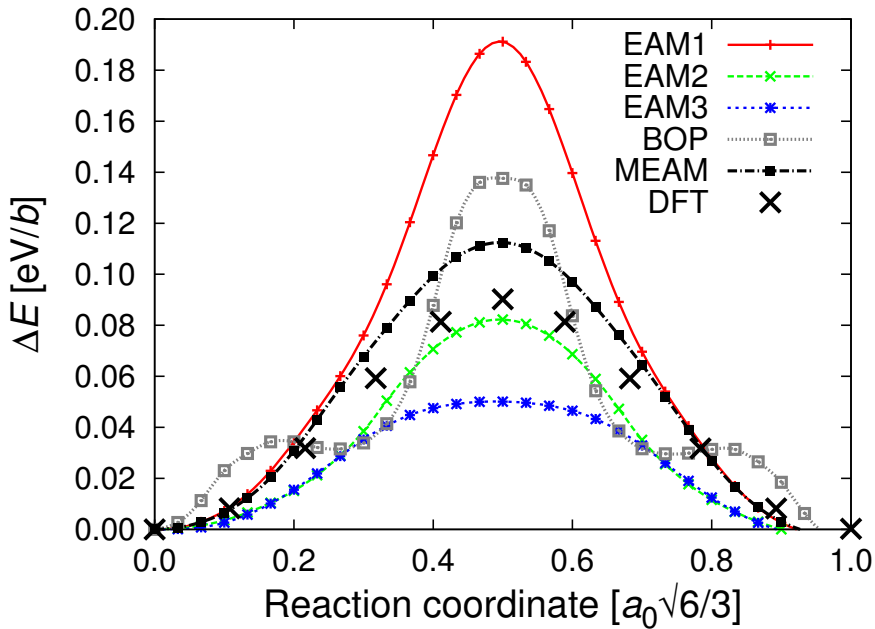


FIGURE 2.1: Peierls potential for all potentials tested here. DFT calculations from Ventelon *et al.* (Ventelon et al., 2013) are shown for comparison.

The five interatomic potentials tested here follow different formulations and have been fitted to different physical properties. It is not our objective to discuss the fitting process or the quality of each one, but only to discuss their performance in relation to screw dislocation modeling. When selecting potentials for screw dislocation simulations, two of the properties most looked at are the core structure and the Peierls stress. For W, these have been obtained using electronic structure calculations of different sorts, which reveal a compact core and σ_P between 1.7 and 2.8 GPa. Regarding the core structure at 0 K, only EAM3 and MEAM reproduce it correctly, although, as shown in Section 2.4, the EAM3 potential does not preserve this structure at high temperature. In terms of σ_P , the five potentials studied here give a range of values from 1.1 to 4.0 GPa. As Table 2.1 shows, EAM3 and MEAM display values of 1.8 and 3.2 GPa, respectively, which are the most consistent with the range obtained by DFT calculations.

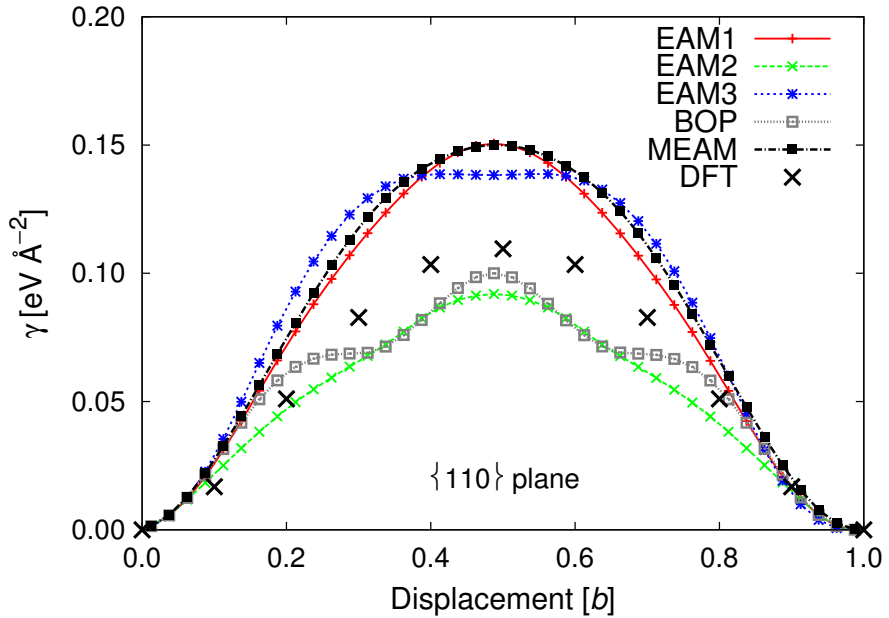


FIGURE 2.2: $(1\bar{1}0)$ γ surface along the $[111]$ direction for all the potentials considered in this work. DFT calculations from Ventelon *et al.* ([Ventelon et al., 2013](#)) are shown for comparison.

Furthermore, the subspace of the energy landscape most relevant to screw dislocation motion is the Peierls potential and the γ surface (Figs. 2.1 and 2.2). Relative to the DFT calculations, the sinusoidal shape of the Peierls potential is best reproduced by potentials EAM3 and MEAM. Interestingly, however, the magnitude of the Peierls energy is most closely predicted by EAM2. EAM1 overestimates this energy by about a factor of two, while the TF-BOP predicts a trajectory with metastable states along its path, both in clear disagreement with DFT calculations. Regarding the γ surface, potentials EAM1, EAM3 and MEAM all predict the essential qualitative and quantitative features of the DFT results and are also in good agreement with the results by Gröger *et al.* using a TB-BOP ([Gröger et al., 2008b](#)).

Thus, on the basis of all these calculations, the MEAM potential appears to be the best suited of those tried here to carry out dislocation simulations at any temperature. When computational cost is of the essence, EAM3 may be considered an acceptable replacement for static calculations or at low temperatures and stresses.

2.3 Mobility of screw dislocations

2.3.1 Simulation setup

MD simulations of dislocation motion are defined by the triad composed of the line, plane normal and glide directions ([Bulatov & Cai, 2006](#); [Hull & Bacon, 1984](#)). The line direction ξ must reflect the character of the dislocation, e.g. $\langle 111 \rangle$ for screw dislocations in bcc metals. The plane normal direction \mathbf{n} must reflect the nature of slip, e.g. $\langle 110 \rangle$ or $\langle 112 \rangle$. The glide direction \mathbf{m} can be arbitrary, although it is common to take $\mathbf{m} = \xi \times \mathbf{n}$ so that orthorhombic simulation cells can be used. A single dislocation in such a cell breaks the periodicity of the box along the normal direction resulting in surfaces with normal vector \mathbf{n} of finite dimensions. Typically, stress or strain rate boundary conditions are imposed on these surfaces to drive dislocation motion. Both methods are valid and should converge in the infinite time and length limits. However, stress-controlled simulations do not prescribe the dislocation velocity (from $v = \dot{\varepsilon}/\rho v$, where $\dot{\varepsilon}$ is the strain rate, ρ the dislocation density, and $b \equiv \|b\|$) and are independent on the size of the computational cell.

To measure dislocation velocities, we have performed stress-controlled simulations of $\frac{1}{2}\langle 111 \rangle$ dislocations with the maximum resolved shear stress (MRSS) on a $\{112\}$ plane. The justification to focus on $\{112\}$ -type planes is twofold. First, as Argon and Maloof ([Argon & Maloof, 1966b](#)) have shown, under tensile loading, most loading orientations and temperatures, result in some degree of $\frac{1}{2}\langle 111 \rangle\{112\}$ slip. Also, Li *et al.* ([Li et al., 2012](#)) have shown that $\{112\}$ slip is important in W alloys with high Re concentrations. Second, certain EAM potentials intrinsically deviate from MRSS behavior when the MRSS plane is of the $\{110\}$ type for reasons that have been discussed at length in the literature ([Chaussidon et al., 2006](#); [Gilbert et al., 2011](#); [Gröger et al., 2008b](#)).

A typical setup for stress-controlled screw dislocation simulations is shown in figure 2.3.

The principal axes x, y, and z of the MD cell were oriented along the $[111]$, $[1\bar{1}0]$, and $[11\bar{2}]$ directions, corresponding to the line, glide and normal directions respectively. The screw dislocation is generated at the center of the box by using the isotropic elastic displacement solution ([Hull & Bacon, 1984](#)).

Periodic boundary conditions are imposed along the x and y directions, whereas traction surfaces bound the system along the z direction. Stress is applied on these surfaces via

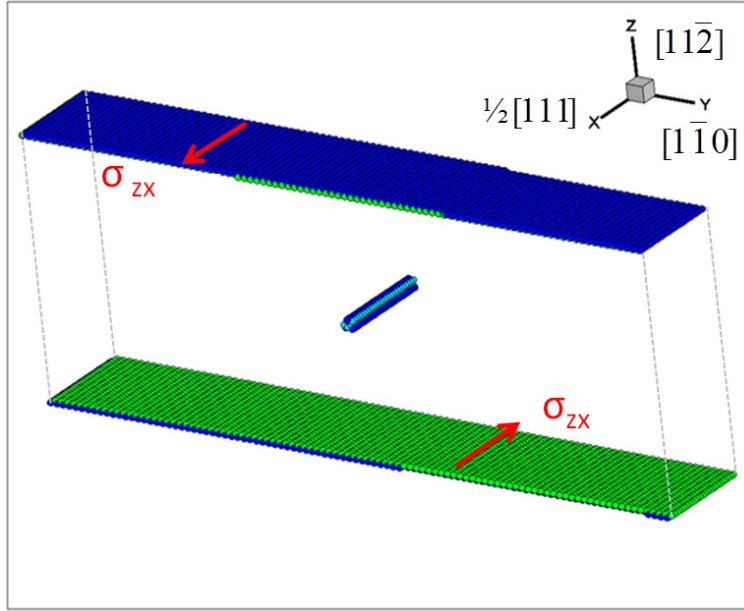


FIGURE 2.3: MD simulation setup.

surface tractions that satisfy $F = \sigma A$, where σ is the desired stress and $A = L_x L_y$ is the exposed area defined by the dimensions along x and y . For the orientation shown in figure 2.3, the stress component that creates a Peach-Kohler force in the glide direction is σ_{xz} . The traction F is distributed evenly among one or several layers of atoms adjacent to the surface. Atoms in these layers are held rigid with respect to one another and are not subjected to MD.

The dimensions of the simulation box were chosen to maximize the physical fidelity of the simulations while keeping the computational cost manageable. First, the dislocation line length L_x must be sufficiently long to support a kink-pair mechanism of motion under the proper conditions (Marian et al., 2004). Second, the dimension along the glide direction L_y was chosen such that the heat generated by the mechanical work during dislocation glide was dissipated before sequential dislocation passages through the periodic boundary. Finally, L_z was set so as to keep image forces small around the glide plane. More details about these optimization strategies are given by Gilbert et al (Gilbert et al., 2011). Of course, these strategies only set generic guidelines and the specific dimensions that satisfy them are potential dependent. The reference cell dimensions were $L_x = 25 \left[\frac{\sqrt{3}}{2} a_0 \right]$, $L_y = 100 \left[\sqrt{2} a_0 \right]$, and $L_z = 50 \left[\sqrt{6} a_0 \right]$, where the amounts in brackets are the dimensions of the nominal unit cell in the coordinate system employed here. The reference configuration contains 7.5×10^5 atoms, which results in strain rates of $1.4 \times 10^{6\sim 7} \text{ s}^{-1}$ for dislocation velocities between 10 and $100 \text{ m}\cdot\text{s}^{-1}$.

Prior to the application of stress, the computational cell is equilibrated at the desired temperature in the microcanonical ensemble. σ_{xz} is then applied on the computational cell boundaries and simulations are conducted in the *NPT* ensemble. All MD simulations were performed using the massively parallel code LAMMPS ([Plimpton, 1995](#)) in a temperature range of 300 to 2100K, and a stress range of 300 to 2000 MPa. These simulations were run on LLNL’s ATLAS cluster using 128 and 256 processors at a reference cost of 1.7×10^{-5} CPU seconds per atom per time step for potential EAM1.

2.3.2 Techniques to accelerate convergence of stress-controlled MD simulations of dislocation motion

All the simulations were run for 100 ps and configuration data were extracted every picosecond. In this subsection we will discuss the effects of using different time functions for the applied stress for the particular MEAM interatomic potential ([Park et al., 2012](#)). The procedure to extract dislocation velocities from MD simulations is well established in the literature ([Bulatov & Cai, 2006](#); [Gilbert et al., 2011](#); [Olmsted et al., 2005](#)): from the position of the core, velocities are calculated as the derivative of the displacement-time curves for each case.

A step function consists of a transition from 0 to σ_{xz} from one time step to the next. This sudden application of stress results in elastic waves generated at the system boundaries that travel at the transversal speed of sound ($c_t = 2890 \text{ m}\cdot\text{s}^{-1}$ for this potential). When these waves reach the opposite end of the computational, they reflect and travel back across the sample with reversed sign. In this fashion, every time either a positive or a negative step wave reaches the dislocation (situated at the center of the box), the dislocation will feel forward or arrest forces depending on the sign of travelling wave. This method is commonplace and has been widely used in the literature ([Chaussidon et al., 2006](#); [Gilbert et al., 2011](#); [Gordon et al., 2010](#); [Gröger et al., 2008b](#)). Its effects are shown in figure 2.4, where the dislocation displacement is plotted against time for a simulation at 1500K and 1100 MPa. The figure shows a succession of steps resembling a stairway. The sloped part of the steps corresponds to exposure to positive elastic waves, whereas the ‘flat’ part results from the cancellation of the acting positive wave with a reverberating negative wave. A simple calculation shows that the duration of each step is of the order of $L_z/c_t \approx 7 \text{ ps}$.

To support this argument, we also plot in figure 2.4 the σ_{xz} component of the virial stress with time. As shown, the shear stress wave oscillates around the prescribed value of applied stress. Overlaying σ_{xz} to the dislocation displacement leads to two interesting observations. First, the period of the elastic wave is coincident with the duration of one step. Second, the stress wave amplitude reaches its maxima at the midpoint flat section of each step. These points correspond to the instances at which positive elastic waves traverse the dislocation glide plane. Conversely, the minima are attained when negative waves reach the glide plane. Travelling waves are gradually attenuated due to scattering processes as seen by the decrease in the amplitude of the displayed oscillations with time. It is expected that, as oscillations are suppressed, the system reaches a state of homogeneous shear stress and the displacement-time curves are perfectly linear.

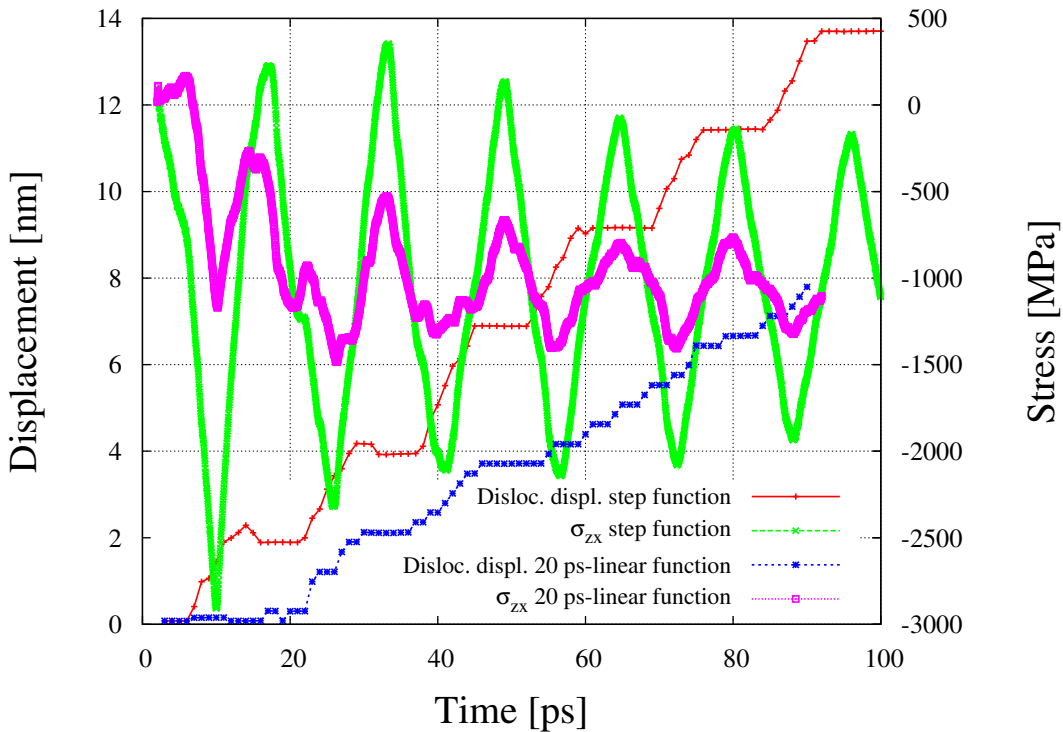


FIGURE 2.4: Screw dislocation position as a function of time for a simulation at $T = 1500$ K and $\sigma = 1100$ MPa, both for the case of a step function and a linear function with a slope of 20 ps.

An alternative to the sudden application of stress is the use of some monotonic time function. For simplicity, here we explore linear functions noting that any other higher order function could be equally acceptable. In this fashion, we ‘ramp up’ the applied stress from zero to its prescribed value, σ_0 , and start measuring dislocation displacement precisely at that time. The linear function is also characterized by the time duration of the ramp, $\theta : \sigma(t) = t/\theta\sigma_0$. Once the desired stress level is achieved, it is maintained

for the remainder of the simulation. The results for the linear stress function case are also shown in figure 2.4. The figure shows data for a simulation where a slope of $\sigma = 20$ ps was used. As the figure shows, the amplitude of the oscillations is much reduced and the smoothness of the displacement-time curve is increased. More importantly, the overall slope of the displacement-time curves, i.e. the dislocation velocity, appears rather different at plain sight. To further study the effect of the time constant on the shape of the displacement-time curves, we have carried out simulations in the 200-2000 MPa stress range every 300 MPa using a step function and two linear functions with time constants of $\sigma = 10$ and 20 ps. We have found that the differences between these two are practically negligible. This is further confirmed by looking at the resulting velocities in each case, obtained as the derivatives of least-squares linear fits to the displacement-time data. These are plotted in figure 2.5.

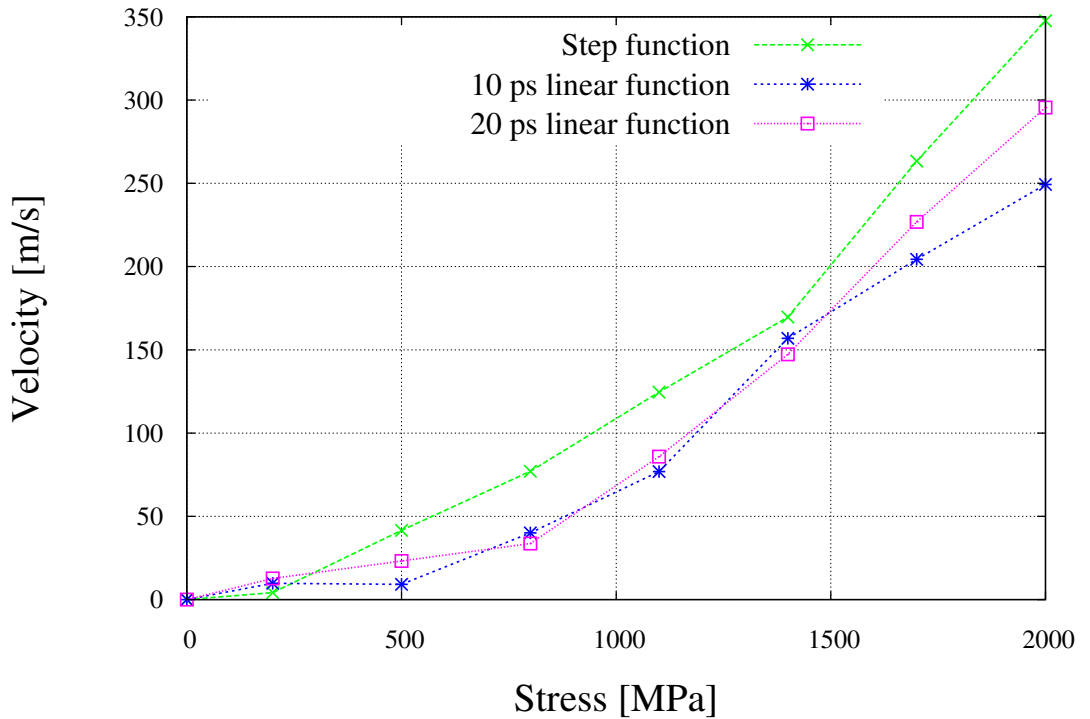


FIGURE 2.5: Screw dislocation velocity at $T=1200$ K using step function, linear function with $\theta = 10$ ps, and linear function with $\theta = 20$ ps.

The figure clearly shows that, except perhaps at 2000 MPa, using a linear function with 10 or 20 ps has not noticeable impact on the dislocation velocities. More worrisome is the fact that, as figure 2.4 shows, 100 ps may not sufficient to obtain converged results using a stress step. In the next paragraph we explore the conditions under which step functions may be used safely on the basis of convergence with the linear function calculations.

As it was shown in figure 2.4, stress wave reflections are gradually damped. The question that logically follows is at which point do fluctuations become of the same order as those that appear in simulations using linear stress functions. To this end, in figure 2.6 we extend step and linear function simulations up to 300 ps to study the convergence of stress fluctuations in each case. Also plotted is the exponential decay function that envelops the maxima of the oscillations in the step function simulations. This function is proportional to $e^{-0.02t}$, i.e. defined by a time constant of $\tau \approx 50$ ps¹.

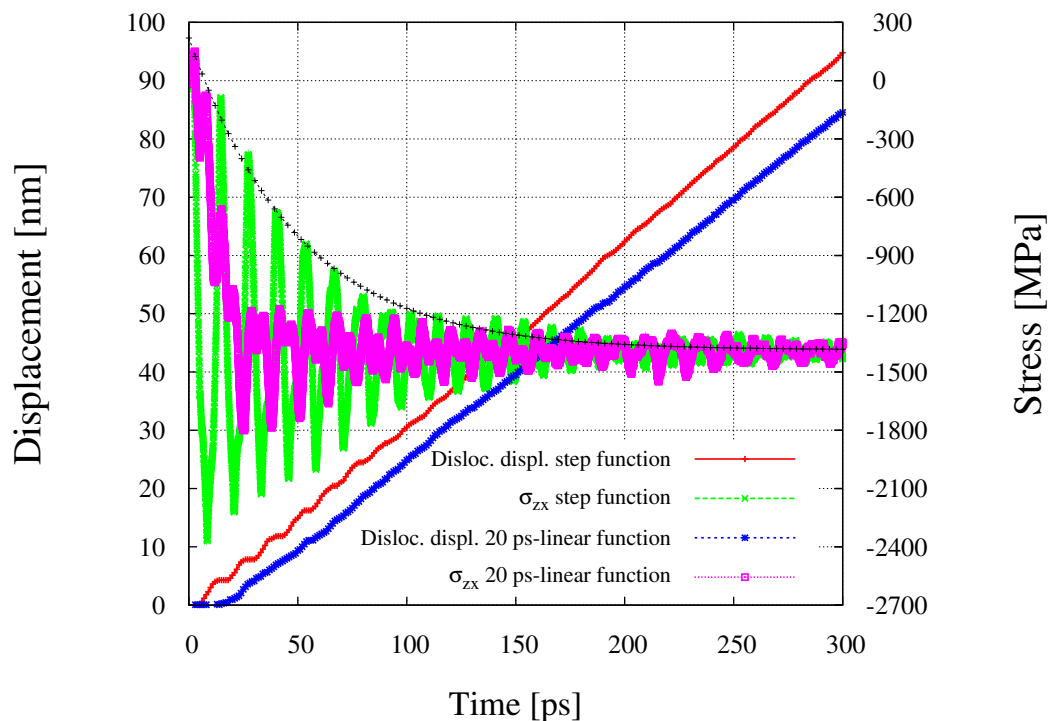


FIGURE 2.6: Screw dislocation position as a function of time during a 300-ps simulation at 600K and 1400 MPa. Also shown is the evolution of the σ_{zx} component of the virial with time.

Indeed, the figure shows that oscillations fall to within 3% of the steady state value (which is the range of the oscillations in the linear function case) after 185 ps of simulation, i.e. both approaches converge after a time of 3.5τ . Furthermore, the slope of the displacement-time curves becomes virtually equivalent. The figure essentially suggests that spending 20 seconds to build up shear stress prior to measuring velocities results in a net 165 ps savings of simulated time. This is a consideration to keep in mind when computational resources are limited.

¹The complete function is: $\sigma(t)=1606e^{-0.02t}-1387$ [MPa]. The independent constant is indicative of the applied stress, while the exponential factor represents the mean lifetime τ .

To emphasize the difference between 100-ps simulations using step and linear functions to apply external stress, we plot in figure 2.7 the normalized difference in velocity from both approaches. The plotted values correspond to the ratio $(v_s - v_l)/v_l$, where v_s and v_l are the dislocation velocities obtained using step and linear stress fucntions. Interestingly, at and above 1200K, the differences in dislocation velocities are only slight, whereas at lower temperatures the differences are more pronounced. This is likely related to the fact that fluctuations are scattered more efficiently via interactions with lattice phonons at high temperature. Generally speaking, the dislocation velocities for the linear function case are lower under the same conditions of temperature and applied stress.

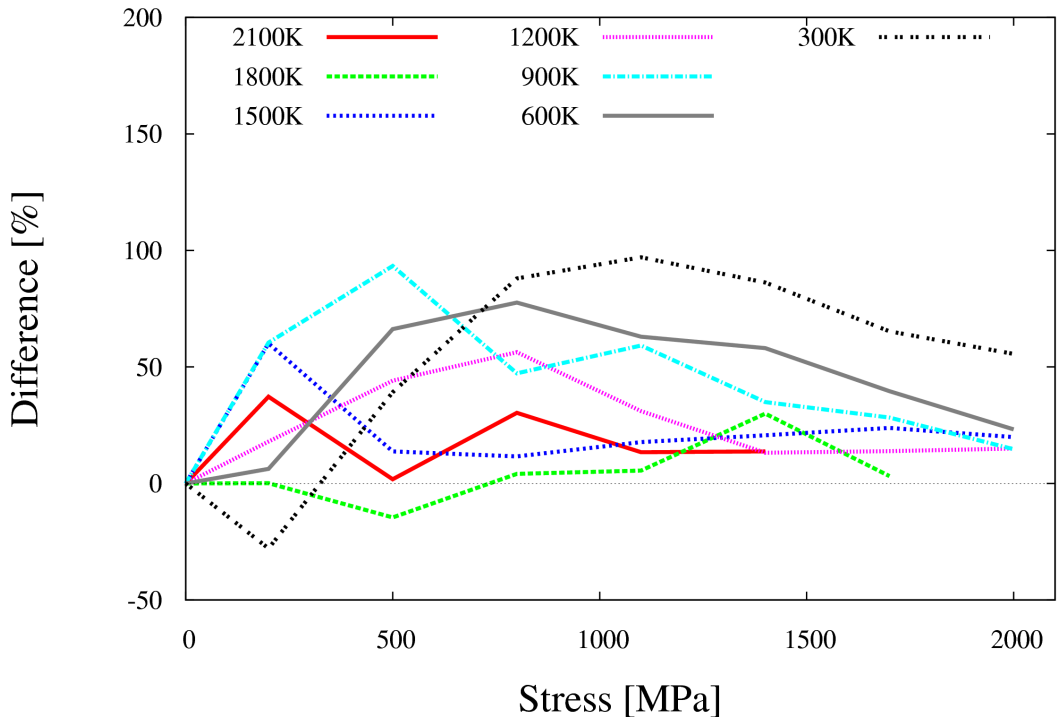


FIGURE 2.7: Percentage difference in screw dislocation velocity between step and linear stress function simulations. The data are plotted as a function of temperature and stress and the difference is computed as $(v_s - v_l)/v_l$.

The potential employed here displays a Peierls stress of 3.2 GPa, which means that all the calculations performed here up to 2.0 GPa fall within the thermally-activated regime of motion, governed by kink pair nucleation and propagation.

2.3.3 Results

Figure 2.8 shows all the (σ - v) data for the five interatomic potentials tested. The figures also contain the temperature dependence for each case. Generally, the velocities in-

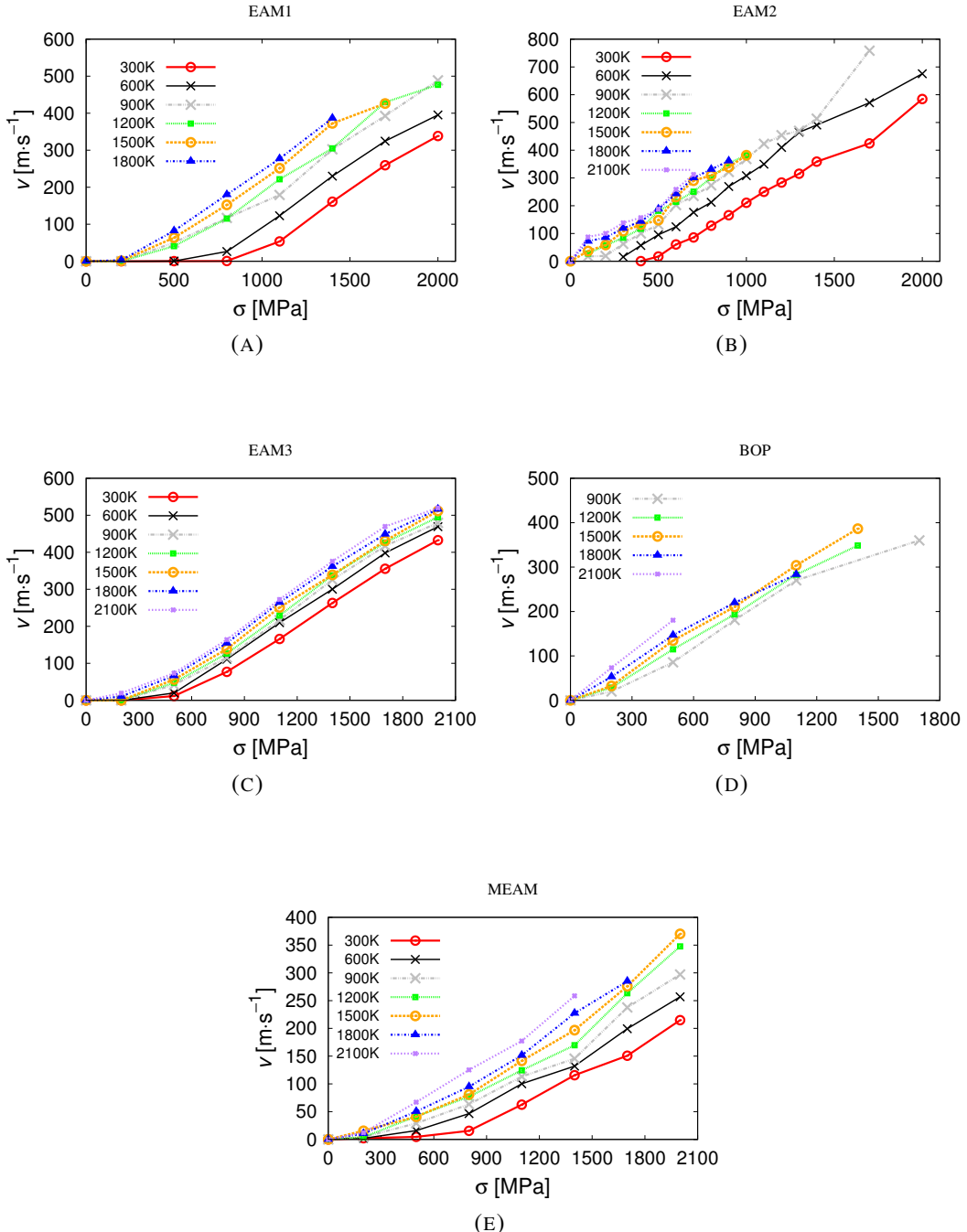


FIGURE 2.8: Screw dislocation velocity as a function of applied shear stress and temperature for the five interatomic potentials considered here. Note that the velocity and stress axes are not on the same scale for each case.

crease monotonically with stress and temperature, although at different rates depending

on the potential. To first order, the mechanism of motion followed by the dislocations depends on the Peierls stress. This means that, at a maximum applied shear stress of 2000 MPa, the EAM1, EAM2, and MEAM potentials both operate under σ_P (cf. Table 2.1), while for the EAM3 and TF-BOP there are several data points above it. In either case, dislocation motion is mostly governed by the thermally activated kink-pair nucleation mechanism, and thus display an exponential dependence with σ and T . This can be qualitatively appreciated in the figure, although in Section 2.5 a more quantitative analysis is carried out.

Another important aspect of dislocation motion is the extent of MRSS motion displayed, *i.e.* whether there are deviations from glide on the MRSS $\{112\}$ -type plane. In Figure 2.9 we analyze the trajectories on the yz -plane for different combinations of σ and T over 100 ps of simulation. Perfect MRSS behavior is characterized by trajectories parallel to 0° . As the figure shows, all the EAM potentials display nearly perfect MRSS behavior, while for the MEAM small deviations in the acceleration phase are captured. The TF-BOP potential displays the most erratic motion with an overall deviation of the order of five degrees. At lower temperatures, this effect is enhanced to the point that the dislocation exits the simulation box only a few picoseconds after the shear stress is applied. This is the reason why there are fewer data points –and none below 900 K– in the σ - v curves shown in Fig. 2.8 for the TF-BOP potential. In any case, the trajectories shown in the Fig. 2.9 are *effective*, *i.e.* they are not sufficiently time resolved to capture the atomistic details of dislocation motion. Nevertheless, the operating mechanism of motion is by way of nucleation and propagation of kink pairs on $\{110\}$ planes adjacent to the MRSS $(11\bar{2})$ plane.

Dislocation mobility is highly multidimensional in that it displays multiparametric dependencies, e.g. on stress, temperature, dislocation character, slip system, etc. Dislocation velocities are difficult to infer from straining experiments, while they are costly and subjected to size limitations in simulations. Measurements ([Schadler, 1964](#)) and calculations ([Gumbsch & Gao, 1999](#); [Li & Shi, 2002](#)) of edge dislocation velocities have been carried out in W. However, other than the values computed by Tian and Woo ([Tian & Woo, 2004](#)) at very high stress (>3.6 GPa), to our knowledge no data exist on screw dislocation mobility in W at low stresses. In this work, we have focused on the temperature and stress dependences, while we have kept the dislocation character and the slip system fixed.

A quick look at Fig. 2.10 reveals several interesting details. First, the EAM2 and MEAM consistently give the highest and lowest velocities, respectively, regardless of

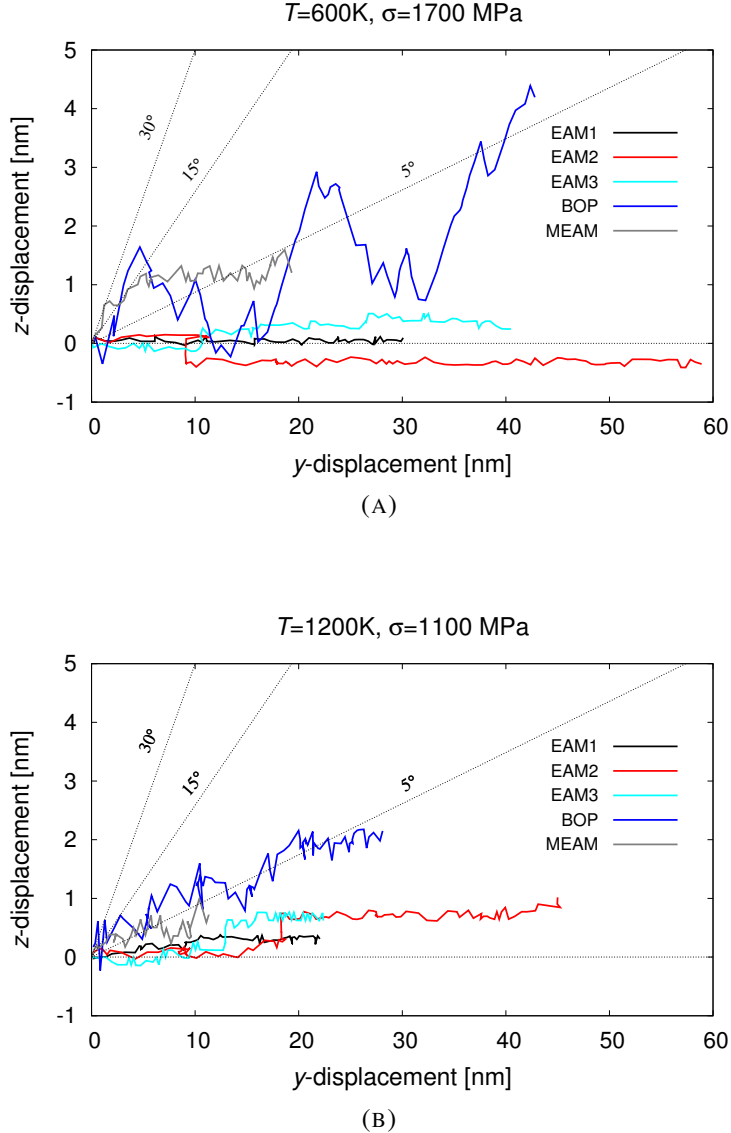


FIGURE 2.9: Line-averaged dislocation trajectories on the yz -plane for two combinations of σ and T and over 100 ps. Planes forming 0, 5, 15 and 30° with the $(11\bar{2})$ MRSS plane are represented with dotted lines (angles not to scale). Except for the TF-BOP potential, all the simulations yield small $<5^\circ$ deviations from MRSS motion.

temperature. Since atomistic simulations commonly overestimate screw dislocation velocities, particularly in the low-stress range, this may be another reason in favor of using MEAM. This is likely to be due to the fact that the dislocation core remains compact in the entire temperature range using the MEAM potential (cf. Fig. 2.12). Second, screw dislocations move by thermally-activated mechanisms below the Peierls stress, transitioning to a viscous damping regime above it. At the maximum applied stress of 2000 MPa, some dislocations have been driven past the Peierls stress as given by their respective potentials (cf. Table 2.1). This is certainly the case for the TF-BOP and possibly potentials EAM2 and EAM3. One would therefore expect to see a gradual exhaustion

of the thermally-activated regime and a transition into a linear regime. Interestingly, such a transition appears to occur for potential EAM1 which has $\sigma_P = 4.0$ GPa. It was shown by Gilbert *et al.* ([Gilbert et al., 2011](#)), however, that the actual transition stress decreases with the square of the temperature, which may be what is seen here. Appropriate exponential fits to the data shown in Fig. 2.10 carried out in Section 2.5 reveal useful parameters that define the thermally activated regime.

The dislocation trajectories shown in Fig. 2.9 demonstrate that screw dislocations move primarily along the direction of the applied stress. The only notable exception is the TF-BOP, for which significant transitions out of plane are observed. The figure, however, does not provide insights into the atomistic mechanism of motion. Then, in Fig. 2.11 trajectories for the EAM3 were analyzed with higher spatial and temporal resolution at temperatures 600 and 1800 K. At both temperatures, the dislocation moves by elementary $\{110\}$ kink-pair episodes. It is reasonable to assume that this mechanism can be extrapolated to other potentials that yield similar effective trajectories (close to MRSS plane). However, for the EAM3 results, there are some differences in terms of the temperature at which the trajectory was extracted. At 1800 K it appears as though the unit mechanism is composed of one $+30^\circ$ jump (on a $(01\bar{1})$ plane) followed by a correlated -30° jump (on a $(10\bar{1})$ plane). In other words, the dislocation appears to move by kink-pair episodes on the $(11\bar{2})$ plane that consist of two alternating and correlated $\pm 30^\circ$ kinks. This is consistent with the mechanism proposed by Duesbury ([Duesbury & Vitek, 1998](#)). Overall, this results in a trajectory that follows a random walk and that, on average, forms zero degrees with the MRSS plane. Interestingly, at 600 K kink pairs on the $+30^\circ$ plane seem to be favored in a proportion of three or more to one over -30° ones. It is unclear at this point if the dislocation core transition discussed above for EAM3 is responsible for this difference. Again, as stated in 2.3, we are reluctant to construe this as real physical behavior until more is known about the core structure transformation. Our main message from the analysis of trajectories is that despite the MRSS plane being of the $\{112\}$ family, motion proceeds by way of kink pairs on $\{110\}$ planes presumably for all potentials.

2.4 Dislocation core structure at finite temperature

As shown in Fig. 2.8, the σ - v data are not conducive to comparison among potentials. Instead, in Fig. 2.10 they are plotted as a function of interatomic potential for a number of selected temperatures. The figure reveals an interesting trend: the *relative* behavior of

all the potentials remains unchanged for all temperatures with the exception of EAM3. At low temperatures, this potential exhibits a relatively high dislocation mobility, akin to that displayed by ‘fast’ potentials such as EAM2. However, above 900 K, the mobility is reduced (relative to the other interatomic potentials) to values more in line with ‘slower’ potentials such as EAM1.

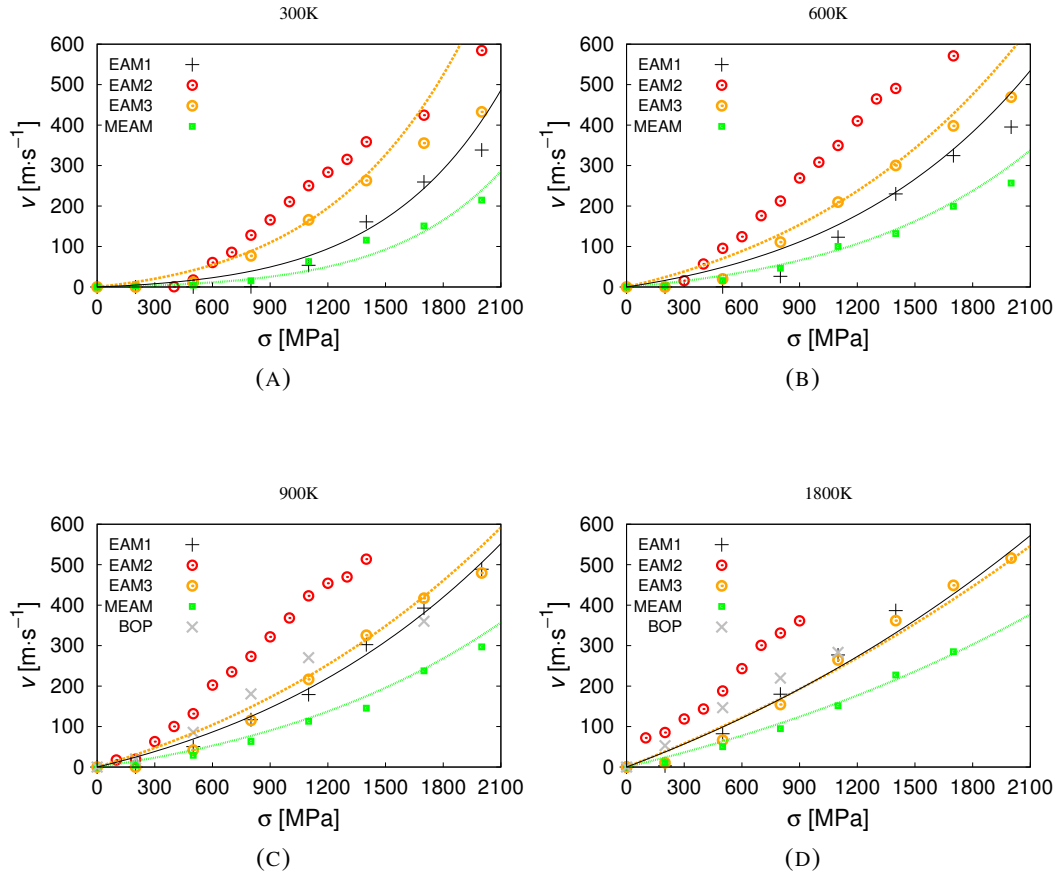


FIGURE 2.10: Comparison of interatomic potentials for the data given in Fig. 2.8. The colored lines correspond to exponential fits obtained in Section 2.5 for potentials EAM1, EAM3 and MEAM.

Moreover, if one examines the trajectories followed by the dislocation at 500 MPa², a notable difference in behavior within the EAM3 potential can be observed. At a temperature of 600 K, the dislocation follows a biased path on an effective glide plane forming $\approx 30^\circ$ with the MRSS plane. However, at 1800 K, the dislocation follows a path that deviates only slightly from that dictated by the Peach-Köhler force (*i.e* 0°). This is quantitatively displayed in Figure 2.11, where this time the trajectories are resolved with atomistic detail. The figure shows unequivocally that dislocation motion proceeds

²To be meaningful, this analysis must be performed at relatively low stresses to interfere the least amount possible with the investigated temperature effect.

via the formation of kink pairs on $\{110\}$ planes bordering the MRSS $[11\bar{2}]$ plane (at $\pm 30^\circ$). Moreover, the details of the trajectory at 600 K suggest biased formation on the $(10\bar{1})$ plane ($+30^\circ$), whereas at 1800 K *random-walk* behavior is displayed, with kink pairs forming equally on both available $\{110\}$ planes.

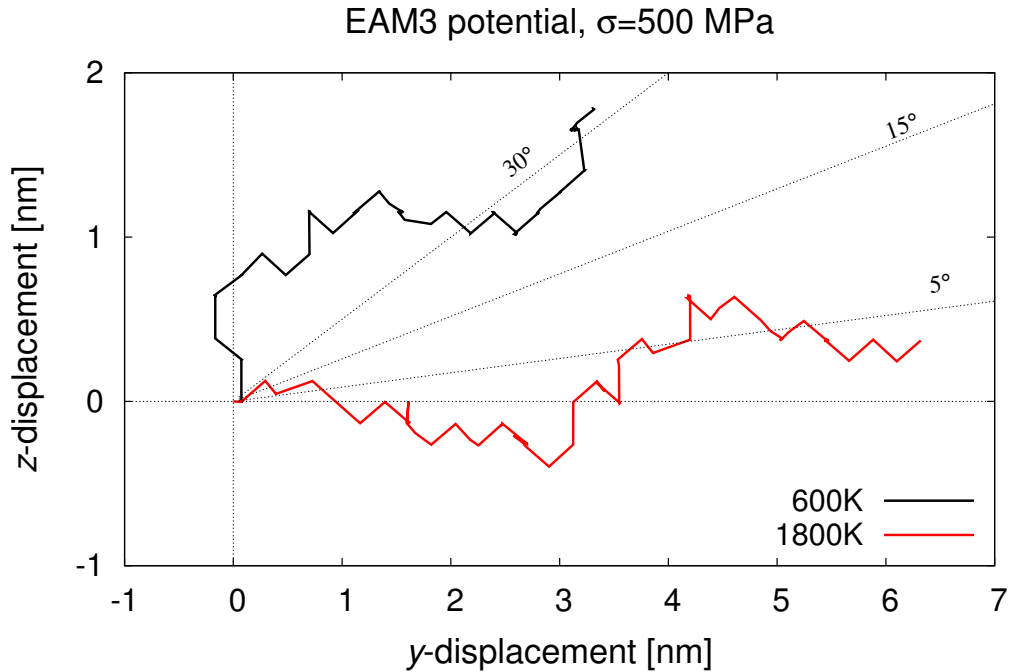


FIGURE 2.11: Line-averaged dislocation trajectories on the yz -plane for the EAM3 potential at 500 MPa. Results for two 200-ps temperatures above and below the presumed core transformation temperature of around 1200 K are shown. Planes forming 0, 5, 15 and 30° with the $(11\bar{2})$ MRSS plane are represented with dotted lines (angles not to scale).

The behaviors illustrated in Figs. 2.10 and 2.11 for potential EAM3 suggest a change in core structure with temperature for a given stress state³. To examine the physical structure of the dislocation core at different temperatures one can use time-averaged differential displacement (DD) maps (these maps were used in Table 2.1 for each 0 K configurations). The DD maps are obtained by running MD simulations of crystals containing four screw dislocations arranged in a balanced quadrupole configuration and periodic boundary conditions. The size of the simulation box is $20 \times 15 \times 18$ multiples of the bcc lattice vectors $[111] \times [\bar{1}\bar{2}\bar{1}] \times [\bar{1}01]$. The dimensions are adjusted to the equilibrium lattice constant at the given temperature. For the finite temperature simulations, the displacement of each atomic string is determined by averaging over all 40 atoms in the string and over a time window of 100 fs, being sufficiently long to avoid

³We know that stress also induces its own core transformations as explained in Ref. (Rodney & Provile, 2009).

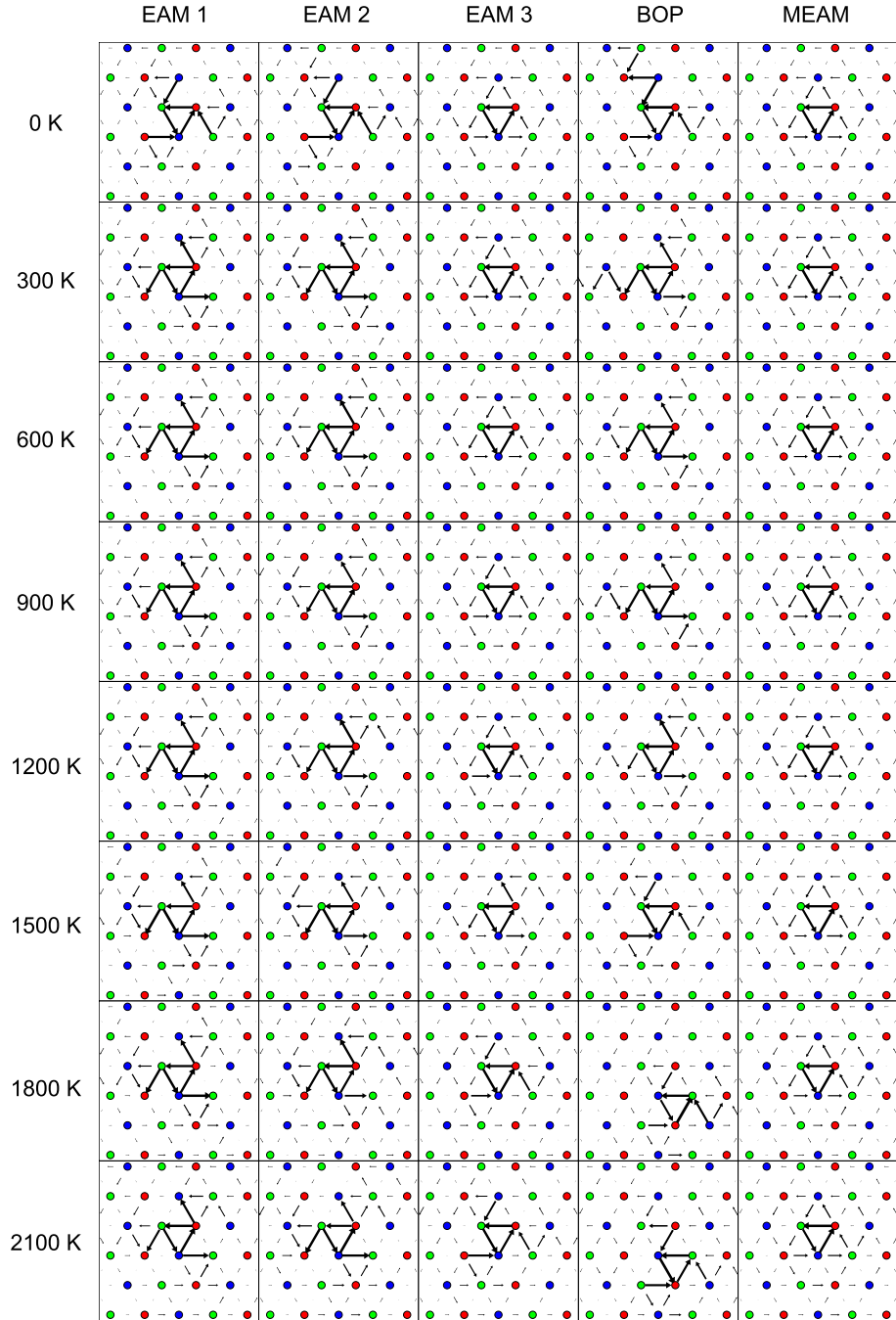


FIGURE 2.12: Time-averaged core structures for the five potentials tested here in the entire temperature range.

noise due to thermal vibrations yet short enough to not capture diffusive behavior. The results are shown in Fig. 2.12⁴ for configurations in the $0 < T < 2100$ K interval. The figure confirms that the the EAM3 core is the only one showing an appreciable transformation from non-degenerate to degenerate, clearly seen at and above 1500 K.

⁴Figure 2.12 was published in Cereceda et al. (2013) and it is courtesy of Dr. Alex Stukowski.

Although DD maps are a useful tool to quickly analyze core structures, next we complement the results in Fig. 2.12 with a more quantitative approach based on fundamental lattice properties.

Duesbery and Vitek ([Duesbery & Vitek, 1998](#)) have provided a simple rule that relates the shape of the $\frac{1}{2}\langle 111 \rangle\{110\}$ γ -surface to the core structure at 0 K. They used the following inequality:

$$\gamma\left(\frac{b}{3}\right) > 2\gamma\left(\frac{b}{6}\right),$$

to predict whether a screw dislocation will display a compact core. $\gamma\left(\frac{b}{3}\right)$ and $\gamma\left(\frac{b}{6}\right)$ are the energies corresponding to the $\frac{b}{3}$ and $\frac{b}{6}$ magnitudes of the generalized fault vectors, which can be obtained by reference to Fig. 2.2. The idea is that, if the above inequality is satisfied, $\frac{b}{6}$ -type faults will be preferred over $\frac{b}{3}$ ones, leading to non-dissociated core structures. However, although Duesbery and Vitek applied this simple rule to six different bcc metals⁵ with remarkable success, we find that in our case it does not hold for potentials EAM1 and EAM2. Thus, here we try a different approach based on the analysis carried out by Gilbert and Dudarev ([Gilbert & Dudarev, 2010](#)).

These authors have shown that, alternatively, the $\frac{1}{2}\langle 111 \rangle$ screw dislocation core structure in bcc systems can be related to the periodic interaction energy between adjacent $\langle 111 \rangle$ strings of atoms forming the crystal. Their analysis, which was performed primarily to help guide potential development, provides a framework to predict whether the favored core structure at 0 K is compact or dissociated. In particular, they derive the so-called “first-nearest-neighbour (1NN) inter-string interaction law” of the potential and use this in a 2D Frenkel-Kontorova (2D-FK) model of interacting $\langle 111 \rangle$ strings to find the minimum energy screw core-structure. Here we extend their methodology to finite temperatures using the quasiharmonic approximation, *i.e.* by relating volume changes to temperature via pre-computed thermal expansion coefficients for each potential. In this fashion, we first compute the inter-string interaction laws as a function of the lattice parameter and then obtain the equivalent temperature as: $T = 3(a/a_0 - 1)/\alpha$. Here, α is the thermal expansion coefficient (given for each potential in Table 2.1), a_0 the lattice parameter at 0 K, and a the lattice parameter corresponding to a temperature T (within the quasiharmonic approximation). For the remainder of this section, we refer to a as $a(T)$ to highlight this temperature dependence.

For each temperature T the 1NN inter-string interaction law $U_1(d)$ was derived by rigidly translating a single $\langle 111 \rangle$ string with respect to a perfect lattice with lattice

⁵V, Cr, Nb, Mo, Ta, and W, all described by Finnis-Sinclair potentials ([Finnis & Sinclair, 1984](#))

parameter $a(T)$ and measuring the associated variation in energy under the particular interatomic potential. The resulting curve, which, according to the 2D-FK model defined in Ref. ([Gilbert & Dudarev, 2010](#)), is dominated by the contributions from the moving string interacting with its six 1NNs, can be unfolded using a Fourier analysis to produce the required pair-wise interaction law for the 2D-FK model. An example of such a law for EAM3 at 0 K is shown in figure 2.13(b). A perfect screw dislocation, inserted into a lattice of $\langle 111 \rangle$ atomic strings (for a given $a \equiv a(T)$) according to the isotropic elasticity solution, was then relaxed using $U_1(d)$ and the nature of the relaxed core was determined by visual inspection of its differential displacement map.

Figure 2.13(a) shows the variation in the favored core structure as a function of T for each of the five potentials. On the y -axis of the plot we have calculated the ratio of the string separation d^* associated with the inflection points in the corresponding $U_1(d)$ law (highlighted by the vertical dotted lines in figure 2.13(b)) to $b(T)/6$, where $b(T)$ is the corresponding Burgers vector of each potential as a function of T .

As observed by Gilbert and Dudarev ([Gilbert & Dudarev, 2010](#)), the favored core structure depends on the position of the inflection points of the $U_1(d)$ function. Specifically, a fully compact core is characterized by minimum string separations of $b(T)/6$, which are the in-line separation distances between each of the three $\langle 111 \rangle$ strings immediately surrounding the core (red circles in Figure 2.13(c), which shows a differential displacement map for a compact core) and their two nearest strings forming the next shell of strings out from the core (blue circles in 2.13(c)). When the inflection points in $U_1(d)$ are located at a distance of less than or equal to $b(T)/6$, then the compact, non-dissociated core is always stable. Furthermore, even if the separations d^* associated with $U_1''(d) = 0$ are such that $|d^*|$ is somewhat greater than $b(T)/6$, the compact core may still be stable provided that U_1 is only slowly varying around these inflection points —meaning that the forces ($-U_1'(d)$) between strings are relatively constant over a range of d values. This, for example, is the situation in the case of the MEAM potential in Fig. 2.13(a), where the ratio $d^*/(b(T)/6)$ is greater than one for all T , but the favored core remains compact.

However, when the ratio is significantly greater than one, as is the case for both EAM1 and EAM2 at all temperatures, then the compact core becomes unstable and the secondary strings out from the core tend to move towards (along $\langle 111 \rangle$) one of their primary-string neighbors (signified by the major arrows in the “arms” of the non-compact core shown for EAM1 in Table 2.1)—ultimately leading to the stabilization of the non-compact, three-fold symmetric dissociated core.

Thus, if, as a function of T , there is significant variation in this ratio, then the preferred equilibrium core structure can also change. In our analysis, we find that, consistent with the transition observed in Fig. 2.12, there is a large shift for EAM3 in the value of $d^*/(b(T)/6)$ (d^* is such that $U_1''(d^*) = 0$) above ~ 1500 K. At this point, the equilibrium core structure diverges from the compact core, and becomes more and more dissociated as temperature increases further.

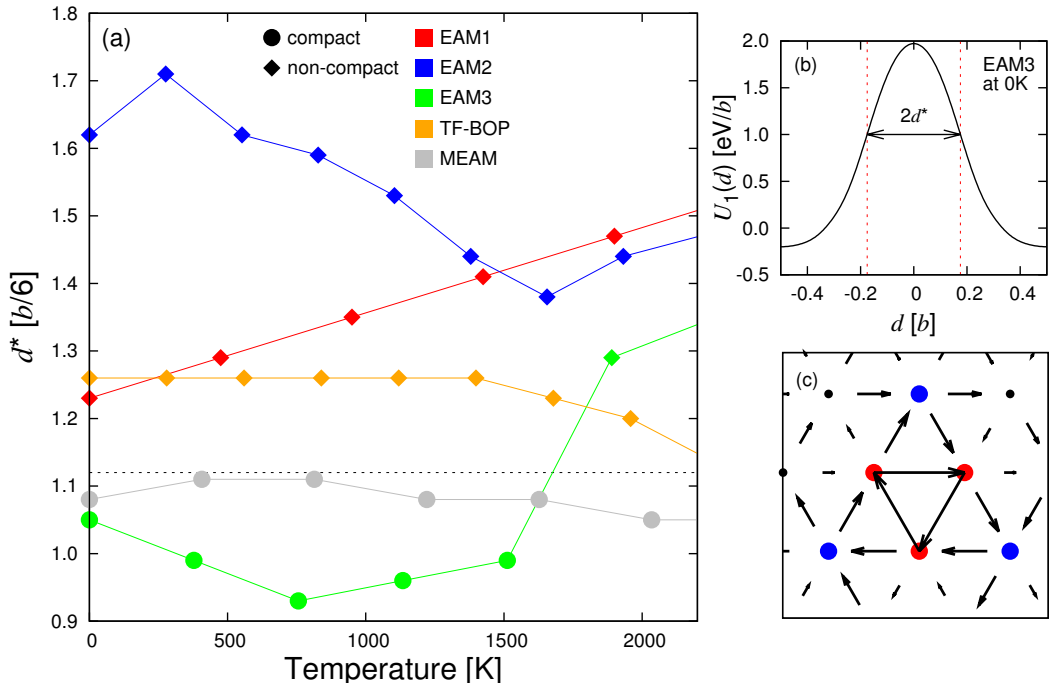


FIGURE 2.13: (a) Analysis of the favored core structure for the five different potentials as a function of temperature. A compact core is designated by a circle, and a non-compact by a diamond. The y -position of each point is the magnitude of distance of the inflection points in the 1NN string-interaction law (*i.e.* d^* , which is the distance at which $U_1''(d) = 0$) normalized to the quantity $b(T)/6$, where $b(T) = \sqrt{3}a(T)/2$. The dashed horizontal line separates the region of phase space where compact cores are favored (below) from the region where non-compact are favored (above). (b) The 1NN string-interaction law for EAM3 at 0 K. The red dashed vertical lines indicate the position of the inflection points in this curve. (c) Differential displacement map of the compact core predicted at 0 K for the U_1 function from EAM3. Each of the three strings closest to the core (red circles) are separated from their two closest secondary strings (blue circles) by $b/6$. In the figure the temperature dependence of b is omitted for the sake of clarity.

The behavior that emanates from the results in Figs. 2.10 and 2.11 for potential EAM3 is the manifestation of a temperature-driven dislocation core transformation that occurs as a result of changes to the free energy landscape. We have characterized this transformation via differential displacement maps of time-averaged atomic positions at finite temperatures, and a quasiharmonic analysis of the location of inflection points in the

$\langle 111 \rangle$ interaction energy, which is known to control the dislocation core structure (cf. Figs. 2.11 and 2.13⁶).

This is seen to affect the dislocation mobility as well. We have shown that the reported core transformation has an impact on both the stress and temperature dependencies. Indeed, in the analysis carried out in Section 2.5, it is shown that the temperature dependence of fitted σ - v relations at $T < 1200$ K for EAM3 does not carry over to higher temperatures. By contrast, the same analysis does not yield significant differences between the low and high temperature regimes for potentials EAM1 and MEAM. This is further indication that the core structure may impact the motion mechanisms in the corresponding temperature range.

We emphasize, however, that as long as there does not exist independent evidence of this dislocation core structural change with temperature, the discussion about its true impact on the dynamic behavior of screw dislocations remains solely speculative, and we cautiously warn against using the EAM3 potential above the observed transformation temperature of ≈ 1500 K. In this sense, the quasi-harmonic analysis performed in Section 2.4 would be very amenable to DFT calculations, as it consists solely of zero-temperature calculations. This would provide an independent means to prove or disprove –at least within the limitations of the quasi-harmonic analysis– the behavior predicted by EAM3 at high temperature.

2.5 Impact of the dislocation core transition on dislocation mobility

Here we analyze the overall impact of the dislocation core transition for potential EAM3 on dislocation mobility. We fit the data given in Fig. 2.8 to the general expression:

$$v(\sigma, T) = A\sigma \exp\left(-\frac{H_0 - \sigma V^*}{kT}\right) \quad (2.1)$$

where A , H_0 , and V^* are fitting constants that represent, respectively, a velocity prefactor, the kink pair energy at 0 K, and the activation volume. We obtain these for three potentials, namely, EAM1, EAM3, and MEAM, and carry out the fit first including all temperatures. The results for each case are shown in Table 2.2. These values deserve

⁶Figure 2.13 was published in Cereceda et al. (2013) and it is courtesy of Dr. Mark Gilbert.

TABLE 2.2: Fitting parameters for the analytical mobility function 2.1. The average fitting error for A , H_0 , and V^* was, respectively, 6, 9 and 10%. Regular script: values from full temperature fits; bold script: values from low temperature (≤ 900 K) fits; in parentheses: percentage difference between both sets of fits.

Potential	A [$\text{ms}^{-1}\text{MPa}^{-1}$]	H_0 [eV]	V^* [b^3]
EAM3	0.26 0.24 (8%)	0.05 0.04 (20%)	0.42 0.19 (55%)
MEAM	0.19 0.17 (10%)	0.08 0.07 (12%)	0.26 0.23 (12%)
EAM1	0.30 0.28 (7%)	0.08 0.07 (12%)	0.24 0.24 (0%)

some commentary, particularly H_0 and V^* . Using the method described by [Ventelon & Willaime \(2007\)](#), we have obtained a kink-pair energy of $H_0 = 1.7$ eV for the MEAM potential. Experimentally, [Brunner \(2000\)](#) has obtained a value of 1.75 eV from the temperature dependence of flow stress measurements in W, in very good agreement with the calculated value but significantly higher than the MD values. [Giannattasio et al. \(2007\)](#) have obtained values of the order of 1.0 eV inferred from the strain rate dependence of the brittle-to-ductile transition, still much larger than those reported here. Similarly, [Tarleton & Roberts \(2009\)](#) have found values of $V^*=20b^3$ to be representative of the kink-pair process in W. Again, these are two orders of magnitude larger than ours. The magnitudes of H_0 and V^* obtained in our analysis suggest a very ‘soft’ thermally activated process, something not necessarily consistent with the static data presented in Section 2.2. The low values of H_0 and V^* obtained in our simulations are likely due to overdriven screw dislocation dynamics in the MD simulations.

Next, we obtain additional fits using only data at 300, 600, and 900 K, *i.e.* at temperatures below the presumed core transformation for potential EAM3. The corresponding parameter values are shown in bold script for each case in Table 2.2. The percentage difference between the values for full and low temperature fits is given in parentheses. Although the differences in the parameter A are similar in all cases, those for H_0 and V^* are clearly largest for EAM3. Particularly, the differences in the activation volume, which is known to be most sensitive to the core structure, are considerable. This further reinforces the notion that, from a dynamical standpoint, dislocations are behaving differently below and above ≈ 1000 K. In contrast, for the other two potentials, the dynamic behavior above and below this presumed transition temperature is governed by the same laws. The low temperature fits obtained here are shown in Fig. 2.10. The fits provide very good agreement with the EAM1 and MEAM data at all temperatures, whereas they gradually worsen for EAM3 as temperature increases. As well, the deviation of the fits above σ_P for potential EAM3 can be clearly appreciated.

2.6 Summary

To summarize, the main findings of this chapter can be condensed into the following main items:

- We have calculated static properties relevant to screw dislocations using five different interatomic potentials for W. These include three EAM, one BOP and one MEAM.
- We have seen that simple 'ramps' as short as 10 ps may be sufficient to dampen stress oscillations to a level that requires nearly 200 ps to reach when stress is applied as a sudden step. It is not clear how other non-linear, albeit still smooth, functions will perform, although it is to be expected that they will behave similarly to the linear ones tried here.
- We have calculated screw dislocation mobilities for all potentials on a {112} glide plane. Our calculations provide elements to judge the MEAM potential as the most suitable for dislocation calculations.
- We have observed a temperature-induced dislocation core transformation –from compact to dissociated– for one of the potentials tested. Lacking independent confirmation, we cannot confirm whether this corresponds to a real physical phenomenon or is an artifact, but the transformation is indeed seen to impact the dynamic properties of dislocations.
- Our analysis of the five interatomic potentials suggests, first, that the atomistic nature of the dislocation core governs behavior at larger scales and, second, a purely static treatment of the dislocation core is insufficient to predict and describe the dynamics of dislocations.

Chapter 3

Nudged Elastic Band simulations of kink pairs

3.1 Introduction

The movement of dislocations can be considered as a set of successive processes that define a pathway through the potential energy landscape. Each of these processes happens between two configurations of atoms that are local minima corresponding to straight dislocations in equilibrium, providing information about the activation energy of the process and what intermediate equilibrium configurations may exist along the transition.

The nucleation and propagation of kink pairs between these local minima appears to be one of the underlying mechanisms that explain some of the characteristics of the motion of dislocations.

Below, we describe the general ideas on how these processes are studied by the ‘nudged elastic band’ (NEB) method discussed in more detail by *Henkelman et al.* ([Henkelman et al., 2000](#)) and by *Tadmor and Miller* in section 6.3.1 of the book *Modeling Materials* ([Tadmor & Miller, 2011](#)).

In the NEB method, a replica of a system with N atoms is defined by a $N \times 3$ matrix that contains the positions of all the atoms in the system, $\mathbf{P} = (\mathbf{r}^1, \mathbf{r}^2, \dots, \mathbf{r}^N)$. Given a total number of R replicas to study the movement of a dislocation between two consecutive Peierls valleys, the first and last replicas, \mathbf{P}^1 and \mathbf{P}^R , are at local energy minima in the

energy landscape. All the other intermediate replicas can be characterized in different ways, but they are not in equilibrium, exhibiting a force on the atoms of each replica i that comes from the non-zero gradient of the potential energy

$$\mathbf{F}_{pot}^i = -\nabla_P V(\mathbf{P}^i) = \{-\nabla_{r^1} V|_{P^i}, \dots, -\nabla_{r^N} V|_{P^i}\} \quad (3.1)$$

The minimization of these forces would displace each intermediate replica to one of the local minima. In the NEB method, replicas 1 and R are fixed, and each intermediate replica is connected to the previous and next replica by a spring of constant k . These springs introduce a new force \mathbf{F}_{spring}^i that depends on the value of the spring constant. If k is small, the spring forces will not affect the minimization and the replicas will fall to one of the local minima. If k is big, the replicas are more rigid, and the spring forces will define a higher-energy path.

Considering the combined action of these two types of forces, the 3N-dimensional force on replica i , \mathbf{F}^i , is defined as

$$\mathbf{F}^i = \mathbf{F}_{pot}^i|_{\perp} + \mathbf{F}_{spring}^i|_{\parallel}, \quad (3.2)$$

where

$$\mathbf{F}_{pot}^i|_{\perp} = \mathbf{F}_{pot}^i - (\mathbf{F}_{pot}^i \cdot \mathbf{t}^i)\mathbf{t}^i, \quad \mathbf{F}_{spring}^i|_{\parallel} = k(\|\mathbf{P}^{i+1} - \mathbf{P}^i\| - \|\mathbf{P}^i - \mathbf{P}^{i-1}\|)\mathbf{t}^i, \quad (3.3)$$

\mathbf{t}^i is the 3N-dimensional tangent to the path at replica i , $\mathbf{F}_{pot}^i|_{\perp}$ is the component of the forces derived from the potential energy that is perpendicular to the path and $\mathbf{F}_{spring}^i|_{\parallel}$ is the component of the spring forces acting parallel to the path. In this distribution of forces, $\mathbf{F}_{pot}^i|_{\perp}$ will attempt to move each replica vertically to the minima and $\mathbf{F}_{spring}^i|_{\parallel}$ will attempt to move it along the reaction coordinate. The minimum energy path (MEP) between Peierls valleys can now be obtained by running an algorithm that moves the atomistic configurations of all the replicas until the global force defined in Eq.3.2 is reduced to zero.

3.2 Computational details

The principal axes x , y , and z , of the simulation box were oriented along the $\frac{1}{2} [1\ 1\ 1]$, $[\bar{1}\ 2\ \bar{1}]$, and $[\bar{1}\ 0\ 1]$ directions, corresponding to the line, glide and normal directions, respectively, of the screw dislocation. The dimensions of the simulation box were chosen to maximize the physical fidelity of the results while keeping the computational cost manageable. According to these criteria the dimensions are: $L_x = 27.2$ nm (100 \mathbf{b}), $L_y = 10.8$ nm, and $L_z = 10.7$ nm, with a total number of 208300 atoms.

Two screw dislocations with Burgers vector $\mathbf{b} = \frac{1}{2} [1\ 1\ 1]$ are generated by using the isotropic elastic displacement solution (Hull & Bacon, 1984) in two independent simulation boxes (one dislocation per box) with the orientation and dimensions described before. The first dislocation d_1 is generated at the center of the box. The second dislocation d_2 is generated at a distance of $\frac{\sqrt{6}}{3} a_0^1$ from the center of the simulation box along the glide direction $[\bar{1}\ 2\ \bar{1}]$, which corresponds to the distance between two consecutive Peierls valleys in that direction.

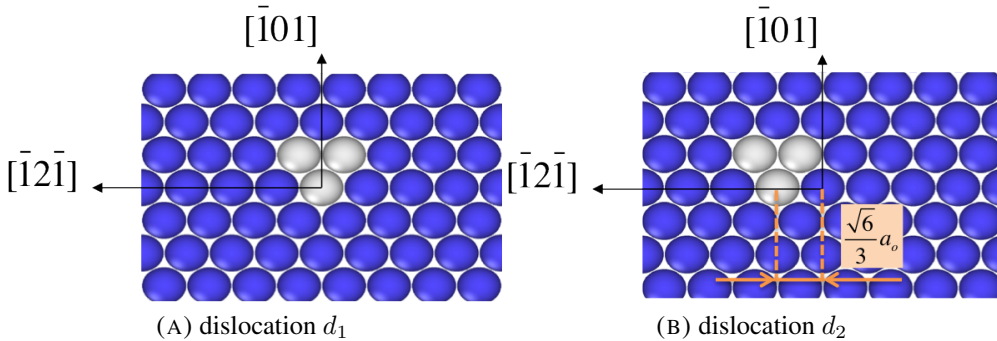


FIGURE 3.1: Position of the first d_1 and second d_2 dislocation with $(\bar{1}\ 0\ 1)$ plane .

Prior to the NEB simulations, dislocations d_1 and d_2 are relaxed using the conjugate gradient algorithm implemented in LAMMPS (Plimpton, 1995). Periodic boundary conditions are applied in the x direction while non-periodic and shrink-wrapped boundary conditions are applied in the y and z directions.

A stress range from zero to the Peierls stress of the potential is studied by applying shear stress σ_{xz} . To reproduce the effect of this applied stress, an external force f_x is added to the atoms in the top and bottom surfaces along the normal direction $[\bar{1}\ 0\ 1]$. The external force per atom satisfies $f_x = \frac{\sigma L_x L_y}{N_s}$, where σ is the desired stress and N_s is the number of atoms in each surface.

¹ a_0 is the lattice parameter of the interatomic potential used in the simulations.

The MEP is obtained using the NEB method described before (Henkelman & Jonsson, 2000; Henkelman et al., 2000; Nakano, 2008; Plimpton, 1995). In this work we present two different types of NEB simulations depending on the intermediate configurations: straight dislocations or kink-pairs. Both of them use a total of 31 replicas, a spring constant of 1 eV Å⁻¹ and set relaxed dislocations d_1 and d_2 as the initial (1) and final (R) configurations respectively.

In this work we have used two different interatomic potential parameterized for tungsten: a embedded-atom method (EAM) potential (Marinica et al., 2013) and a modified embedded-atom method (MEAM) potential (Park et al., 2012). Both of them predict the correct symmetric core structure at 0 K. They predict a Peierls stress of 2.03 and 3.2 GPa, repectively.

3.3 Results

3.3.1 Enthalpy and Energy barriers

Straight dislocations

For the study of a straight dislocation moving between two consecutive Peierls valleys along the glide direction, the initial coordinates of all the atoms in the intermediate replica i , \mathbf{P}_0^i , are set to values linearly interpolated between the corresponding atoms in replicas 1 and R.

$$\mathbf{P}_0^i = \mathbf{P}^1 + \frac{i - 1}{R - 1} (\mathbf{P}^R - \mathbf{P}^1), \quad (3.4)$$

where $i=2 \dots R-1$.Therefore, the initial path of the NEB simulation contains a single dislocation for every replica.

The dimension along the dislocation line is reduced to $L_x = 1.36$ nm (5 **b**). In contrast with the study of kink-pairs where a value of $L_x = 27.2$ nm (100 **b**) is required for the nucleation of the kinks, this reduced size of the box is big enough for the straight dislocation to reproduce the physical fidelity of the results while decreasing the computational cost of the simulations.

For a given replica i , its enthalpy, H_i , includes the contribution of the internal energy and the mechanical work generated by the applied stress

$$H_i = U_i - \sigma \cdot b \cdot L_x \cdot \theta_r, \quad (3.5)$$

where U_i is the internal energy of the replica, σ is the applied stress and θ_r is the reaction coordinate along the MEP. The enthalpy barrier per unit length is represented in Fig.3.2 as the difference between the enthalpy of each replica and the enthalpy of the initial configuration of the NEB simulation. One can notice that the increase in the applied stress increases the negative slope of the enthalpy barrier and decreases the maximum value achieved.

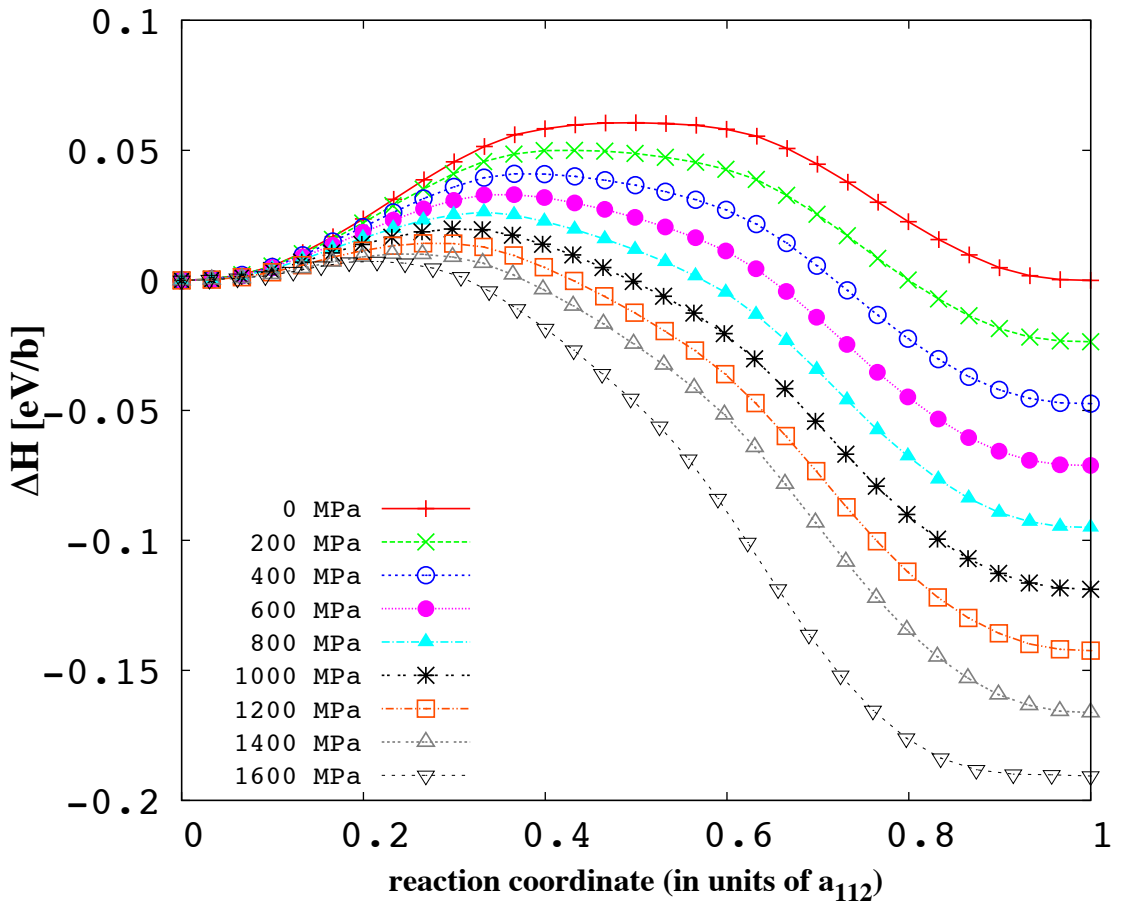


FIGURE 3.2: Enthalpy barrier per Burgers vector for a straight screw dislocation with normal plane $(\bar{1}01)$, computed with the NEB method using the EAM potential under the full range of applied stress.

According to Eq.3.5, the energy barrier is obtained by adding the mechanical work to the enthalpy. Similar to the enthalpy barrier, the energy barrier per unit length is represented in Fig.3.3.a as the difference between the energy of each replica and the energy of the initial configuration of the NEB simulation. In Fig.3.3.b, energies and reaction coordinates were shifted to overlap the potential minima for the different applied stresses ([Provile et al., 2013](#)).

In addition to the study of the $\frac{1}{2}\langle 111 \rangle\{110\}$ screw dislocation, the Peierls potential for the $\frac{1}{2}\langle 111 \rangle\{112\}$ screw dislocation was also studied. In this case the directions $\frac{1}{2}[111]$, $[10\bar{1}]$, and $[\bar{1}2\bar{1}]$ correspond to the line, glide and normal directions of the simulation box respectively. The second dislocation d_2 is generated at a distance of $\sqrt{2}a_0$ from the center of the simulation box along the new glide direction $[10\bar{1}]$. For this orientation of the system Fig3.4.b shows a MEP with two barriers to move the straight dislocation between two consecutive Peierls valleys along the $(\bar{1}2\bar{1})$ plane. These results, in addition to the results of Fig.3.5.a, where the energy barriers along the $(10\bar{1})$ and $(\bar{1}2\bar{1})$ planes are plotted together at 0 MPa, suggest that the MEP along the $(\bar{1}2\bar{1})$ plane can be explained as two partial MEP along the $(10\bar{1})$ plane. Therefore the study of the kink-pair enthalpy has been completed only for the $\frac{1}{2}\langle 111 \rangle\{110\}$ system.

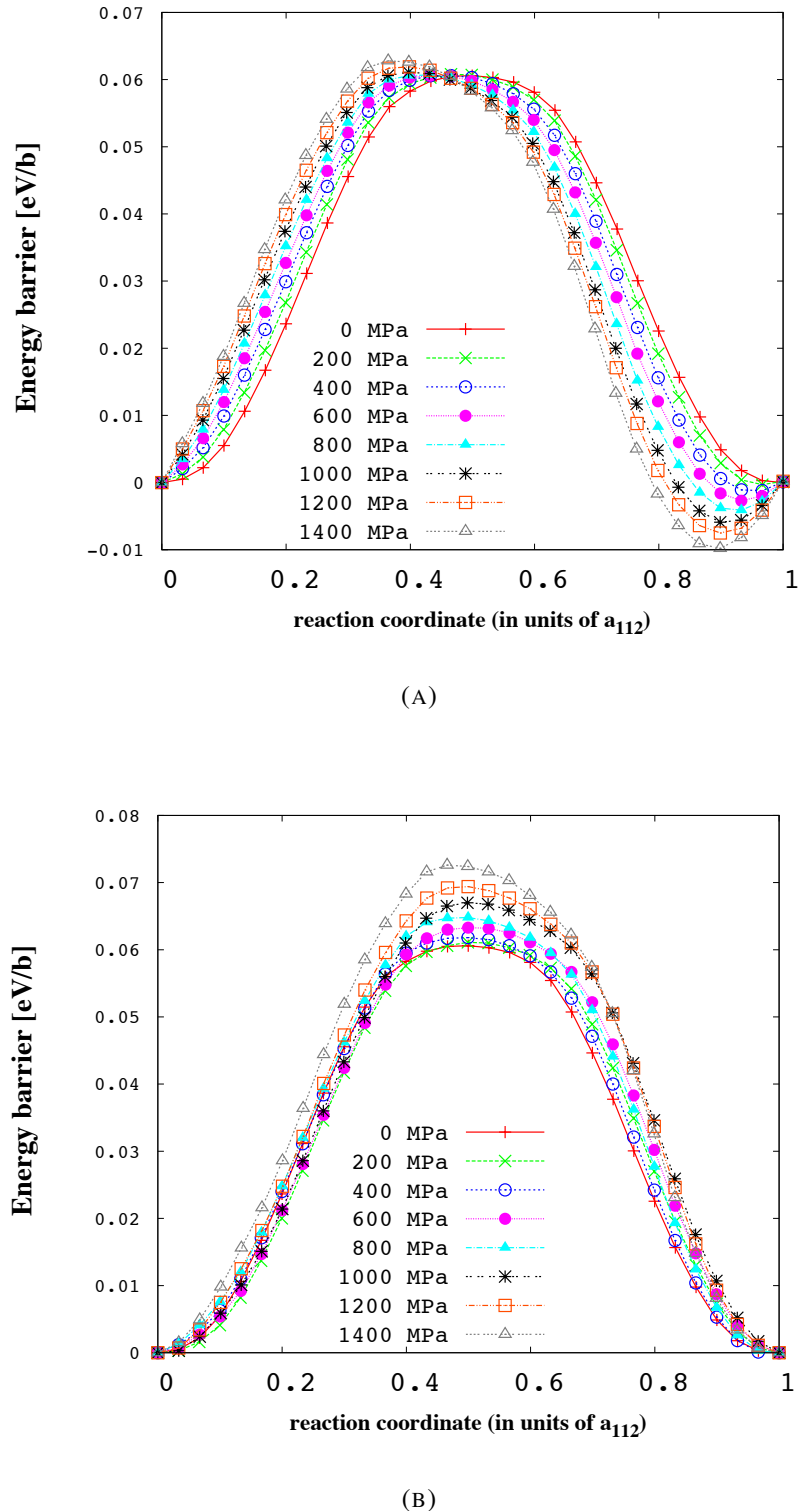


FIGURE 3.3: Energy barrier per Burgers vector for a straight screw dislocation with normal plane $(10\bar{1})$ and EAM potential.

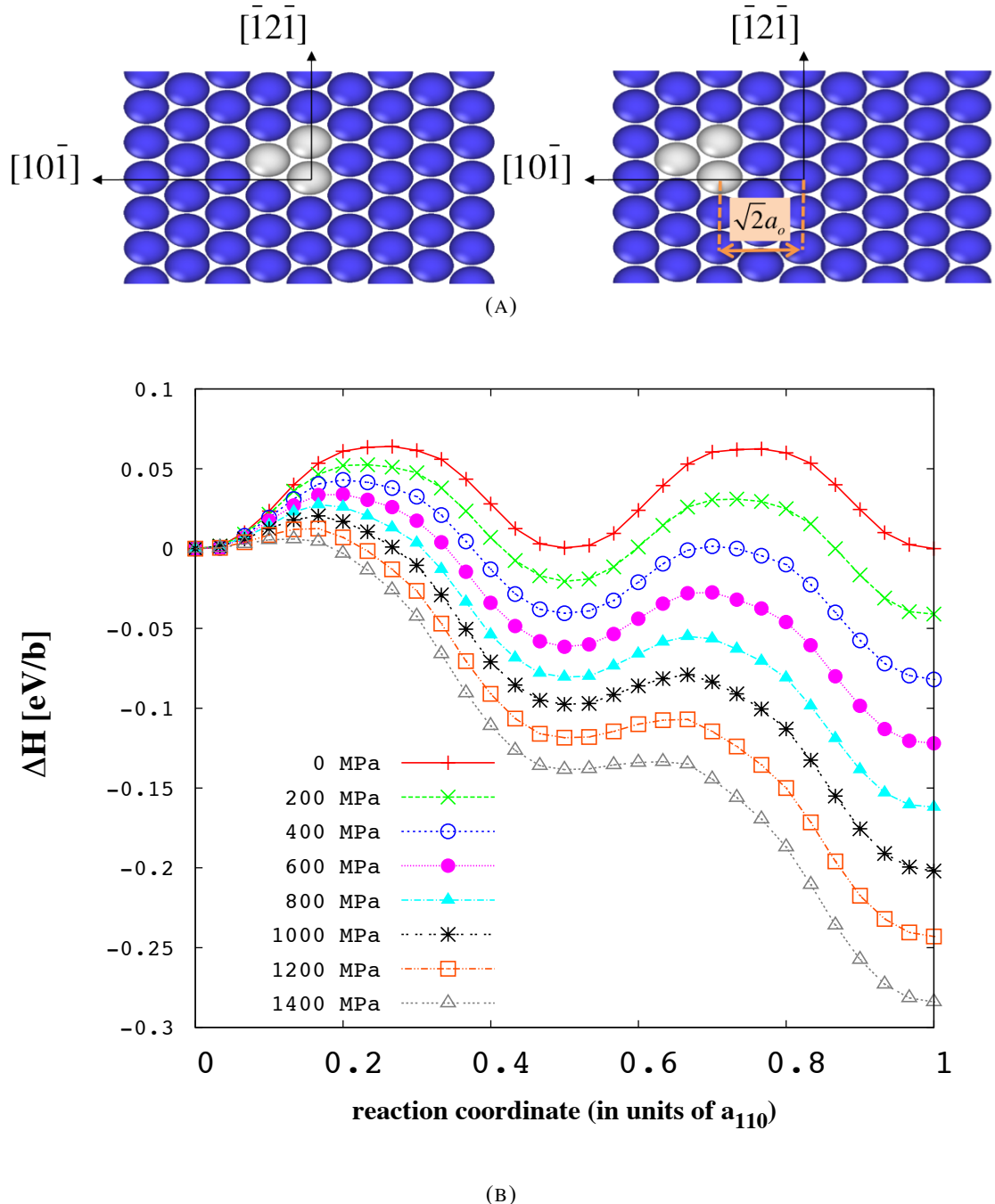


FIGURE 3.4: (a) Position of dislocations d_1 and d_2 when the screw is oriented with $(\bar{1} 2 \bar{1})$ as the normal plane. (b) Enthalpy barrier per Burgers vector for a straight screw dislocation with normal plane $(\bar{1} 2 \bar{1})$, computed with the NEB method using the EAM potential.

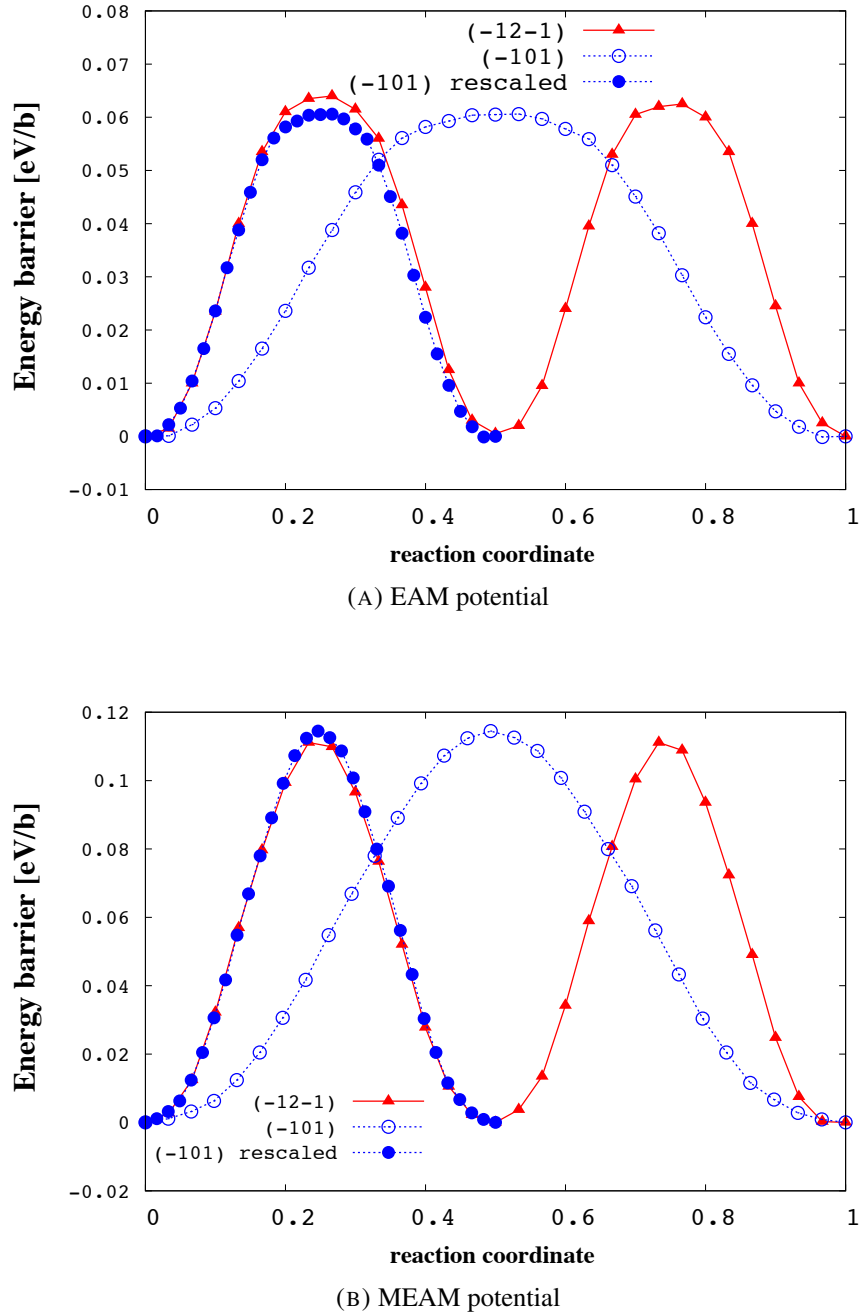


FIGURE 3.5: Energy barrier at 0 MPa for the $(\bar{1}01)$ and $(\bar{1}2\bar{1})$ planes versus the reaction coordinate in units of the glide direction, $[\bar{1}2\bar{1}]$ and $[101]$ respectively.

The enthalpy and energy barriers have also been computed for more accurate and more expensive (Cereceda et al., 2013) MEAM potential. The results of Fig.3.6.b and the comparison between Fig.3.5.a and Fig.3.5.b reflect a more sinusoidal behavior of the MEAM potential, in agreement with the results of all the bcc transition metals (Weinberger et al., 2013).

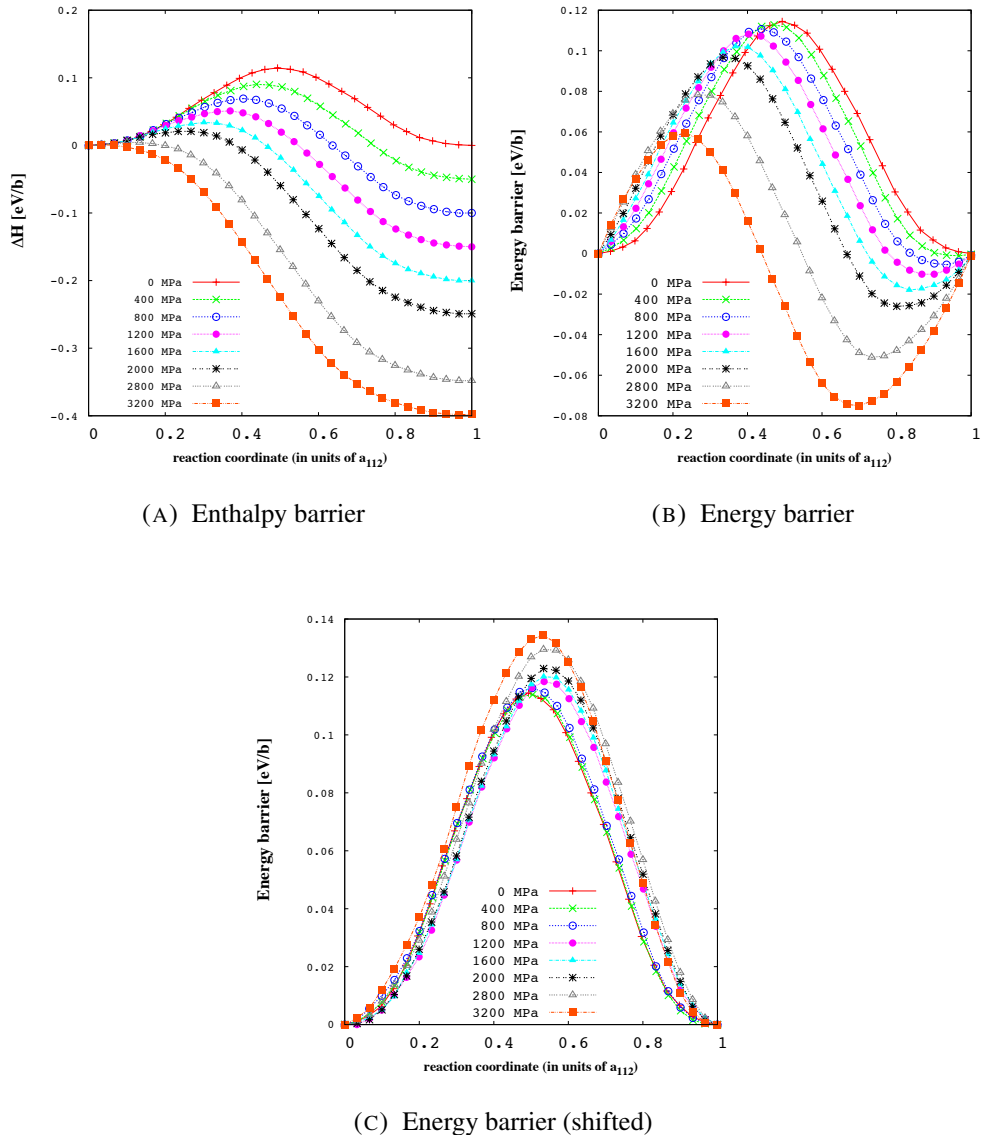


FIGURE 3.6: Enthalpy and energy barriers versus the reaction coordinate in units of the glide direction, $\overline{1} \ 2 \ \overline{1}$, for the MEAM potential.

Kink-pairs

For the study of the enthalpy and energy barriers in kink-pairs, the initial configurations of the intermediate replicas 2, 3, … R-1 contain a kink pair in the simulation box. The width of the kink pair w depends on the number of the replica i as follows

$$w_i = 0.5 \left(1 + \frac{i - 2}{R - 2} \right) L_x, \quad (3.6)$$

where $i=2 \dots R-1$. The initial coordinates of the atoms in the intermediate replicas correspond to the initial configuration except for a region of width w_i around the YZ central plane where atomic positions are taken from the final configuration ([Rodney & Provile, 2009](#)).

In this case, the initial path of the NEB simulation contains a single dislocation for the initial and final replica, and a kink pair for the intermediate replicas 2 … R-1.

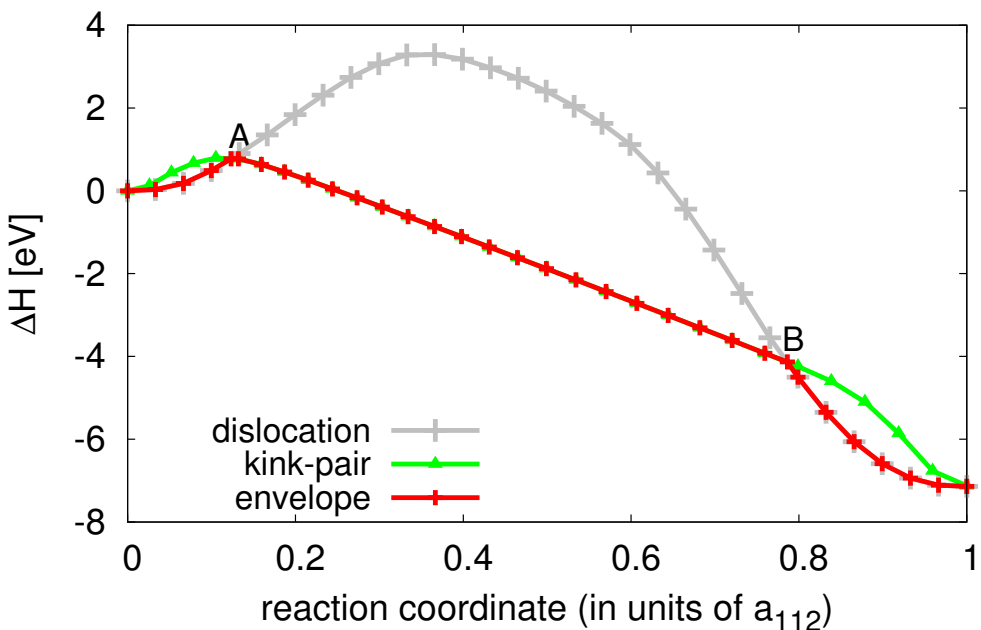


FIGURE 3.7: Enthalpy barrier when the initial configurations of the intermediate replicas are straight dislocations, kink-pairs, and the resultant envelope of minimum enthalpy of this two cases for the EAM potential at 600 MPa.

For each value of applied stress, the real pathway between two consecutive Peierls valleys is defined by the envelope of minimum enthalpy when overlapping the enthalpy barriers of the straight dislocation and the kink-pair.

$$H_{MEP}(i) = \begin{cases} H_{disloc}(i) & \text{if } H_{disloc}(i) \leq H_{kp}(i) \\ H_{kp}(i) & \text{if } H_{disloc}(i) < H_{kp}(i) \end{cases}, \quad (3.7)$$

where $H_{MEP}(i)$ is the enthalpy of the replica i defined by the MEP, $H_{disloc}(i)$ is the enthalpy of the replica i at the end of the NEB simulation when the initial configurations of the intermediate replicas are straight dislocations and $H_{kp}(i)$ is the enthalpy of the replica i at the end of the NEB simulation when the initial configurations of the intermediate replicas are kink-pairs.

The point A in Fig.3.7 where the enthalpy barriers of the straight dislocation and the kink-pair intersect represents the state where the kink-pair is nucleated, and it defines, for a specific applied stress, the enthalpy and width of the kink-pair. The point B where the enthalpy barriers of the straight dislocation and the kink-pair also intersect, but in this case with a negative slope, represents the state where the kink-pair is totally expanded and becomes a straight dislocation situated in the next Peierls valley. All the replicas in the segment \overline{AB} contain a kink-pair with an increased width.

3.3.2 Kink-Pair Enthalphy

The interest of obtaining the kink-pair enthalpy as a function of the stress comes from the important role that this variable plays when defining the nucleation rate of a kink-pair, j_{kp} . This nucleation rate can be defined as:

$$j_{kp} = \nu_0 \exp \left\{ -\frac{\Delta F_{kp}}{2kT} \right\} \quad (3.8)$$

where ν_0 is an attempt frequency, k is Boltzmann's constant, T is the temperature and ΔF_{kp} is the (Gibbs) free energy difference resulting from the nucleation of an embryonic kink pair, i.e. one with the minimum lattice separation. The $1/2$ factor arises from the fact that it is only necessary to take the dislocation to the activated state (saddle point) to achieve a transition. This is only appropriate for cases where the free energy landscape is symmetric about the midpoint of the reaction coordinate. Since figures 3.3.b and 3.6.c are mostly symmetric and bcc metals reflect a sinusoidal behavior (Weinberger et al., 2013), our case of study satisfies the conditions to use the $1/2$ factor.

The free energy can be defined as:

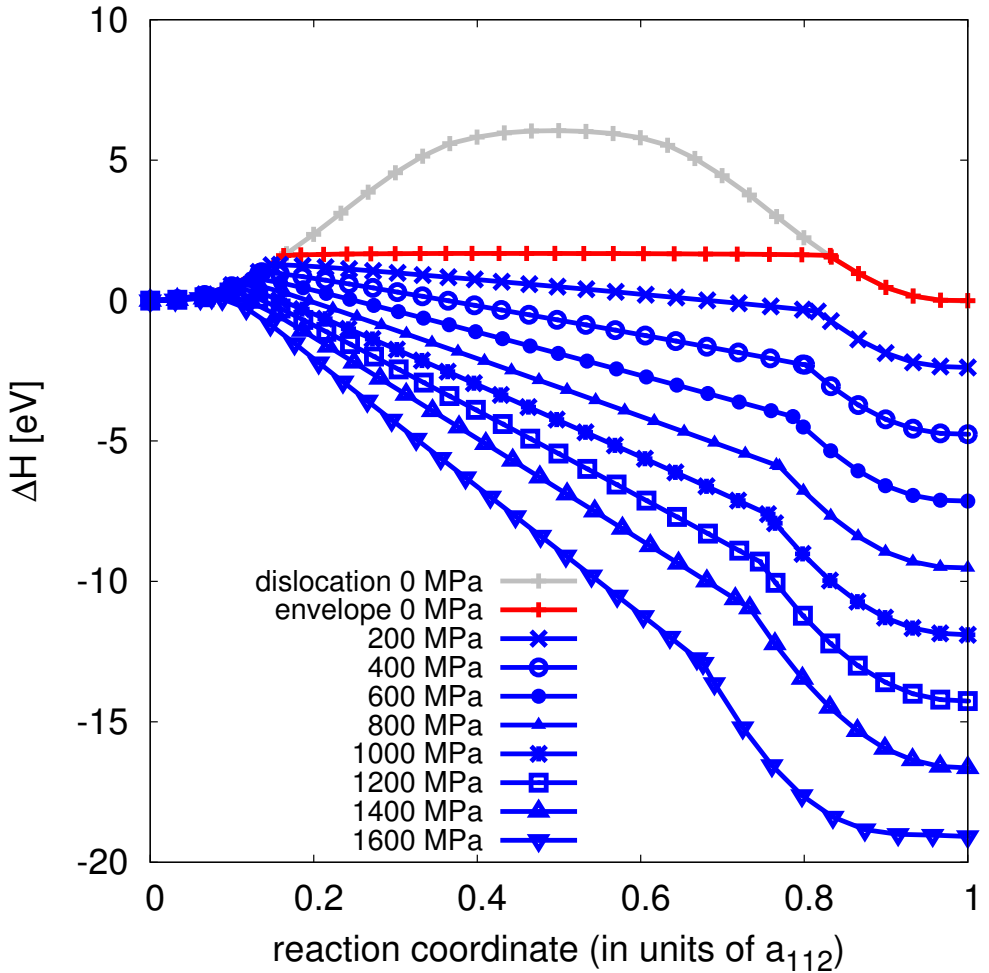


FIGURE 3.8: Enthalpy barrier of the straight dislocation at 0 MPa and the envelope of minimum enthalpy for the full range of applied stress 0 - 1600 MPa and EAM potential.

$$\Delta F_{kp} = \Delta H - T\Delta S \quad (3.9)$$

where ΔH is the enthalpy and ΔS the entropy. Assuming that the entropy can be taken as $\Delta S \sim 3k$, the enthalpy is the missing variable to compute the nucleation rate of the kink-pair.

where ΔH is the enthalpy and ΔS the entropy. Assuming that the entropy can be taken as $\Delta S \sim 3k$, the enthalpy is the missing variable to compute the nucleation rate of the kink-pair.

The atomistic data in Fig. 3.9 shows the dependence of the kink-pair enthalpy as a function of the applied stress. It results from obtaining, for each value of applied stress,

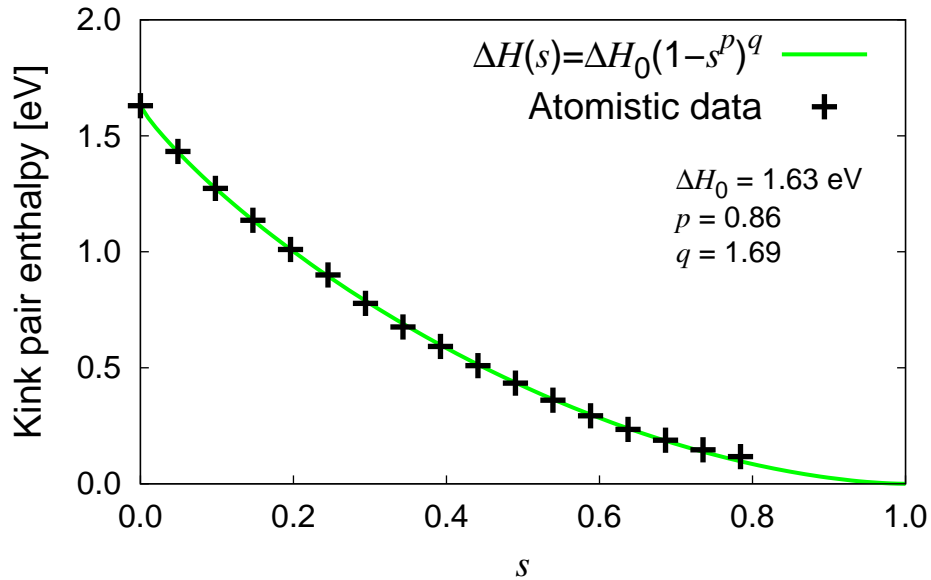


FIGURE 3.9: Kink pair activation enthalpy as a function of stress. The data is fitted to the standard Kocks-Argon-Ashby expression that equals the energy of a pair of isolated kinks at zero stress and vanishes at $s = 1$ ($\tau = \sigma_p$).

the enthalpy of the point of intersection *A* in Fig. 3.7. As we expected, the value of the kink-pair enthalpy tends to zero when the applied stress is close to the Peierls stress.

To obtain the kink-pair enthalpy at 0 MPa the procedure developed by *Ventelon et al.* ([Ventelon et al., 2009](#)) was used, where ‘the formation energy of a single kink is calculated as the difference between the energy of a kinked screw-dislocation and the energy normalized to the same number of atoms of a straight dislocation lying in a single Peierls valley’. The formation enthalpy (equivalent to the energy since there is no mechanical work at 0 MPa) of the kink-pair at 0 MPa is obtained as the sum of the formation enthalpies for the left and right kink. Fig.3.10 shows the convergence of the formation enthalpies with the number of atoms per plane perpendicular to the Burgers vector, obtaining a value of 1.701 eV for the EAM potential. Experimentally, Brunner ([Brunner, 2000](#)) has obtained a value of 1.75 eV from the temperature dependence of flow stress measurements in W, in very good agreement with the calculated value.

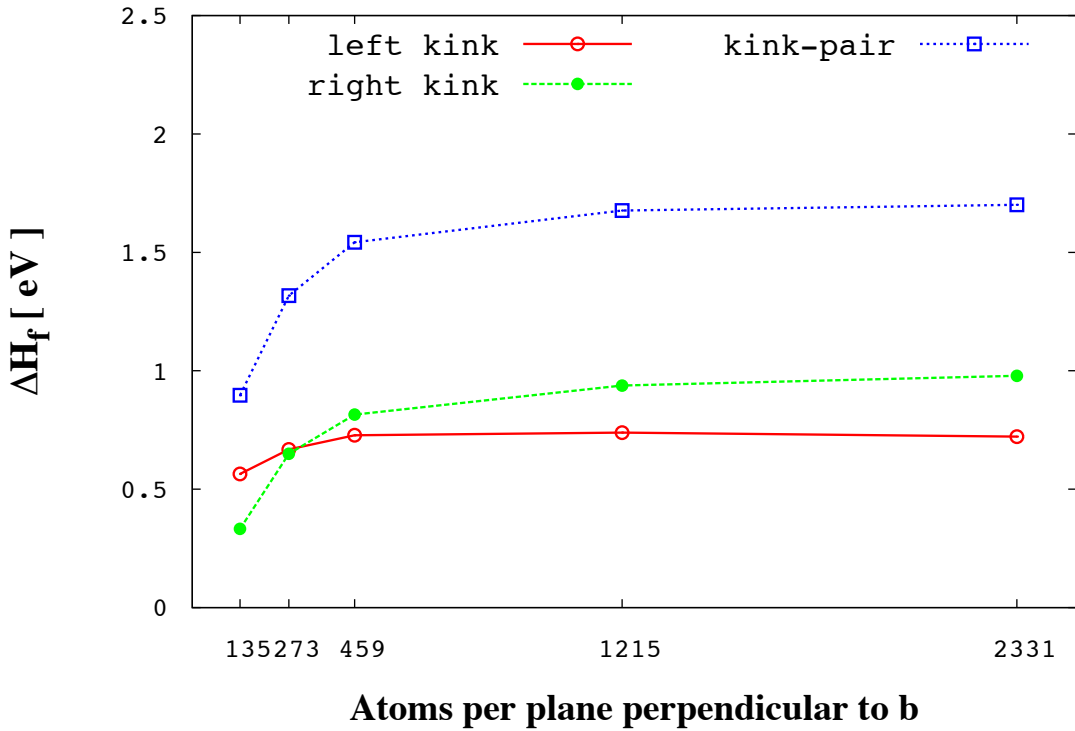


FIGURE 3.10: Kink formation enthalpies as a function of the number of atoms per Burgers vector.

3.3.3 Kink-Pair Width

As it was described in section 3.3.1, the study of the enthalpy barrier in kink-pairs requires that the initial path of the NEB simulation contains a single dislocation for the initial and final replica, while the intermediate replicas (2 ... R-1) contain a kink pair of a specific width. The initial and final replicas maintain their dislocation shape after the NEB simulation. Some of the intermediate replicas achieve the minimum along the path in the form of a dislocation while some others keep the kink pair shape with a different width from the one that was imposed when defining the initial configurations of the intermediate replicas.

The envelope of minimum enthalpy represented in Fig. 3.7 gives an idea of when to expect the change of shape between dislocation and kink pair: intermediate replicas in regions 0-A and B-1 have a dislocation shape, whereas, intermediate replicas in region A-B have a kink pair shape. This can also be probed by visualizing the relaxed replicas via Ovito (Stukowski, 2010). Figure 3.11 shows the results of this visualization, where the atoms defining the dislocation and the kink pair have been highlighted using

the common neighbor analysis (CNA) technique([Faken & Jónsson, 1994](#); [Honeycutt & Andersen, 1987](#); [Tsuzuki et al., 2007](#)).

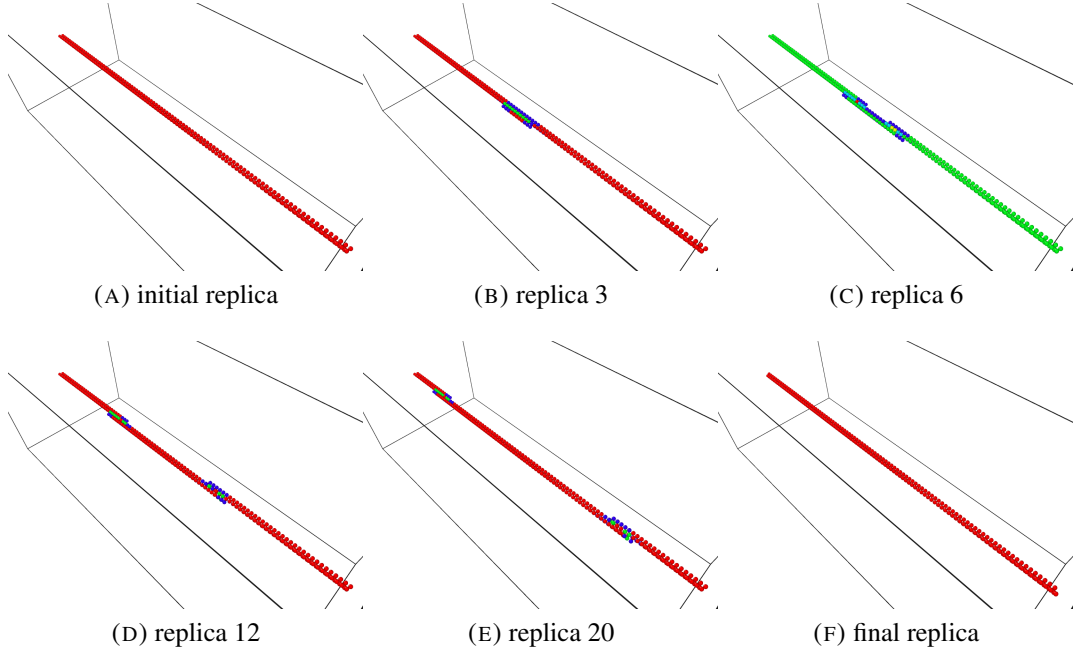


FIGURE 3.11: Atomistic visualization obtained via ovito ([Stukowski, 2010](#)) of different replicas along the final pathway of the NEB simulation at 1200 MPa.

Atomistic visualizations of Fig. 3.11 using the CNA technique present kink pairs with a sharp shape and do not reproduce the details of their profile, required to determine the width. In order to obtain the details on the shape of the replicas, we suggest an analytical methodology that takes into account the coordinates of all the atoms in the simulation box and the displacement field associated with the dislocation.

The steps to obtain the shape of each replica with this analytical method suggested are:

- i. The simulation box is divided into slices along the dislocation line direction x . Each slice has a width of $\mathbf{b}/3$ and contains the atoms of one single plane of the ABC stacking sequence of $\{111\}$ planes in bcc metals.
- ii. For each slice, a grid of nodes that are candidates to host the centroid of the dislocation is created. The grid spacing would determine the efficiency of the method in terms of the precision of the results and the computational cost. The purpose is to identify between all the possible nodes in the grid, the node that is closer to the real position of the centroid of the dislocation.

- iii. Given a perfect bcc lattice oriented with x , y and z axes corresponding to the line, glide and normal directions respectively, inserting a screw dislocation in the box requires that every atom i is displaced according to the following field (?):

$$\begin{aligned} u_x^i &= \frac{b}{2\pi}\theta = \frac{b}{2\pi}\tan^{-1}\left(\frac{R_z^i - c_z}{R_y^i - c_y}\right) \\ u_y^i &= u_z^i = 0 \end{aligned} \quad (3.10)$$

where R_x^i, R_y^i, R_z^i are the coordinates of an atom i in the perfect lattice and c_x, c_y, c_z are the coordinates of the centroid of the dislocation. Applying the previous displacement field to all the atoms in the box guarantees that the centroid of the dislocation is at $C(c_x, c_y, c_z)$.

If we want to obtain the centroid of a dislocation already inserted in a simulation box the previous process needs to be applied in reverse. Denoting r_x^i, r_y^i, r_z^i as the coordinates of an atom i in the distorted configuration with the screw dislocation, the centroid of the dislocation must satisfy the following condition for all the atoms i present in the slice:

$$r_x^i - R_x^i - \frac{b}{2\pi}\tan^{-1}\left(\frac{R_z^i - c_z}{R_y^i - c_y}\right) = 0 \quad (3.11)$$

We then use as a measure error to locate the centroid. The displacement error on atom i when the centroid of the dislocation corresponds to node n is defined as:

$$\epsilon_n^i = r_x^i - R_x^i - \frac{b}{2\pi}\tan^{-1}\left(\frac{R_z^n - R_z^n}{R_y^n - R_y^n}\right), \quad (3.12)$$

where R_x^n, R_y^n, R_z^n are the coordinates of the node n . Node n is considered the centroid of the dislocation for this slice if it minimizes, compared with all the other candidate nodes of the grid, the following sum:

$$\sum_{i=1}^{N_{at}} \epsilon_n^i \quad (3.13)$$

where N_{at} is the number of atoms in this slice.

- iv. We repeat step (iii) for all slices and obtain the kink pair shape shown in Fig. 3.12.

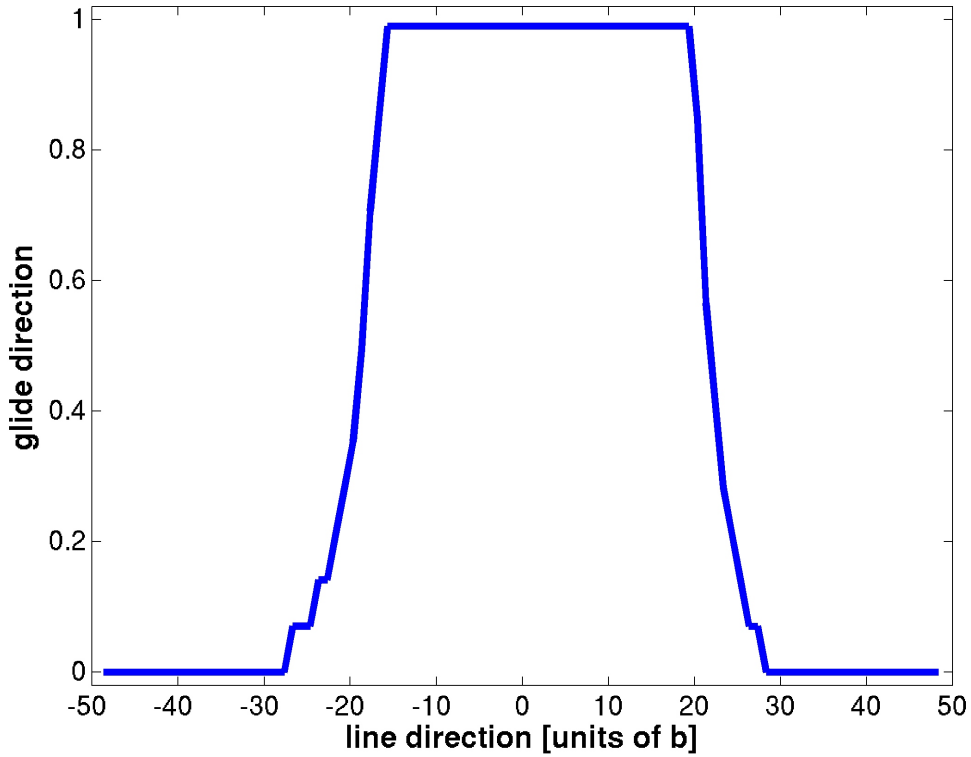


FIGURE 3.12: Shape of kink pair for replica number 14 of the reaction pathway at 1200 MPa.

It is important to consider that the positions of the centroid represented in Fig. 3.12 correspond only to the slices taken three by three, since the stacking sequence of {111} planes in bcc metals has three planes. The comparison between Fig. 3.11 and Fig. 3.12 reveals that the analytic method suggested provides the shape of the dislocation line with more detail than the atomistic visualizations.

Results from Fig. 3.13 shows that the initial and final replicas (1 and 31 respectively) maintain their dislocation shape, some of the intermediate replicas achieve the minimum along the path in the form of a dislocation (replicas number 4,28) and some others keep the kink pair shape (replicas number 5,6,7,14,21).

The enthalpy of the point of intersection A in Fig. 3.7 determines the kink pair enthalpy for each value of applied stress in Fig. 3.9. Therefore, ideally, the width of the kink pair should be computed at the same point A . However, replicas are spread along the reaction pathway in a linear way so it cannot be guaranteed that there is a replica that corresponds exactly with A . Consequently, the kink pair width is going to be computed from the first replica that exhibits a kink pair behavior with a fraction of the dislocation line totally positioned on the next valley.

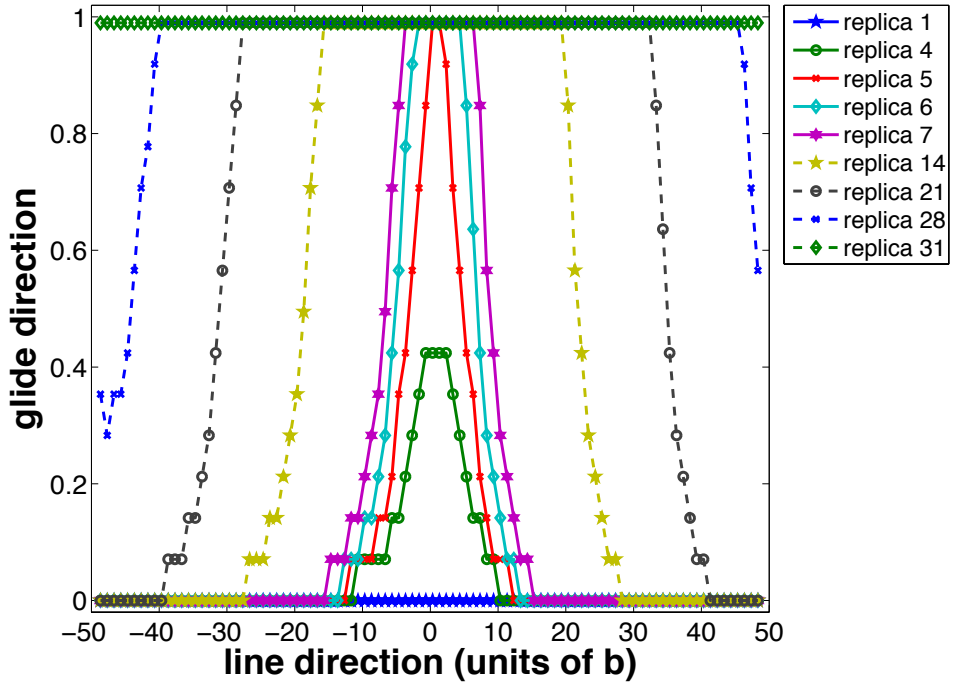


FIGURE 3.13: Shape of several replicas from the final pathway of the NEB simulation when applying 1200 MPa.

Once the replica with the first kink pair behavior is selected, the kink pair width is measured between the inflection points of the two legs of the kink pair. When repeating this process for all the values of applied stress, Fig. 3.14 is obtained.

3.4 Summary

To summarize, the main findings of this chapter can be condensed into the following main items:

- We have performed NEB calculations of single screw dislocations to obtain the energy and enthalpy barriers of straight dislocations and kink-pair configurations as a function of the stress applied.
- Results from Fig. 3.5 show that elementary glide on a $\{1\bar{1}2\}$ plane is a composite of two elementary steps on alternate $\{110\}$ planes. Judging by these results, we conclude that glide on any given plane is achieved by way of sequential $\{110\}$ jumps. This is consistent with previous experimental work from Caillard ([Caillard, 2010a,b](#)).

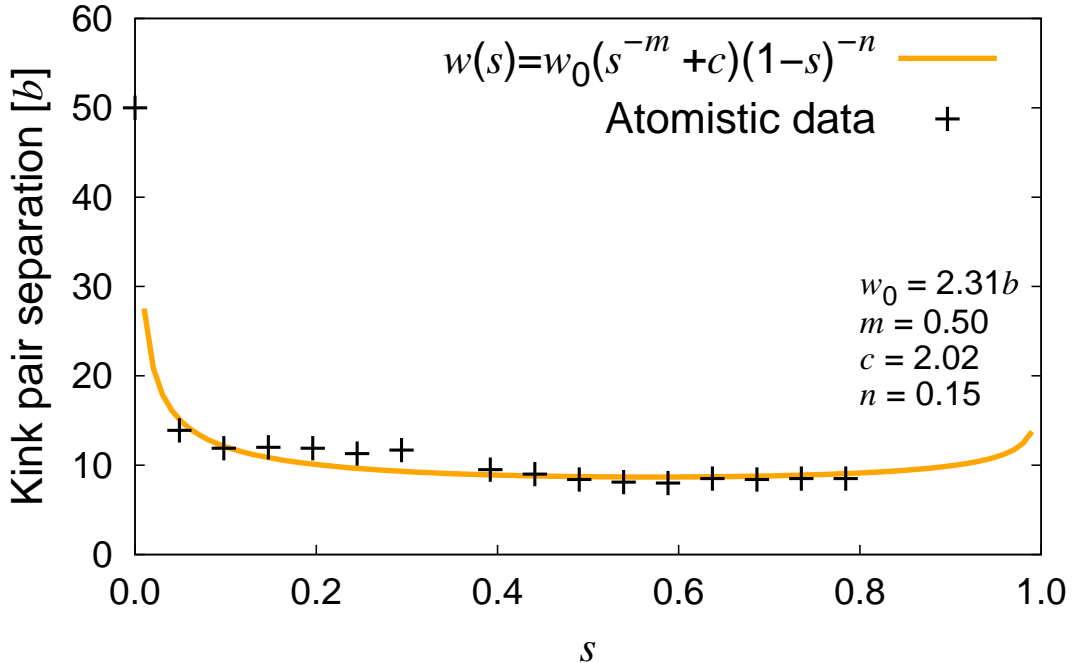


FIGURE 3.14: Kink pair width as a function of the applied stress.

- To study the enthalpy barriers of kink-pairs, intermediate initial replicas are seeded with kink-pair configurations. The activated state, where the enthalpy of the system is measured, is chosen as the maximum energy point along the relaxed final path.
- For each value of stress, the kink-pair width is also measured at the activated state. Fig. 3.14 shows the dependence of the kink-pair width with the stress, with an effective kink pair separation of 11b.

Chapter 4

Atomistic simulations of non-Schmid effects in tungsten

4.1 The Schmid's law

Dislocation slip was presented in Chapter 1 as the most common manifestation of plastic deformation in crystalline solids. If we want to generate slip along the slip plane and the slip direction represented in Fig. 4.1, we can not only consider the tensile stress $\sigma = F/A$, where A is the cross-sectional area perpendicular to F . The characteristic shear stress required for slip depends on the effective area of the slip plane defined by $A/\cos\phi$ and the component of the force in the slip direction $F\cos\lambda$, where ϕ and λ are the angles between the force F and the normal to the slip plane and slip direction, respectively.

Thus, the *resolved shear stress (RSS)* on the slip plane in the slip direction is

$$\tau = \frac{F\cos\lambda}{\frac{A}{\cos\phi}} = \frac{F}{A} \cos\phi \cos\lambda \quad (4.1)$$

where the product $\cos\phi \cos\lambda$ is known as the *Schmid factor*. This factor with maximum value 0.5 is named after Erich Schmid, who introduced the concept in 1935 ([Schmid et al., 1935](#)). According to the above equation, called *Schmid's law*, glide on a given slip system starts when the resolved shear stress on the slip plane in the slip direction reaches a critical value ([Schmid & Boas, 1935](#)). Between all the possible slip systems

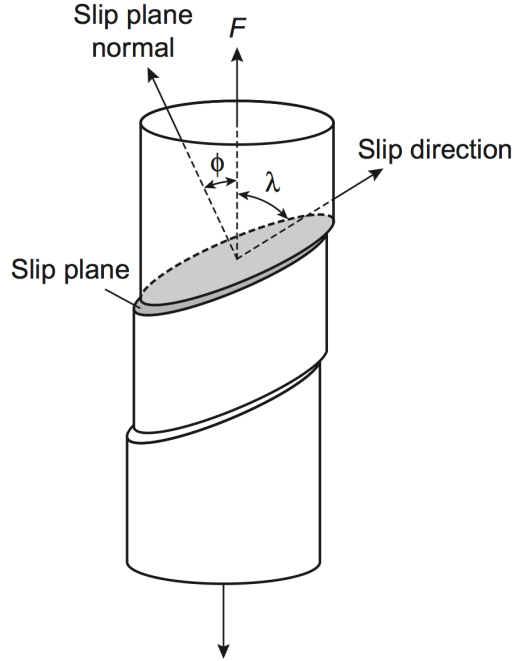


FIGURE 4.1: Geometry of dislocation slip in crystallite materials. In general $(\phi + \lambda) \neq \pi/2$ ([Hull & Bacon, 1984](#)).

α defined by the normal to the slip plane \mathbf{n}^α and the slip direction \mathbf{m}^α , the operational slip system for an applied load in the direction \mathbf{l} is the system that maximizes

$$\cos\phi \cos\lambda = \frac{\mathbf{l} \cdot \mathbf{n}^\alpha}{\|\mathbf{l}\| \cdot \|\mathbf{n}^\alpha\|} \cdot \frac{\mathbf{l} \cdot \mathbf{m}^\alpha}{\|\mathbf{l}\| \cdot \|\mathbf{m}^\alpha\|} \quad (4.2)$$

and the plane of the slip system that maximizes the eq. 4.2 is called *the maximum resolved shear stress plane (MRSSP)*. In the particular case of bcc metals where the most probable slip systems are $[1\ 1\ 1]\{1\ 1\ 0\}$ and $[1\ 1\ 1]\{1\ 1\ 2\}$, the family of the operational slip systems for 231 equally-spaced loading directions along the standard triangle are represented in Fig. 5.3.

If we choose the $(\bar{1}\ 0\ 1)$ plane as a reference, as it is shown in Fig. 4.3, the MRSSP is defined by the angle χ that it makes with the $(\bar{1}\ 0\ 1)$ plane. The dislocation initiates its movement when the shear stress in this MRSSP reaches a critical value called the *critical resolved shear stress (CRSS)*.

In other words, Schmid's law states that the plastic deformation induced by the movement of dislocations is independent of the sense of shearing and other components of the stress tensor σ different from the shear stress on the slip plane in the slip direction. Hence, the resolved shear stress on slip plane α can be expressed as

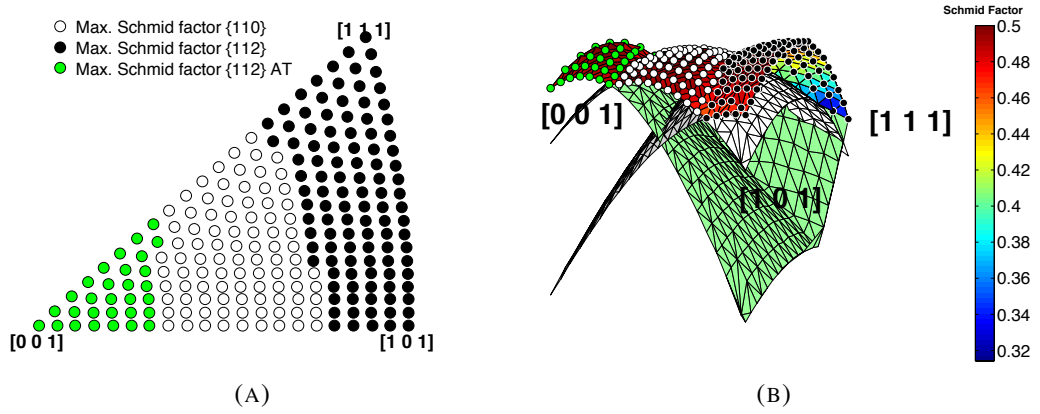


FIGURE 4.2: Schmid factor for 231 equally-spaced loading directions along the standard triangle. 5.3a represents the the slip family with maximum Schmid factor. 5.3b represents the envelope of maximum Schmid factor colored in red.

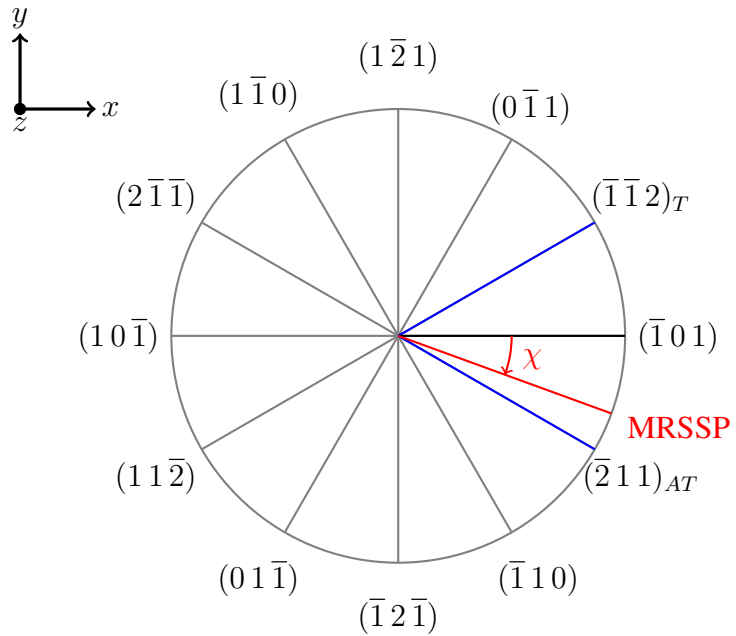


FIGURE 4.3: Schematic view of the glide planes of the [111] axis zone. The orientation of the MRSSP is defined by the angle χ that it makes with the $(\bar{1}01)$ plane. The suffixes ‘T’ and ‘AT’ refer to the twinning and antitwinning senses, respectively.

$$\tau^\alpha = \boldsymbol{\sigma} : \mathbf{m}^\alpha \otimes \mathbf{n}^\alpha \leq \tau_c \quad (4.3)$$

where τ_c is the value of shear stress for which plastic deformation begins. If we choose, for example, the $[1\ 1\ 1](\bar{1}\ 0\ 1)$ slip system, we can write the above yield criterion as

$$\tau^{(\bar{1}\ 0\ 1)} = CRSS \cos\chi = \tau_c, \quad (4.4)$$

which reflects, based on Schmid's law, the symmetrical dependence of the CRSS on the orientation of the MRSSP,

$$CRSS(\chi) = \frac{\tau_c}{\cos\chi} \quad (4.5)$$

4.2 The break down of Schmid's law in bcc crystals

While the Schmid's law is true in metals with face-centered-cubic (fcc) structure, it is known to break down in bcc metals, which has great implications on the overall plastic flow and deformation behavior in these systems.

The first time the particular mechanism of slip of bcc materials was mentioned was in 1928 by Taylor, when he wrote the following: "It is shown also that in β -brass resistance to slipping in one direction on a given plane of slip is not the same as resistance offered to slipping in the opposite direction. Such a difference is to be expected from crystallographic symmetry, but was not observed in α -iron" (Taylor, 1928). But it was not until the 1960s when the failure of the Schmid's law was extensively investigated and documented via experiments (Christian, 1983; Pichl, 2002; Šesták & Zárubová, 1965; Sherwood et al., 1967; Zwiesele & Diehl, 1979).

The non-Schmid behavior of bcc crystals includes two different effects, each of them related to one of the consequences of the Schmid's law: the independency of the CRSS with the sense of slip, and the non-influence of other components of the stress tensor rather than the shear stress on the slip plane in the slip direction. These two effects are discussed in the following subsections.

4.2.1 Twinning/anti-twinning asymmetry

The first of these effects is an intrinsic property of all bcc materials. Following Neumann's principle, which states that "Any kind of symmetry which is possessed by the crystal structure of the material is also possessed by any physical property of the material" (Neumann & Meyer, 1885), the non mirror symmetry of planes belonging to the [1 1 1] zone in bcc crystals (with the exception of {1 1 0} planes where this symmetry is imposed by the ⟨1 1 1⟩ diad axis) first noted by Vitek and co-workers (Duesbery & Vitek, 1998; Ito & Vitek, 2001) implies that positive and negative shear stresses parallel to the dislocation line are not equivalent to each other, meaning that the sign of the applied stress does matter to determine the CRSS. This symmetry - asymmetry of {1 1 0} and {1 1 2} planes in a bcc lattice can be appreciated in Fig.4.4, where the arrangement of atoms in planes with normal [1 1 1] are represented. This characteristic of bcc crystals is commonly referred as the *twinning/anti-twinning asymmetry*.

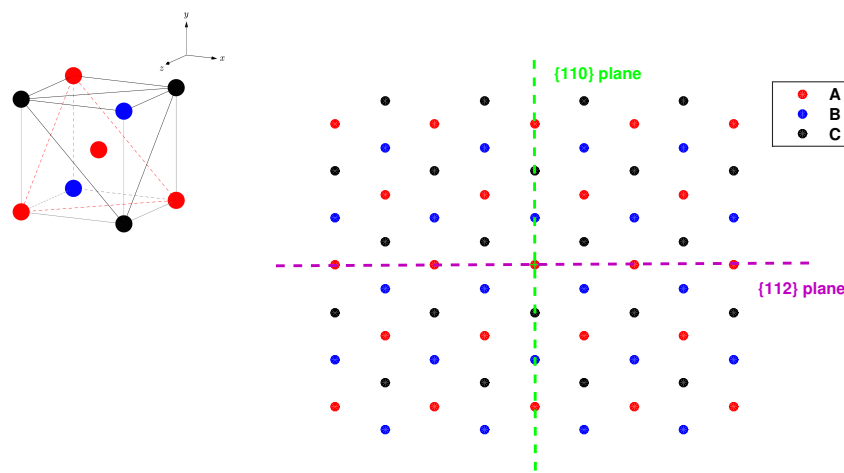


FIGURE 4.4: Arrangement of atoms for a bcc lattice in planes with normal [1 1 1].

With the addition of this twinning/anti-twinning asymmetry, the stress tensor σ applied in a right-handed coordinate system with the y-axis normal to the MRSSP, the z-axis parallel to the slip direction [1 1 1] and the x-axis in the MRSSP is still

$$\sigma = \begin{bmatrix} 0 & 0 & 0 \\ 0 & 0 & \tau \\ 0 & \tau & 0 \end{bmatrix}, \quad (4.6)$$

where τ is the shear stress parallel to the slip direction in the MRSSP, but the yield criterion initially formulated in eq. 4.4 includes now an additional term,

$$\tau^\alpha = \boldsymbol{\sigma} : \mathbf{m}^\alpha \otimes \mathbf{n}^\alpha + a_1 \boldsymbol{\sigma} : \mathbf{m}^\alpha \otimes \mathbf{n}_1^\alpha \leq \tau_c \quad (4.7)$$

where a_1 is an adjustable parameter and \mathbf{n}_1 is, following the sign criterion used by Vitek and co-workers ([Gröger et al., 2008a,b](#)), the unit vector perpendicular to the $\{1\bar{1}0\}$ plane in the zone of \mathbf{m}^α that makes the angle -60° with the reference plane. For the $[1\bar{1}1](\bar{1}01)$ slip system, in a similar way to the formulation of eq. 4.4, we can write the above yield criterion as

$$\tau^{(\bar{1}01)} + a_1 \tau^{(0\bar{1}1)} = \tau_c \quad (4.8)$$

$$CRSS \cos\chi + a_1 CRSS \cos(\chi + \pi/3) = \tau_c \quad (4.9)$$

and then the CRSS is not symmetric anymore with respect to the orientation of the MRSSP,

$$CRSS(\chi) = \frac{\tau_c}{\cos\chi + a_1 \cos(\chi + \pi/3)} \quad (4.10)$$

where τ_c can be also expressed as a function the Peierls stress τ_p and a fitting parameter a_0 , i.e. $\tau_c = a_0 \tau_p$. In this case the CRSS depends now on the orientation of the MRSSP, the Peierls stress, and the fitting parameters a_0 and a_1 as follows

$$CRSS(\chi) = \frac{a_0 \tau_p}{\cos\chi + a_1 \cos(\chi + \pi/3)} \quad (4.11)$$

Atomistic simulations

Based on the detailed analysis of several W interatomic potentials from Chapter 2, we have used the embedded-atom method (EAM) interatomic potential parameterized by Marinica et al. ([Marinica et al., 2013](#)), the most suitable potential (between the five potentials studied) in terms of screw dislocation property calculations and computational

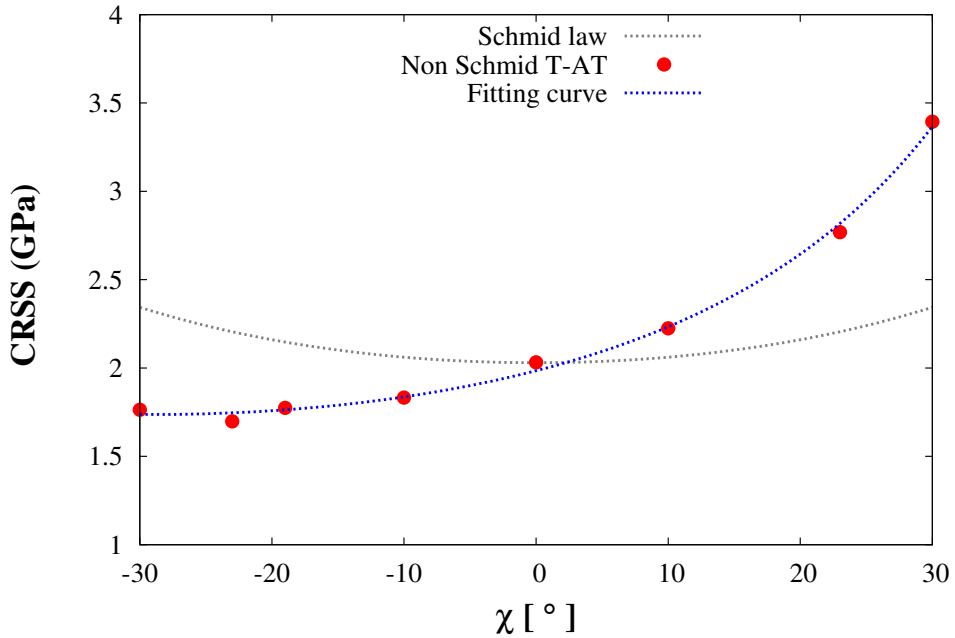


FIGURE 4.5: Dependence of the CRSS on the orientation of the MRSSP, i.e. angle χ , when applying shear stress parallel to the slip direction in the MRSSP.

efficiency. This potential predicts the correct symmetric core structure at 0 K and a Peierls stress of 2.03 GPa.

We use the standard geometry of the $[1\bar{1}1]$ zone as shown in Fig.4.3 to compute the CRSS using atomistic simulations. This is done by performing nudged-elastic band (NEB) calculations of single screw dislocations with a setup essentially identical to that used in Chapter 3. The distance between the initial and final replica is the distance between two consecutive Peierls Valleys and therefore it depends on the orientation of the MRSSP. The size of the simulation box also depends on the orientation of the MRSSP. For example, when $\chi = 0$ the size of the simulation box is $21 \times 24 \times 1$ multiples of the bcc lattice vectors $[\bar{1}21] \times [\bar{1}01] \times [111]$ containing nominally 3024 atoms.

The dependence of the CRSS with χ for the EAM potential employed here and its deviation from Schmid's law are shown in Fig.4.5. For $\chi > 0$, the CRSS is always higher than the corresponding value for $\chi < 0$. Then, we can conclude that $\chi > 0$ is identified as shear in the antitwinning sense and $\chi > 0$ is identified as shear in the twinning sense. Considering the crystal symmetry, only the angular interval $-\frac{\pi}{6} \leq \chi \leq \frac{\pi}{6}$ need to be explored. A least-squares fit of the atomistic data with eq. 4.10 is also represented in the figure. The values of the fitting parameters are $a_0 = 1.437$ and $a_1 = 0.938$.

4.2.2 Non glide stresses

The second of the non-Schmid effects is related to the importance of non glide stresses in the deformation process, and it is not an intrinsic property of bcc crystals. In fact, it was first noted by Escaig (Escaig, 1968, 1974) when studying cross-slip in fcc materials. Studies using accurate atomistic methods (semi empirical interatomic potentials and density functional theory calculations) have shown that stress components that are not collinear with the Burgers vector do not move the dislocation, but change the dislocation core configuration modifying the process of slip (Chaussidon et al., 2006; Gröger et al., 2008a,b; Gröger & Vitek, 2005; Woodward & Rao, 2001).

Adding these non glide stresses to the existing twinning/antitwinning asymmetry result into a new applied stress tensor σ ,

$$\sigma = \begin{bmatrix} -\sigma & 0 & 0 \\ 0 & \sigma & \tau \\ 0 & \tau & 0 \end{bmatrix}, \quad (4.12)$$

where σ is the non glide stress perpendicular to the slip direction in the MRSSP, and the yield criterion formulated in eq. 4.7 includes now two additional terms that represent the contribution of the non glide effects,

$$\begin{aligned} \tau^\alpha &= \sigma : \mathbf{m}^\alpha \otimes \mathbf{n}^\alpha + a_1 \sigma : \mathbf{m}^\alpha \otimes \mathbf{n}_1^\alpha + \\ &a_2 \sigma : (\mathbf{n}^\alpha \times \mathbf{m}^\alpha) \otimes \mathbf{n}^\alpha + a_3 \sigma : (\mathbf{n}_1^\alpha \times \mathbf{m}^\alpha) \otimes \mathbf{n}_1^\alpha \leq \tau_c \end{aligned} \quad (4.13)$$

where a_2 and a_3 are adjustable parameters. The first two terms in eq. 4.13 are contributions to the RSS parallel to the dislocation line and the last two terms are contributions perpendicular to the dislocation line. The application of the above yield criterion to the [1 1 1]($\bar{1}$ 0 1) slip system results in

$$\tau^{(\bar{1} 0 1)} + a_1 \tau^{(0 \bar{1} 1)} + a_2 \sigma^{(\bar{1} 0 1)} + a_3 \sigma^{(0 \bar{1} 1)} = \tau_c \quad (4.14)$$

$$CRSS \cos\chi + a_1 CRSS \cos(\chi + \pi/3) + \sigma[a_2 \sin 2\chi + a_3 \cos(2\chi + \pi/6)] = \tau_c \quad (4.15)$$

Hence, when all the contributions of the non-Schmid effects are considered, the CRSS depends on the orientation of the MRSSP as

$$CRSS(\chi) = \frac{a_0\tau_p - \sigma[a_2\sin 2\chi + a_3\cos(2\chi + \pi/6)]}{\cos \chi + a_1\cos(\chi + \pi/3)} \quad (4.16)$$

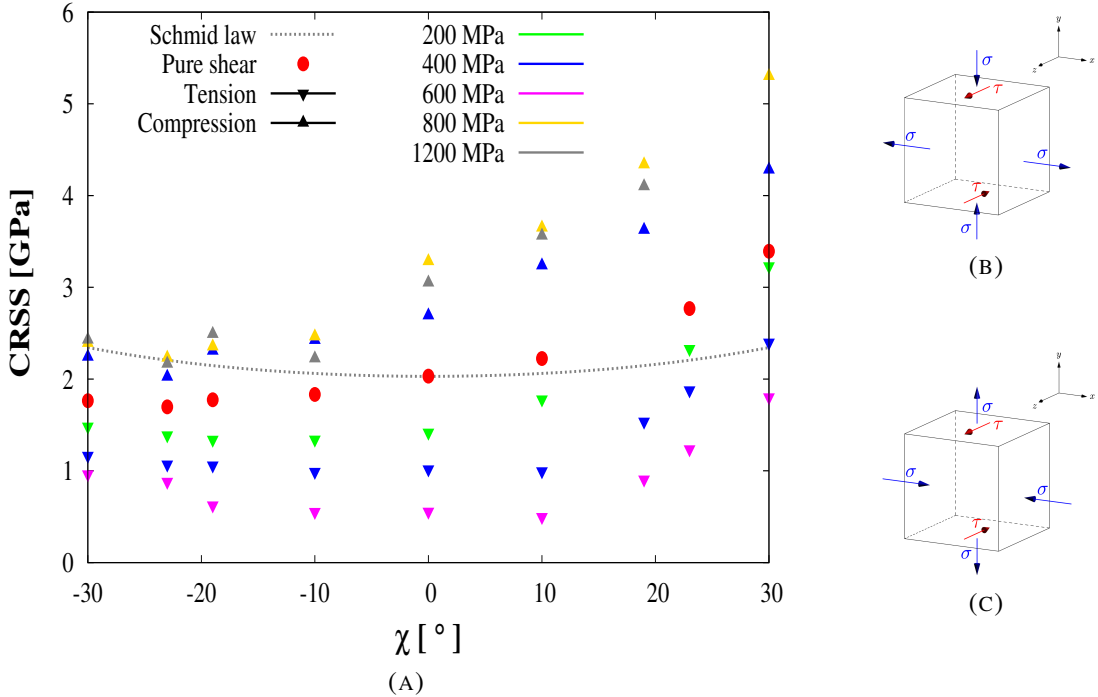


FIGURE 4.6: (a) Dependence of the CRSS on the orientation of the MRSSP, i.e. angle χ , when applying pure shear stress τ (circles) and a combination of shear stress and non glide stresses σ in tension (down-triangles) and compression (up-triangles). (b) Compression loading scheme. (c) Tension loading scheme.

Atomistic calculations

New forces need to be applied in two different directions to include the effect of non glide stresses in the atomistic simulations. First, an external force f_x is added to the atoms in the boundary surfaces of the simulation box perpendicular to the x axis. The external force per atom satisfies $f_x = \frac{\sigma L_y L_z}{N_x}$, where σ is the applied non glide stress, N_x is the number of atoms in each surface and $L_y \times L_z$ is the area of the each of the boundaries surfaces perpendicular to x . Second, an external force f_y is added to the atoms in the surfaces perpendicular to the y axis, where the shear stress τ was already applied. In a similar way to f_x , $f_y = \frac{\sigma L_x L_z}{N_y}$, where σ is the applied non glide stress, N_y is the number of atoms in each surface and $L_x \times L_z$ is the area of the each of the

surfaces perpendicular to z . Atomistic calculations specifically designed to calculate the non-Schmid critical stress τ_c^χ as a function of the angle χ between the maximum resolved shear stress (MRSS) plane were performed according to the geometry shown schematically in Figure 4.7. The Figure shows the mapping between the atomistic box and the crystallography of the [111] zone. Following the sign convention used in the Figure, NEB calculations are performed between the two relaxed configurations with the previous setup.

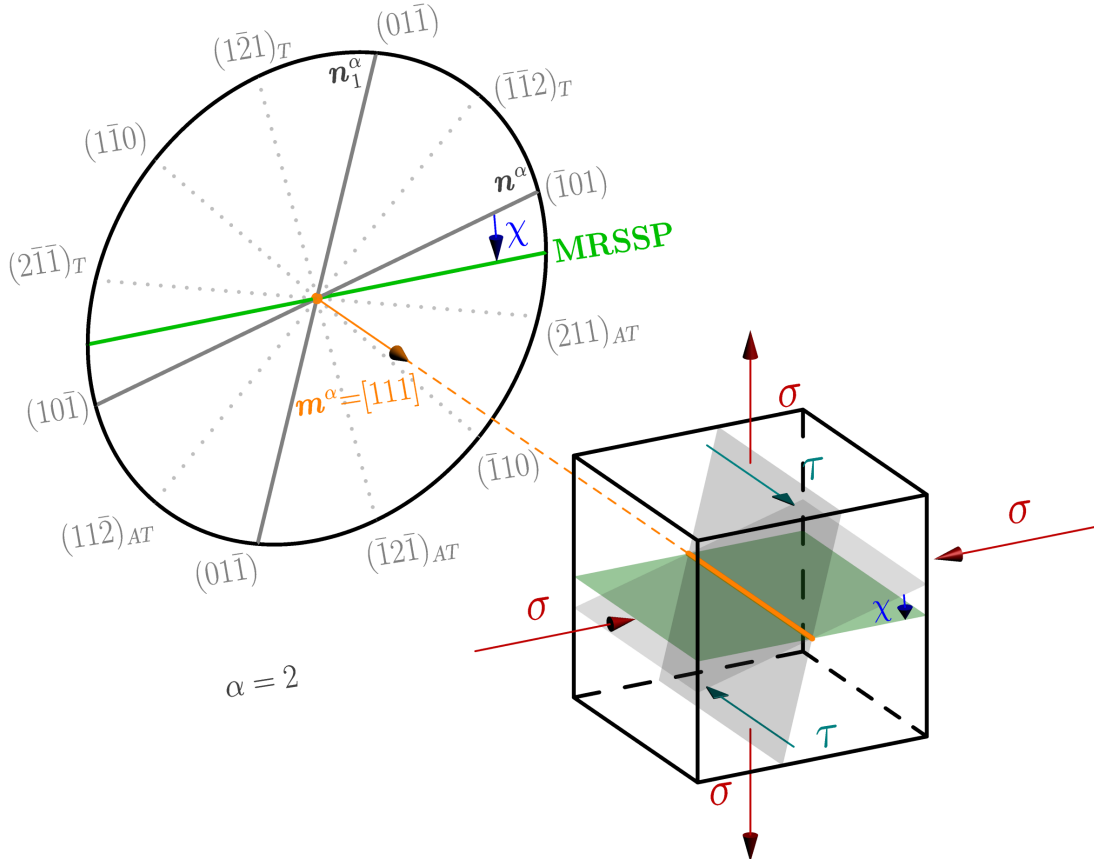


FIGURE 4.7: Crystallographic diagram of the [111] zone in the bcc lattice with each $\{110\}$ and $\{112\}$ clearly labeled. The picture also shows a mapping of the [111] zone to a schematic atomistic box containing a screw dislocation subjected to shear and nonglide stresses according to Vitek's convention. The glide n^α , auxiliary n_1^α and MRSSP planes are labeled in each case. A $[\bar{1}01]$ glide plane corresponds to $\alpha = 2$ in our CP calculations.

The dependence of the CRSS on the orientation of the MRSSP and the magnitude of the non glide stress are shown in Fig.4.6. It is seen from this figure that for a given χ , applying non glide stresses in tension and compression clearly deviates the CRSS from the pure shear stress scenario. These results justify the interest to include the effect of non glide components of the stress tensor during the process of dislocation slip.

When Groger and Vitek ([Gröger et al., 2008a,b](#)) first computed these effects using atomistic simulations, they suggested to keep the values of a_0 and a_1 fixed from the least-squares fit of eq. 4.11, which represents only pure shear stress, and then determine the parameters a_2 and a_3 using also a least-square method, but taking only into account the linear part of the dependence of CRSS with the non glide stress σ for three orientations of the MRSSP. For the interatomic potential used in our simulations, the least-squares fit of the linear part at $\chi = 0$ and $\chi = \pm 10$ leads to the following values of the fitting parameters: $a_2 = 0.71$ and $a_3 = 4.43$.

4.2.3 Projection tensor and non-Schmid effects

The influence of non-Schmid effects are also studied by evaluating the stress projection factor P_{tot} for each crystallographic loading orientation in the standard triangle. As previously defined ([Lim et al., 2013; Weinberger et al., 2012](#)), the stress projection factor for a crystallographic loading direction \mathbf{l} on a slip system α is

$$P_{tot}^\alpha = \mathbf{l} \cdot \mathbf{P}^\alpha \cdot \mathbf{l} \quad (4.17)$$

and the stress projection factor P_{tot} for each crystallographic loading orientation in the standard triangle is the maximum of P_{tot}^α for all the slip systems α considered active during slip. The number of terms defining \mathbf{P}^α depends on whether or not non-Schmid effects are included in the model. If only the Schmid's law is considered, then

$$\mathbf{P}^\alpha = \mathbf{m}^\alpha \otimes \mathbf{n}^\alpha \quad (4.18)$$

If the T/AT asymmetry is considered, then \mathbf{P}^α is

$$\mathbf{P}^\alpha = \mathbf{m}^\alpha \otimes \mathbf{n}^\alpha + a_1 \mathbf{m}^\alpha \otimes \mathbf{n}_1^\alpha \quad (4.19)$$

Finally, if both non-Schmid effects, the T/AT asymmetry and non-glide stresses, are included in the model, then \mathbf{P}^α is defined as

$$\mathbf{P}^\alpha = \mathbf{m}^\alpha \otimes \mathbf{n}^\alpha + a_1 \mathbf{m}^\alpha \otimes \mathbf{n}_1^\alpha + a_2 (\mathbf{n}^\alpha \times \mathbf{m}^\alpha) \otimes \mathbf{n}^\alpha + a_3 (\mathbf{n}_1^\alpha \times \mathbf{m}^\alpha) \otimes \mathbf{n}_1^\alpha \quad (4.20)$$

Fig. 4.8 shows the contributions of the non-Schmid effects on P_{tot} for 231 uniformly-distributed crystallographic loading orientations in the standard triangle when $\langle 111 \rangle\{110\}$ slip systems are active. The dependence of the projection factor on the orientation of the loading axis increases when non-Schmid effects are considered. Moreover, if pure Schmid behavior is considered (eq. 4.18), the maximum value of P_{tot} is 0.5, if only the T/AT asymmetry is considered (eq. 4.19) the maximum value of P_{tot} is 0.8, and if both T/AT asymmetry and non-glide stresses are considered (eq. 4.20) the maximum value of P_{tot} is 2.3.

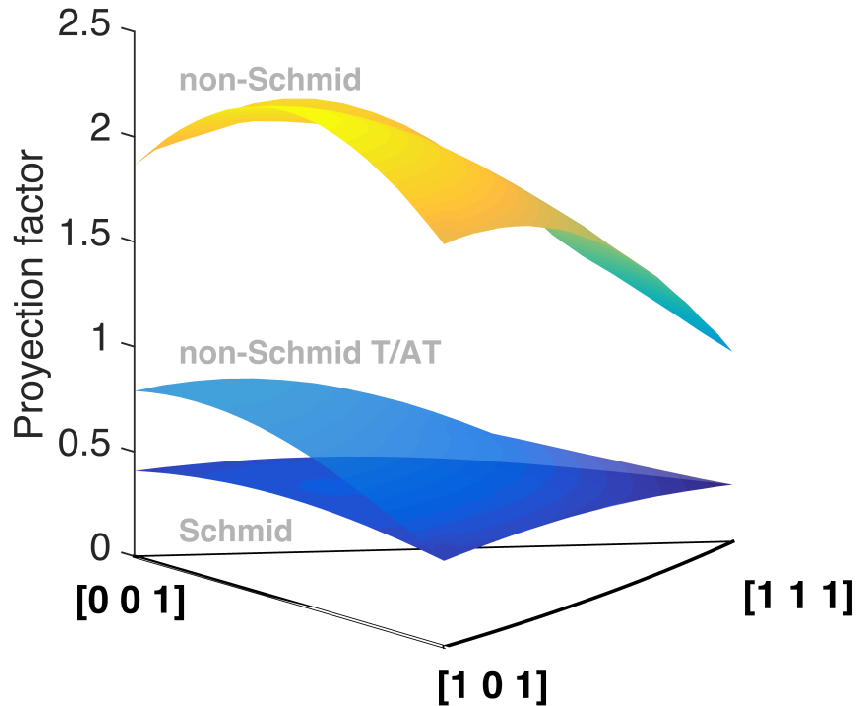


FIGURE 4.8: Stress proyection factor P_{tot} for 231 uniformly-distributed crystallographic loading orientations in the standard triangle when $\langle 111 \rangle\{110\}$ slip systems are active. Three different scenarios are studied: (i) Schmid law, (ii) non-Schmid effects including only T/AT asymmetry, (iii) non-Schmid effects including both T/AT asymmetry and non glide stresses.

4.3 Parabolic and multiparametric implementation of the non-Schmid effects

In this section we present two novel approaches to include the contribution of the non-Schmid effects in the formulation of the RSS.

Our first approach focus on the non glide stresses, and in particular, the mathematical shape of the function where the parameters are fitted. Instead of taking only the linear part into account, as it was proposed in the previous section, we suggest to consider the dependence of CRSS with σ for the entire range of non glide stress, from tension to compression. The dependence of the CRSS with χ presented in Fig. 4.6a is now represented as CRSS versus the non glide stress σ in Fig.4.9. Trying different functions we have found that a parabolic dependence of the CRSS with the non glide stress is a good approximation. When considering this parabolic dependence, the yield criterion from eq. 4.13 is reformulated as

$$\begin{aligned} \tau^\alpha = & \boldsymbol{\sigma} : \mathbf{m}^\alpha \otimes \mathbf{n}^\alpha + a_1 \boldsymbol{\sigma} : \mathbf{m}^\alpha \otimes \mathbf{n}_1^\alpha + [a_2 \boldsymbol{\sigma} \circ \boldsymbol{\sigma} + a_3 \boldsymbol{\sigma} + a_4 \mathbf{I}] : (\mathbf{n}^\alpha \times \mathbf{m}^\alpha) \otimes \mathbf{n}^\alpha + \\ & [a_5 \boldsymbol{\sigma} \circ \boldsymbol{\sigma} + a_6 \boldsymbol{\sigma} + a_7 \mathbf{I}] : (\mathbf{n}_1^\alpha \times \mathbf{m}^\alpha) \otimes \mathbf{n}_1^\alpha \leq \tau_c \end{aligned} \quad (4.21)$$

where $a_2 \dots a_7$ are fitting parameters, \mathbf{I} is the identity tensor and $\boldsymbol{\sigma} \circ \boldsymbol{\sigma}$ is the Hadamard product¹ of the stress tensor $\boldsymbol{\sigma}$. The dependence of CRSS with the orientation of the MRSSP and the non glide stress σ from eq.4.15 is now

$$CRSS(\chi, \sigma) = \frac{a_0 \tau_p - [(a_2 \sigma^2 + a_3 \sigma + a_4) \sin(2\chi) + (a_5 \sigma^2 + a_6 \sigma + a_7) \cos(2\chi + \pi/6)]}{\cos(\chi) + a_1 \cos(\chi + \pi/3)} \quad (4.22)$$

Keeping the values of a_0 and a_1 fixed from the least-squares fit of eq.4.11, a least-squares fit of eq.4.22 with the atomistic data from Fig.4.9 gives the following values of the fitting parameters: $a_2 = 0.902$, $a_3 = 2.295$, $a_4 = -0.196$, $a_5 = 1.805$, $a_6 = 3.771$ and $a_7 = -0.101$.

¹ $(A \circ B)_{i,j} = A_{i,j} \cdot B_{i,j}$

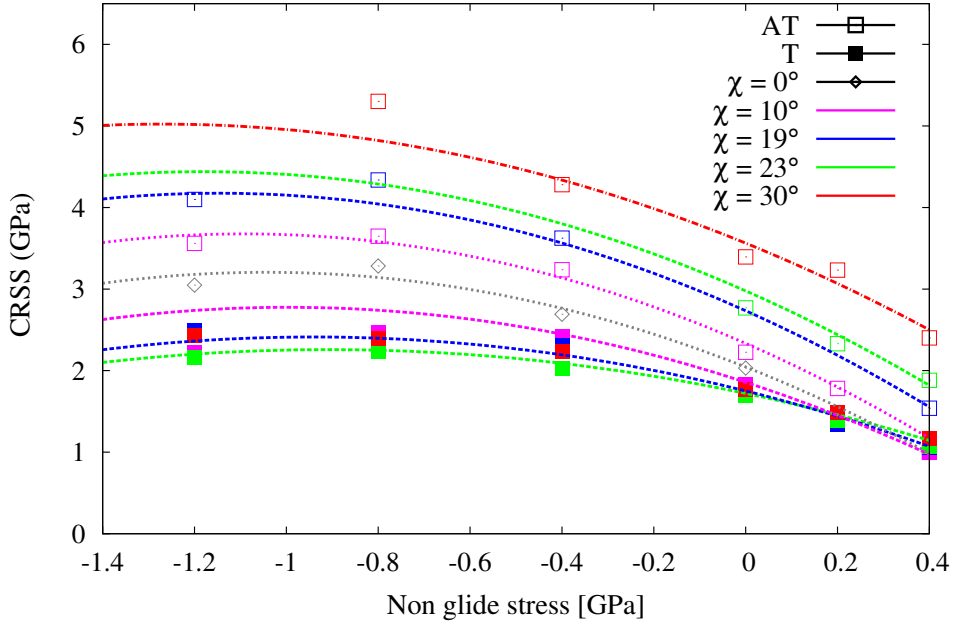


FIGURE 4.9: Dependence of the CRSS on the non glide stress perpendicular to the slip direction. In agreement with Fig.4.6, positive and negative values are assigned to compression and tension loading, respectively. The CRSS is also plotted at different orientations of the MRSSP, i.e. angle χ , in the twinning (T) and antitwinning (AT) regions.

Our second approach combines both non-Schmid effects, twinning-antitwinning asymmetry and non glide stresses. It has been seen in previous sections that the CRSS depends on both the orientation of the MRSSP given by χ and the magnitude and sign of the non glide stress σ applied. Instead of capturing these two effects sequentially and constraining the dependence by imposing the shape of the mathematical functions, we suggest a general fit that captures both dependencies of χ and σ simultaneously and with no constraints in the shape of the mathematical function. By performing a general fit of the atomistic data represented in Fig. 4.6a we obtain the following expression of CRSS

$$CRSS(\chi, \sigma) = 1.797 + 0.021 \cdot \chi + 9.175 \cdot 10^{-4} \cdot \chi^2 + 1.087 \cdot 10^{-5} \cdot \chi^3 - 1.796 \cdot \sigma - 0.028 \cdot \sigma \chi - 0.552 \cdot \sigma^2 \quad (4.23)$$

which defines the CRSS as a surface that depends on two variables, χ and σ . The atomistic data and the CRSS surface is shown in Fig.4.10.

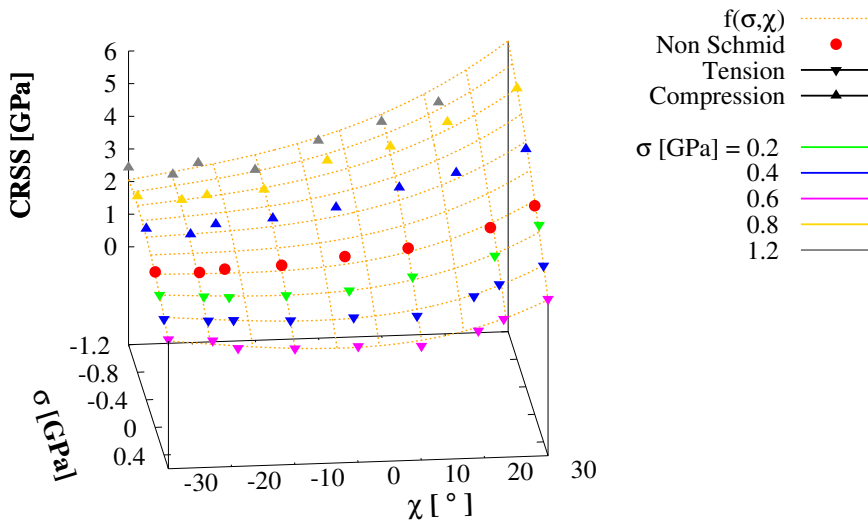


FIGURE 4.10: Surface plot that captures the simultaneous dependence of the CRSS on both the orientation of the MRSSP, i.e. angle χ , and the non glide stress σ . The surface defined by eq. 4.23 is also plotted.

4.4 Summary

To summarize, the main findings of this chapter can be condensed into the following main items:

- NEB simulations have been performed in single crystal tungsten to capture the characteristic non-Schmid behavior of bcc metals during dislocation slip. The EAM interatomic potential from Marinica et al.([Marinica et al., 2013](#)) has been used in all the calculations.
- The results obtained reveal the importance of both non-Schmid effects. Contrary to Schmid's law, the CRSS in tungsten for this interatomic potential depends on the twinning-antintwinning asymmetry and the non glide stresses.
- In addition to the standard procedure to capture the non-Schmid effects suggested by Vitek and co-workers ([Gröger et al., 2008a,b](#)), we present two additional approaches. First, we compute the contribution of the non-glide stresses using a parabolic dependence of CRSS with the non glide stress σ . Second, we suggest a multiparametric fitting surface with no contrains that captures the dependence of CRSS with χ and σ simultaneously.

Part II

CRYSTAL PLASTICITY SIMULATIONS

Chapter 5

Linking atomistic, kinetic Monte Carlo and crystal plasticity simulations of single-crystal tungsten strength

5.1 Introduction

Tungsten and tungsten alloys are being considered as leading candidates for structural and functional materials in future fusion energy devices. The most attractive properties of tungsten for the design of magnetic fusion energy reactors are its high melting point and thermal conductivity, low sputtering yield and low long-term disposal radioactive footprint. However, tungsten also presents a very low fracture toughness, mostly associated with inter-granular failure and bulk plasticity, that limits its applications ([Bolt et al., 2004](#); [Rieth et al., 2013a](#); [Zinkle & Ghoniem, 2011](#)).

The plastic behavior of bcc refractory metals like tungsten is governed by the kink-pair mediated thermally activated motion of $\frac{1}{2} \langle 111 \rangle$ screw dislocations ([Cai et al., 2004a](#); [Ismail-Beigi & Arias, 2000](#); [Vitek, 2004a](#); [Vitek et al., 1970](#)). Dislocation slip in bcc metals has been reported in the literature on $\{110\}$, $\{112\}$ and $\{123\}$ slip planes. While some authors have suggested that the temperature range determines the activation of slip planes ($\{110\}$ and $\{112\}$ planes at lower temperatures, $\{123\}$ planes at higher temperatures) ([Ma et al., 2007](#); [Raabe, 1995a](#); [Sestak & Seeger, 1978](#)) , other works propose the decomposition of slip into $\{112\}$ and $\{123\}$ planes on alternating $\{110\}$ planes, suggesting that slip occurs entirely on $\{110\}$ slip planes at room

temperature (Brunner, 2010; Christian, 1983; Madec & Kubin, 2004; Spitzig & Keh, 1970; Van Petegem et al., 2013). Schmid's law, which is used to determine the active slip planes for a specific stress state (Schmid & Boas, 1950) is known to break down for bcc metals. This particularity with a big impact on the plastic flow is referred to as *non-Schmid behavior*, and it implies that the critical resolved shear stress defining the onset of dislocation glide on a given slip plane varies with the sign of the applied stress and the orientation of the loading axis with respect to the lattice (Duesbery & Vitek, 1998; Qin & Bassani, 1992).

A whole variety of crystal plasticity (CP) constitutive models have been proposed and discussed in the literature to solve multiple plasticity problems in materials. There are two main groups of constitutive models differentiated by the nature of the state variable they use: phenomenological models mostly use a critical resolved shear stress as state variable for each slip system (Hutchinson, 1976; Peirce et al., 1982, 1983; Rice, 1971), while physically-based constitutive models rely on the dislocation density as state variable since dislocations are considered the main carriers of plasticity (Arsenlis & Parks, 2002; Arsenlis et al., 2004; Ma et al., 2006). Most of the existing CP frameworks have been focused on fcc metals (Alankar et al., 2012; Arsenlis & Parks, 1999; Cheong & Busso, 2004; Ma & Roters, 2004), while only a few studies have been devoted to study bcc plasticity. The selection of active slip systems in the constitutive framework will also affect the predictions of the model. The incorporation of non-Schmid effects can be used as a differentiating feature among the models for bcc materials. Table 5.1 presents the most important examples of CP models for bcc metals classified by the previous criteria.

In this work, we present a CP framework to obtain the yield strength in single crystal tungsten. The constitutive model is built on physically-based mobility functions¹ for $\frac{1}{2}\langle 111 \rangle$ screw dislocations obtained via kMC simulations, which include the characteristic *non-Schmid* behavior of bcc metals. Another important aspect in our simulations is the consideration of the entire family of $\{110\}\langle 111 \rangle$ and $\{112\}\langle 111 \rangle$ slip systems (twelve each) and combinations thereof. We simulate uniaxial tensile tests along 231 different crystallographic orientations in the standard triangle. The temperature range covered goes from room temperature to $\frac{1}{3}T_m$, where $T_m=3680$ K is the melting point for tungsten (Lassner & Schubert, 1999). The orientation dependence of the stress-strain curves and the temperature dependence of the yield stress predicted by our model are in

¹The mobility function represents the relation between the dislocation velocity and the state variables stress and temperature.

TABLE 5.1: CP constitutive models for bcc metals.

	Phenomenological			Physically-based			
<i>slip planes</i>	{110}	{110} {112}	{110} {112} {123}	{110}	{112}	{110} {112}	{110}
Schmid	-	(Raphael & Van Houtte, 1985) (Erieau & Rey, 2004)	(Hölscher et al., 1991, 1994) (Raabe, 1995a,b; Raabe et al., 1994)	(Peeters et al., 2000) (Stainier et al., 2002)	-	(Kitayama et al., 2013)	(Ma et al., 2007) (Hamelin et al., 2011)
Non Schmid	(Weinberger et al., 2012)	(Lee et al., 1999) (Lim et al., 2013) (Kuchnicki et al., 2008)	-	(Koester et al., 2012) (Narayanan et al., 2014a) (Patra et al., 2014)	(Yalcinkaya et al., 2008)	(Alankar et al., 2014)	-

qualitative agreement with previous results in other bcc metals (Brunner & Diehl, 1991; Kuramoto et al., 1979; Narayanan et al., 2014a).

The paper is organized as follows. The formulation of the constitutive model proposed is described in Section 5.2. Simulation details and the predictor-corrector scheme are presented in Section 5.3. In Section 5.4 we report the CP calculations in single crystal tungsten as a function of the Schmid behavior, glide plane, loading direction and temperature. Final concluding remarks are given in Section 5.5.

5.2 Constitutive model

We use the multiplicative decomposition of the deformation gradient \mathbf{F} :

$$\mathbf{F} = \mathbf{F}_e \mathbf{F}_p \quad (5.1)$$

where \mathbf{F}_e and \mathbf{F}_p are the elastic and plastic deformation gradients, respectively (Reina & Conti, 2014). The plastic deformation evolves as:

$$\dot{\mathbf{F}}_p = \mathbf{L}_p \mathbf{F}_p \quad (5.2)$$

where \mathbf{L}_p is the deformation velocity gradient. In the case of dislocation slip as the only deformation process (no mechanical twinning or martensitic transformations considered), \mathbf{L}_p can be formulated as:

$$\mathbf{L}_p = \sum_{\alpha} \dot{\gamma}^{\alpha} \mathbf{M}^{\alpha} = \sum_{\alpha} \dot{\gamma}^{\alpha} \mathbf{m}^{\alpha} \otimes \mathbf{n}^{\alpha} \quad (5.3)$$

Here, the running index α goes from 1 to n , where n is the total number of slip systems; \mathbf{m}^{α} and \mathbf{n}^{α} are unit vectors representing the normalized slip direction and the normal to the slip plane of the system α , respectively; $\dot{\gamma}^{\alpha}$ is the shear rate on system α , given by the Orowan equation:

$$\dot{\gamma}^{\alpha} = \rho^{\alpha} b v^{\alpha} \quad (5.4)$$

where b is the magnitude of the Burgers vector, ρ^{α} is the density of mobile dislocations and v^{α} is the dislocation velocity on slip system α .

5.2.1 Dislocation velocity function

In bcc metals such as tungsten, screw dislocations with Burgers vector $\mathbf{b} = \frac{1}{2} [111]$ are the main net carriers of the plastic shear due to their low mobility and non-planar core structure ([Hartmaier & Gumbsch, 2005a](#); [Vitek, 2004a](#); [W. Cai & Yip, 2002](#)). At low temperatures, screw motion proceeds via thermally activated kink pair nucleation and lateral propagation. These effects render screw dislocation motion the rate limiting kinematic mechanism and thus in our model we only focus on it. Molecular Dynamics (MD) is a commonly used simulation technique to capture dislocation mobility functions ([Cereceda et al., 2013](#); [Gilbert et al., 2011](#); [Olmsted et al., 2005](#)). In bcc crystals, MD simulations naturally include non Schmid effects as part of the simulated dynamics of screw dislocation motion, but they provide overdriven dynamics and are limited to glide on $\{112\}$ planes due to limitations with boundary conditions and the interatomic potentials used ([Cereceda et al., 2013](#); [Gilbert et al., 2011](#)). An alternative technique that is not subjected to this limitation is kMC ([Deo et al., 2005](#); [Lin & Chrzan, 1999b](#);

Stukowski et al., 2015). Therefore we choose a mobility function extracted from the kMC simulations described by Stukowski *et al.* (Stukowski et al., 2015), which includes non-Schmid effects.

From the kMC simulations results, the following function provides the dependence of the velocity function with the stress and temperature:

$$v(s, T) = A \cdot s^n \cdot f(s, T) \cdot [1 - B \cdot f(s, T)] \cdot \text{sign}(\tau^\alpha) \quad (5.5)$$

$$f(s, T) = \exp \left\{ -\frac{\Delta H_0}{k_B T} (1 - s^p)^q \right\}$$

where k_B is the Boltzmann constant; T is the absolute temperature; A , B , n , p , and q are all fitting parameters obtained from the kMC simulations and τ^α is the resolved shear stress. Since non-Schmid effects are already included in this mobility law, the resolved shear stress can be defined as projections of the applied load on the slip system. For small elastic strains, it reads as

$$\tau^\alpha = \sigma : \mathbf{M}^\alpha \approx \mathbf{S} : \mathbf{M}^\alpha; \quad (5.6)$$

where \mathbf{S} is the second Piola-Kirchhoff stress tensor, that can be expressed as a function of the elastic deformation gradient \mathbf{F}_e and the stiffness tensor \mathbf{C} ,

$$\mathbf{S} = \frac{\mathbf{C}}{2} (\mathbf{F}_e^T \mathbf{F}_e - \mathbf{I}) \quad (5.7)$$

We have chosen to work with a non dimensional scalar form of the stress tensor defined as

$$s = \frac{|\tau^\alpha| - \tau_{pass}}{\tau_p}, \quad (5.8)$$

where τ_p is the Peierls stress; τ_{pass} is the passing stress, defined as a function of the shear modulus μ , the local dislocation densities $\rho^{\alpha'}$, and the interaction parameters $\xi_{\alpha\alpha'}$ that characterize the interaction strength between slip systems α and α' as a result of the possible interaction types self, coplanar, collinear, mixed-asymmetrical junction (orthogonal), mixed-symmetrical junction (glissile) and edge junction (sessile) (Queyreau

et al., 2009):

$$\tau_{pass} = \mu b \sqrt{\sum_{\alpha'} \xi_{\alpha\alpha'} \rho^{\alpha'}}; \quad (5.9)$$

ΔH_0 is the activation enthalpy when s is equal to zero.

5.2.2 Dislocation density law

The evolution of the dislocation density on each slip system serves as an internal variable describing the current microstructural state. Different models that calculate the flow stress from dislocation densities have been discussed in the literature (Arsenlis & Parks, 1999, 2002; Arsenlis et al., 2004; Cheong & Busso, 2004; Ma & Roters, 2004; Ma et al., 2006, 2007; Roters et al., 2010). In this work we have used the model presented by Roters (Roters, 2011),

$$\begin{cases} \rho^\alpha(0) = \rho_0^\alpha, \\ \rho^\alpha(n+1) = \rho^\alpha(n) + [d\rho_{mult}^\alpha + d\rho_{ann}^\alpha] dt \end{cases} \quad (5.10)$$

where ρ_0^α is the initial dislocation density, $d\rho_{mult}^\alpha$ and $d\rho_{ann}^\alpha$ represent respectively the dislocation multiplication and dislocation annihilation rate terms on slip system α . In this model, dislocation multiplication is treated as being proportional to the inverse mean free path of the dislocations, λ^α :

$$d\rho_{mult}^\alpha = \frac{|d\gamma^\alpha|}{b^\alpha \lambda^\alpha}, \quad (5.11)$$

defined as a function of the grain size d_{grain} and a hardening constant c ,

$$\frac{1}{\lambda^\alpha} = \frac{1}{d_{grain}} + \frac{\sqrt{\rho^\alpha}}{c} \quad (5.12)$$

Dislocation annihilation occurs spontaneously when dipoles approach to a spacing below d_{edge} :

$$d\rho_{ann}^\alpha = -\frac{2d_{edge}}{b^\alpha} \rho^\alpha |d\gamma^\alpha| \quad (5.13)$$

5.3 Simulation details

The constitutive model described in Section 5.2 has been implemented in the the Düsseldorf Advanced Material Simulation Kit (DAMASK) ([Roters et al., 2012](#)). This open source software allows the integration of the constitutive models within different solvers for mechanical equilibrium: a spectral method based solver and two commercial FEM solvers as Abaqus and MSC.Marc. Based on its performance for single crystals, we have chosen the spectral method solution described in ([Eisenlohr et al., 2013](#); [Shanbhag et al., 2014](#)) to perform tensile tests in single crystal tungsten.

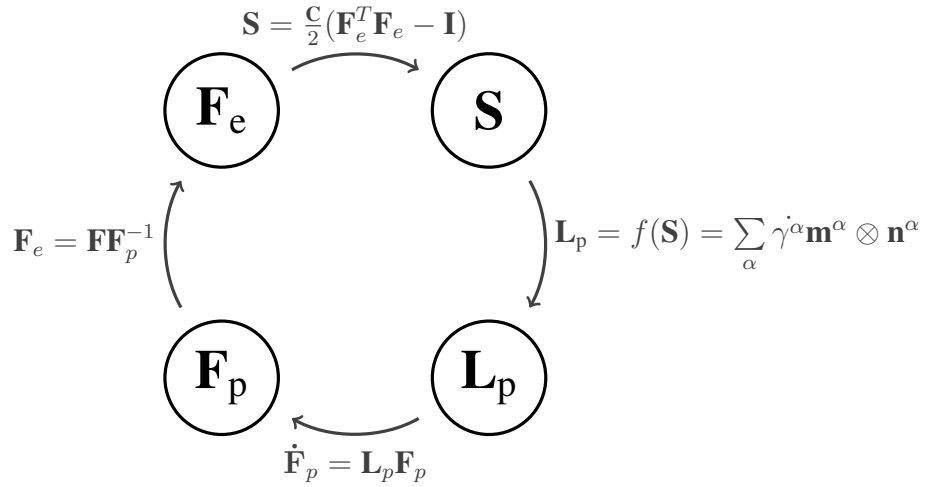


FIGURE 5.1: Predictor-corrector scheme to calculate the stress \mathbf{S} as a function of \mathbf{F} .

The set of nonlinear equations (5.1), (5.2), (5.3) and (5.7), for which the dependency is summarized in Fig. 5.1, needs to be solved iteratively. In DAMASK, a Newton-Raphson scheme is used to do that and the velocity gradient \mathbf{L}_p is chosen as a predictor. Since \mathbf{L}_p is used as a predictor, the tangent $\frac{\delta \mathbf{L}_p}{\delta \mathbf{S}}$ needs to be computed as well by the plasticity model. More details about the implementation are given in ([Kords & Raabe, 2013](#)). Choosing \mathbf{L}_p as initial step represents an advantage for the inversion of the Jacobi matrix during the Newton-Raphson algorithm, since the dimension of the Jacobi matrix is equal to the number of independent variables of the quantity that it is used as predictor, and these are its 9 components. However, when starting with \mathbf{L}_p , slip rates $\dot{\gamma}^{\alpha}$ need to be calculated from the stress, which may generate important deviations as a consequence of the exponential nature of the shear rates ([Roters et al., 2010, 2012](#)).

A schematic diagram of the multiscale procedure that links atomistic, kMC and CP simulations is shown in Fig. 5.2, where the relation between \mathbf{L}_p and the dislocation velocities v^{α} is achieved via eq. 5.3. The core of the dislocation-based CP model is in

the formulation of this eq. 5.3. While some models include mechanical twinning and phase transformations, we have only considered dislocation glide as the main carrier of plastic deformation.

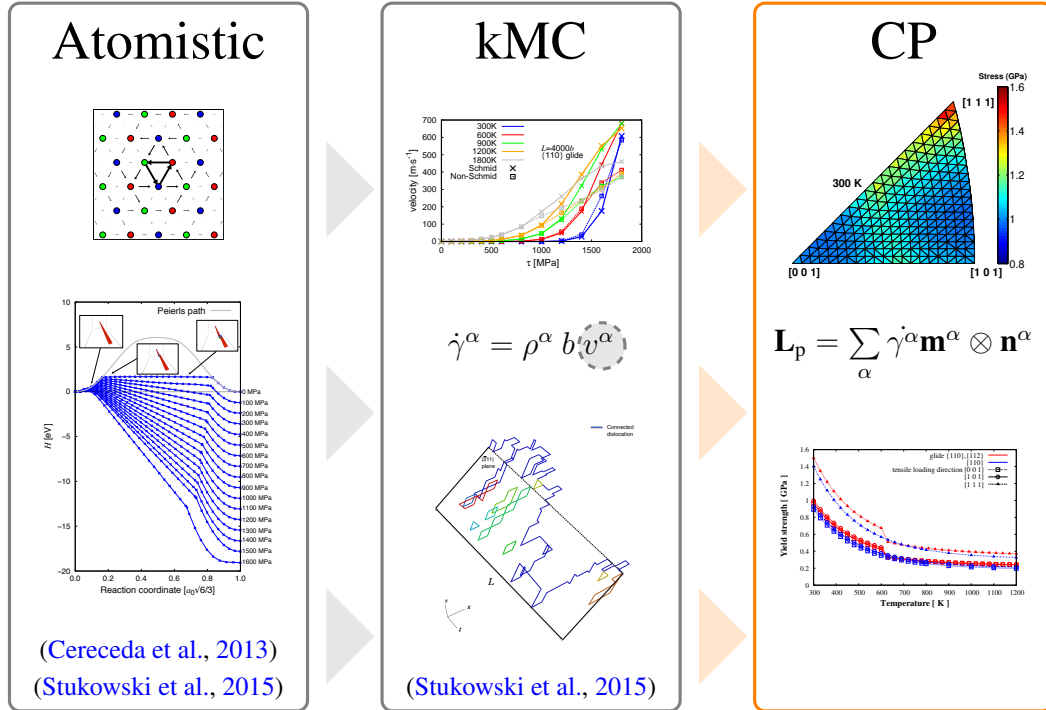


FIGURE 5.2: Schematic diagram of the multiscale approach that links atomistic, kinetic Monte Carlo and crystal plasticity simulations. In step I we use semiempirical interatomic potentials to calculate the energetic of single dislocation motion. In step II we use kMC parameterized with atomistic data to fit a mobility function to the velocity vs. stress vs. temperature. Finally, in step III, we use those mobility functions to characterize the velocity gradient in CP.

The periodic volume element for the material point simulations is taken as a cube of initial dimension $d_{x,0} = d_{y,0} = d_{z,0} = 1$ m, discretized by $4 \times 4 \times 4$ voxels (Eisenlohr et al., 2013).

5.4 Results

In this section we perform uniaxial tensile tests in single crystal tungsten under different crystallographic orientations in the standard triangle using the CP framework just described. We study the crystal response as a function of the number and type of slip planes, whether or not non-Schmid behavior is considered, and temperature.

TABLE 5.2: Fitting parameters of the mobility function defined in eq. 5.5 (obtained from ([Stukowski et al., 2015](#))).

	Schmid		Non Schmid		
	$\{1\bar{1}0\}$ glide	$\{112\}$ glide	$\{1\bar{1}0\}$ glide	$\{112\}$ glide	
				T \leq 600 K	T > 600 K
A	3693.4	755.59	1444.23	2084.19	3415.97
B	0.97	0.50	0.72	0.68	0.89
n	2.47	0.38	1.78	1.39	2.72
p	0.16	0.22	0.26	0.81	0.19
q	1.00	1.01	1.40	2.45	1.32

TABLE 5.3: List of parameters for the constitutive model. The last row represents the six coefficients of the interaction matrix.

Parameter	Value	Units	Parameter	Value	Units
k_B	8.617×10^{-5}	eV K $^{-1}$	τ_p	2.03	GPa
ΔH_0	1.63	eV	μ	161	GPa
a_0	3.143×10^{-10}	m	$ \mathbf{b} $	2.72×10^{-10}	m
ρ_0^α	1.0×10^{12}	m $^{-2}$	d_{grain}	2.7×10^{-5}	m
c	10		d_{edge}	2.72×10^{-10}	m
$\xi_{\alpha\alpha'}$	0.009	0.009	0.72	0.05	0.09
					0.06

The values of the parameters defined in the constitutive model are listed in tables 5.2 and 5.3. Most of the parameters of these tables have been obtained directly from kMC simulations ([Stukowski et al., 2015](#)) or first principle and atomistic calculations ([Cereceda et al., 2013](#)) with the EAM interatomic potential ([Marinica et al., 2013](#)) used to parameterize the kMC model. For those parameters not derived from atomistic or kMC simulations (ρ_0^α , d_{grain} , c , d_{edge} , $\xi_{\alpha\alpha'}$) the values used merit some discussion. The initial dislocation density is defined as $\rho_0^\alpha \approx 1/L^2 \approx 10^{12}\text{m}^{-2}$, with $L = 4000b$ the average dislocation segment length. The grain size is taken from ([Lassner & Schubert, 1999](#)) where $d_{grain} = 2.7 \times 10^{-5}\text{m}$. The interaction coefficients $\xi_{\alpha\alpha'}$ were computed for elastic isotropic iron ([Queyreau et al., 2009](#)), which make them suitable also for elastic isotropic tungsten. Since this work focuses on the yield stress and not on the entire stress-strain curve, the values assigned to these mentioned parameters that mainly

influence the plastic regime of the model are considered a valid approximation.

Uniaxial tensile tests

The boundary conditions chosen to represent the uniaxial tensile tests along the z -direction are

$$\frac{\dot{\mathbf{F}}}{10^{-3} s^{-1}} = \begin{bmatrix} * & * & * \\ 0 & * & * \\ 0 & 0 & \frac{d_z}{d_{z,0}} \end{bmatrix} \quad \text{and} \quad \frac{\mathbf{P}}{Pa} = \begin{bmatrix} 0 & 0 & 0 \\ * & 0 & 0 \\ * & * & * \end{bmatrix}, \quad (5.14)$$

with “*” denoting components for which complementary conditions are prescribed. These conditions are applied for 100 s in 300 equal increments resulting in a final z -tension of 0.1. Different loading orientations in the standard triangle are characterized by their Bunge Euler angles φ_1 , ϕ and φ_2 .

For a bcc slip system defined by slip direction \mathbf{m}^α and normal to the slip plane \mathbf{n}^α , the Schmid factor for an applied tensile load along direction \mathbf{l} can be calculated by

$$\cos\Phi \cos\lambda = \frac{\mathbf{l} \cdot \mathbf{m}^\alpha}{\|\mathbf{l}\| \cdot \|\mathbf{m}^\alpha\|} \cdot \frac{\mathbf{l} \cdot \mathbf{n}^\alpha}{\|\mathbf{l}\| \cdot \|\mathbf{n}^\alpha\|} \quad (5.15)$$

In this work, the Schmid factor has been computed for 231 crystallographic orientations uniformly distributed in the standard triangle. The maximum Schmid factor indicates the primary slip system for each loading direction. Fig. 5.3a shows three regions where the operational slip system corresponds to $\{110\}$, $\{112\}$ or $\{1\bar{1}2\}$ anti-twinning (AT) families. These results from Fig. 5.3a are in agreement with experimental work from Franciosi *et al.* ([Franciosi et al., 2015](#)). The envelope of maximum Schmid factor plotted in fig. 5.3b shows not only the operational slip family but also the value of the Schmid factors.

The resulting component of the *first Piola-Kirchoff stress* along loading direction is plotted in Fig. 6.2 as a function of the *Biot strain* $\mathbf{E}^{(1)} = \mathbf{U} - \mathbf{I} = (\lambda_i - 1)\mathbf{u}_i \otimes \mathbf{u}_i$, with λ_i and \mathbf{u}_i being the eigenvalues and eigenvectors of the right stretch tensor $\mathbf{U} = \sqrt{\mathbf{F}^T \mathbf{F}}$. We have chosen to plot the *first Piola-Kirchoff stress* versus the *Biot strain* because they represent the engineering stress and engineering strain respectively.

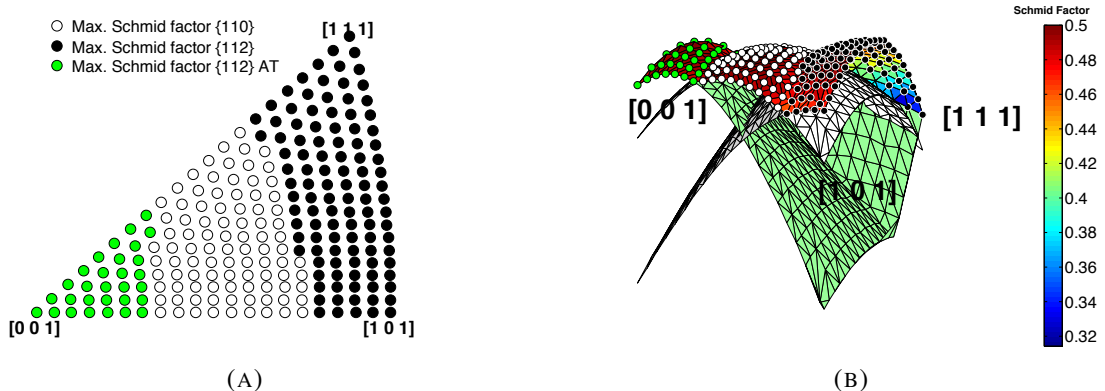


FIGURE 5.3: Discretization of the standard triangle into a regular grid of 231 points representing different crystallographic orientations. 5.3a represents the the slip family with maximum Schmid factor. 5.3b shows the three dimensional surface of the Schmid factor. The envelope of maximum Schmid factor is colored coded according to Fig.5.3a.

The uniaxial loading directions shown in Fig. 6.2 are the three corners of the standard triangle: [0 0 1], [1 0 1], [1 1 1]. As it is expected for an isotropic material like tungsten, there is no orientation dependence on the *Young's modulus*, represented by the slope of the elastic regime². On the other hand, there is an orientation dependence of the yield strength that matches observations from previous experiments and simulations in bcc metals (Brunner, 2010; Keh, 1965; Narayanan et al., 2014a).

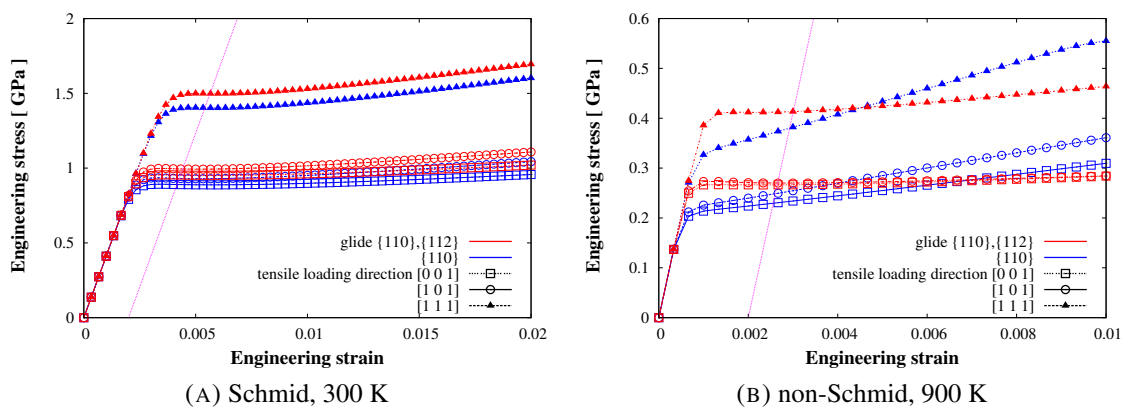


FIGURE 5.4: Mechanical response of bcc W single crystal predicted by our constitutive model under conditions of uniaxial tension along different loading directions and slip systems. The stress-strain behavior is represented using the components of the *first Piola-Kirchoff stress* and the *Biot strain* along the loading direction z . Parameters from Table 5.2 are taken for (a) Schmid behavior and (b) non-Schmid behavior.

²The value of the Young's modulus for Tungsten used in our simulations is 411 GPa (Lassner & Schubert, 1999).

The yield strength σ_y has been determined using the 0.2% strain offset method, where a straight line is constructed parallel to the elastic portion of the stress-strain curve for a strain offset of 0.002. The stress corresponding to the intersection of this line and the stress-strain curve as it bends over the plastic region is defined as the yield strength (Callister & Rethwisch, 2009). Figure 5.5 represents the yield strength as a function of the temperature for uniaxial tensile tests along the three corners of the standard triangle. As it is reported in previous works for bcc metals (Brunner & Diehl, 1991; Kuramoto et al., 1979; Narayanan et al., 2014a), yield strength decreases with temperature. Two different scenarios of slip have been considered in Fig. 6.2 and Fig. 5.5: (i) only the twelve $\{110\}\langle111\rangle$ slip systems are active; (ii) $\{110\}\langle111\rangle$ and $\{112\}\langle111\rangle$ slip systems are active. We can see from Fig. 5.5 that the values of yield strength are higher if the non-Schmid effects are considered. Below 600 K, non-Schmid behavior also predicts slightly different results for the two scenarios of slip.

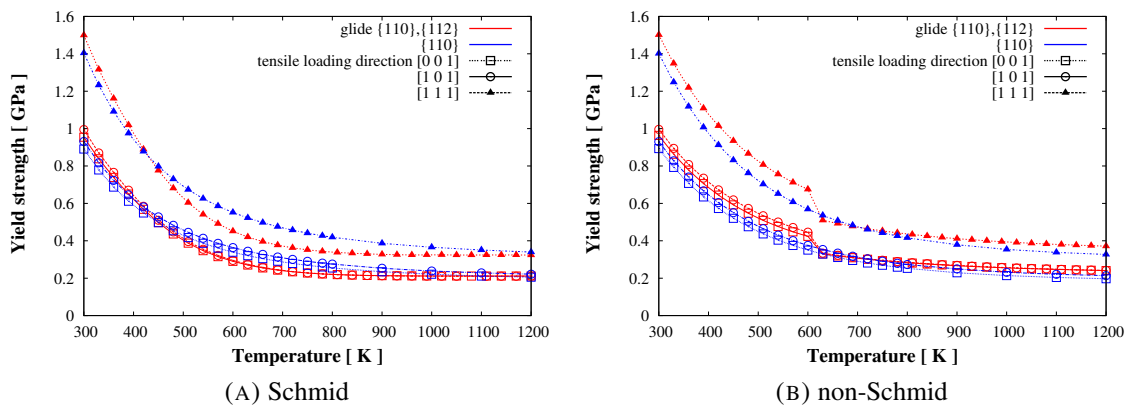


FIGURE 5.5: Temperature dependence of yield strength for different tensile loading orientations and active slip systems. 5.5a represents Schmid behavior and 5.5b represents non-Schmid behavior.

Figure 5.6 shows the loading directions corresponding to the five highest and lowest values of yield strength. Figure 5.7 shows the yield strength under uniaxial tension for 231 uniformly distributed loading directions within the standard stereographic triangle. The percentage difference between the yield strength with non-Schmid behavior, σ_y^{NS} (fig. 5.7b), and the yield strength with Schmid behavior, σ_y^S (fig. 5.7a), is defined as $\left| \frac{\sigma_y^{NS} - \sigma_y^S}{(\sigma_y^{NS} + \sigma_y^S)/2} \right|$, and its value decreases with temperature (fig. 5.7c). We can conclude from Fig. 5.6 and fig. 5.7 that the maximum yield strength is always achieved when loading along $[111]$ while the loading direction of minimum yield strength depends on the temperature range and whether non-Schmid effects behavior are considered.

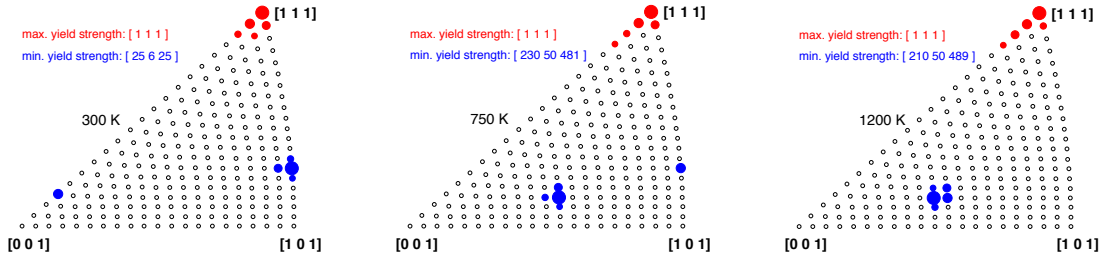


FIGURE 5.6: Loading directions corresponding to the five highest and lowest values of yield strength for uniaxial tensile tests at 300, 750 and 1200 K. The biggest blue circle represents the absolute minimum and the biggest red circle represents the absolute maximum.

5.5 Summary

To summarize, the main findings of this chapter can be condensed into the following aspects:

- We have performed single material point simulations in monocrystalline tungsten using a CP framework whose constitutive law is physically-based on the dislocation velocities obtained using a kMC model (Stukowski et al., 2015). The entire set of parameters required to formulate the CP framework are obtained using atomistic simulations and one EAM interatomic potential (Marinica et al., 2013).
- We have incorporated in our model non-Schmid effects and compared their influence in the results with respect to the classic Schmid's law. The results shown in Fig.5.5 and Fig. 5.7 reveal that adding the contribution of non-Schmid effects rises the values of yield strength. The difference between Schmid and non-Schmid behaviors also decreases when increasing the temperature.
- We have compared the results obtained when activating only $\{110\}\langle111\rangle$ slip systems and a combination of both $\{110\}\langle111\rangle$ and $\{112\}\langle111\rangle$ slip systems. The results shown in Fig. 5.5 confirm the low impact of activating additional $\{112\}$ planes even when they are considered active during slip. These results, in agreement with previous work from Caillard (Caillard, 2010a,b), show that for the entire range of temperature studied, slip of screw dislocations takes place primarily on $\{110\}$ planes.
- In agreement with previous works in other bcc metals (Brunner & Diehl, 1991; Kuramoto et al., 1979; Narayanan et al., 2014a), results in Fig. 5.5 show that the yield strength rapidly decreases with temperature in single crystal tungsten.

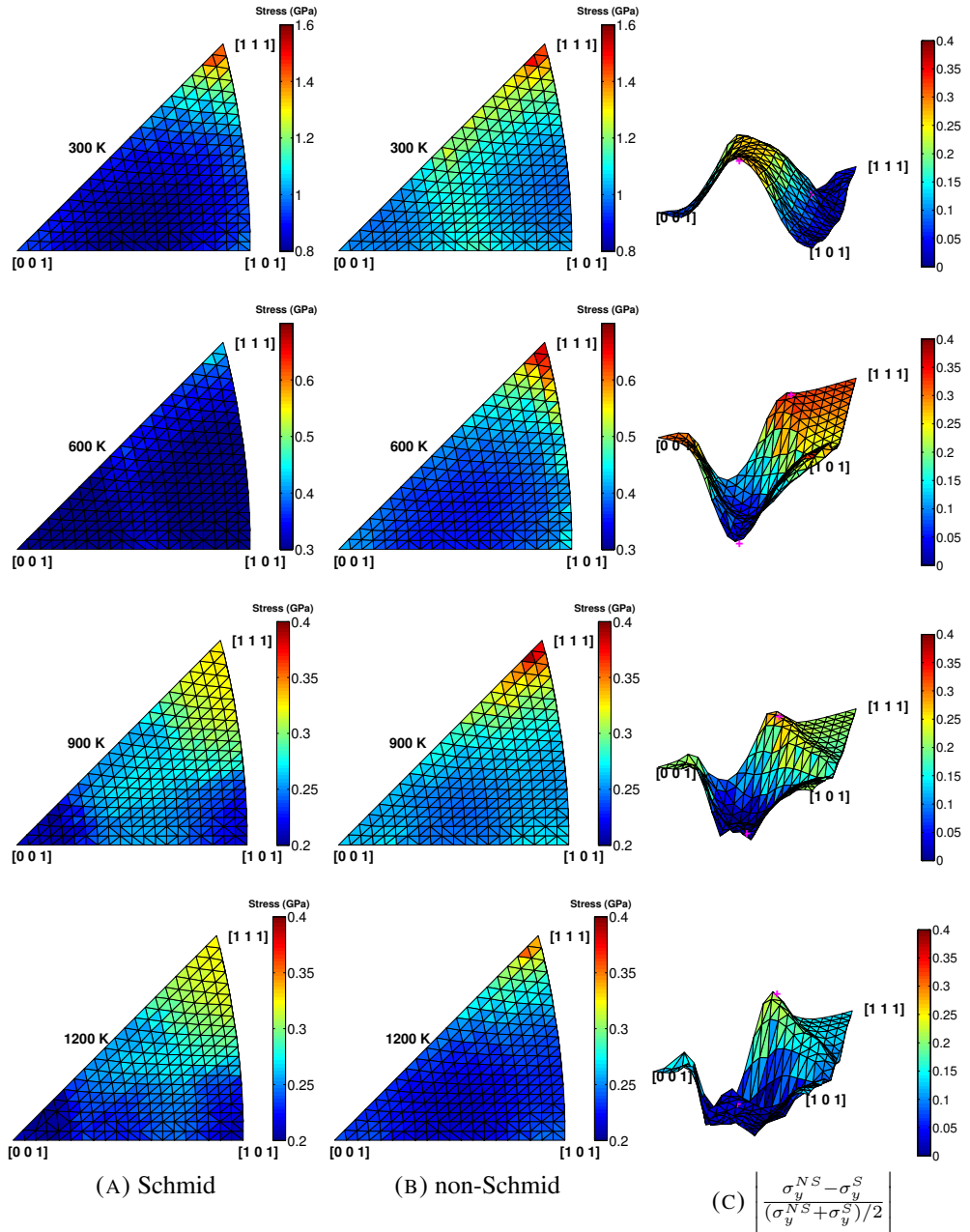


FIGURE 5.7: Yield strength for uniaxial tensile tests along 231 uniformly distributed crystallographic orientations in the standard triangle at different temperatures. Schmid and non-Schmid behaviors are studied separately. $\{1\bar{1}0\}\langle 1\bar{1}1\rangle$ and $\{1\bar{1}2\}\langle 1\bar{1}1\rangle$ slip systems are active. Fig. 5.7c represents the percentage difference between non-Schmid and Schmid.

- The yield strength shown in Fig. 6.2, Fig. 5.5, and Fig. 5.7 clearly depends on the loading orientation of the tensile test. Among the 231 uniformly distributed crystallographic orientations studied here, we observe in Fig. 5.6 that the loading orientation of maximum yield is always [1 1 1] while the loading orientation of minimum yield strength depends on the temperature.

Chapter 6

Unraveling the temperature dependence of the yield strength in single-crystal tungsten using atomistically-informed Crystal Plasticity simulations

6.1 Introduction

The plastic behavior of bcc single crystals at low to medium homologous temperatures is governed by the motion of $\frac{1}{2}\langle 111 \rangle$ screw dislocations on close-packed crystallographic planes (Cai et al., 2004b; Hartmaier & Gumbsch, 2005b; Vitek, 2004b). Under these conditions there are two particularities that make bcc metals unique in relation to their deformation characteristics. The first one is the thermally-activated nature of screw dislocation glide, a consequence of the compact (non-planar) structure of the dislocation core at the atomistic level (Li et al., 2012; Samolyuk et al., 2013; Wurster et al., 2010). This feature is also responsible for the high intrinsic friction stresses reported in the literature for bcc crystals and alloys (Romaner et al., 2010; Samolyuk et al., 2013). The second is the breakdown of the standard geometric projection rule for the resolved shear stress (RSS) from the total stress tensor known as *Schmid law* (Schmid & Boas, 1935). This is owed to both specific crystallographic properties of the bcc lattice structure as well as to the coupling between the core and non-glide components of the

stress tensor, which –to the best of our understanding– is unique to bcc crystals (Brinckmann et al., 2008; Bulatov et al., 1999; Chaussidon et al., 2006; Gröger & Vitek, 2005; Woodward & Rao, 2001). These anomalies have been the subject of much research and discussion going back to the 1960’s and earlier (Duesbery, 1969; Duesbery & Foxall, 1969; Hull et al., 1967; Takeuchi et al., 1967), both experimentally and –more recently– using computational atomistic models.

In regards to the first point above, at low stresses slip proceeds via the thermally activated nucleation of steps on the dislocation line, known as *kink pairs*, and their subsequent sideward relaxation. For a constant strain rate, this gives rise to the characteristic temperature dependence of the flow stress in bcc single crystals, which has been observed for all refractory metals and is considered to be a principal signature of their plastic response (Ackermann et al., 1983; Chaussidon et al., 2006; Gordon et al., 2010; Seeger, 1981; Taylor, 1992; Yang et al., 2001). The flow stress is considered to be composed of thermal and athermal contributions, with the latter depending on temperature only as the elastic moduli. For its part, dislocation glide is thought to occur on {110}, {112}, and even {123} planes, depending on temperature and stress, over a periodic energy landscape known as the *Peierls* potential U_P . The connection between the experimentally measured flow stress and this periodic energy potential is via the critical stress for which U_P vanishes at zero temperature, known as the Peierls stress σ_P . Theoretically then, the flow stress at very low temperatures (≤ 25 K) is thought to represent the macroscopic equivalent of σ_P as the temperature approaches 0 K. σ_P can thus be unequivocally defined and has been the object of considerable numerical work since the first atomistic models were devised by Vitek and co-workers starting in the 1970s (Vitek & Yamaguchi, 1973).

For their part, non-Schmid effects were detected early on, in tests done in the 1930’s by Taylor in the wake of his seminal works on plastic flow and strain hardening (Taylor, 1928, 1934a,b). Subsequent observations and measurements (Christian, 1983; Escaig, 1968, 1974; Pichl, 2002; Šesták & Zárubová, 1965; Sherwood et al., 1967; Zwiese & Diehl, 1979), and a rigorous theoretical formulation of the problem (Chaussidon et al., 2006; Duesbery & Vitek, 1998; Gröger et al., 2008a,b; Gröger & Vitek, 2005; Ito & Vitek, 2001; Woodward & Rao, 2001) have established non-Schmid behavior as a principal tenet of bcc plasticity, one that absolutely must be accounted for in order to understand bcc plastic flow. The underlying ideas are (i) that the resolved shear stress is not independent of the sign of the stress in glide planes of the $\langle 111 \rangle$ zone (the so-called *twinning/antitwinning* asymmetry), and (ii) that non-glide components of the

stress tensor –*i.e.* those which are perpendicular to the Burgers vector– play a role on the magnitude and sign of the RSS on the glide plane of interest.

Areas where we do not have a complete understanding of bcc plastic picture include the value of the flow stress at near zero absolute temperatures, the meaning of the so-called *knee* temperature, and the onset of athermal flow. In the last two decades, computer simulation has unquestionably emerged as discipline capable of shedding light on these issues on (almost) equal footing with experiments, providing physically-substantiated explanations micro and macroscopic phenomena . These include the use and application of density-functional theory methods ([Dezerald et al., 2015, 2014](#); [Ventelon & Willaime, 2007](#); [Ventelon et al., 2013](#); [Weinberger et al., 2013](#)), semi empirical atomistic calculations and molecular dynamics calculations ([Chang et al., 2001](#); [Gilbert et al., 2011](#); [Komanduri et al., 2001](#); [Queyreau et al., 2011](#)), kinetic Monte Carlo ([Cai et al., 2002](#); [Deo & Srolovitz, 2002](#); [Lin & Chrzan, 1999a](#); [Scarle et al., 2004](#); [Stukowski et al., 2015](#)), and crystal plasticity (CP) ([Brünig, 1997](#); [Dao & Asaro, 1993](#); [Qin & Bassani, 1992](#)), to name but a few. In general, while there is no doubt that the intricacies of $\frac{1}{2}\langle 111 \rangle$ screw dislocation glide –including its thermally activated nature and deviations from Schmid law– cannot but be resolved using methods capable of atomistic resolution, one must recognize that, at the same time, flow is a phenomenon involving statistically-significant amounts of dislocations and –as such– cannot be captured solely by resorting to atomistic calculations.

Modeling thermally-activated flow and non-Schmid effects in bcc systems has been the subject of much work, starting in the 1980s but particularly in recent times . Different authors have considered different subsets of the {110}, {112}, and {123} families of glide planes, with non-Schmid effects ([Alankar et al., 2014](#); [Knezevic et al., 2014](#); [Koester et al., 2012](#); [Kuchnicki et al., 2008](#); [Lee et al., 1999](#); [Lim et al., 2015a,b, 2013](#); [Narayanan et al., 2014b](#); [Patra et al., 2014](#); [Weinberger et al., 2012](#)) or without them ([Erieau & Rey, 2004](#); [Hamelin et al., 2011](#); [Hölscher et al., 1991, 1994](#); [Kitayama et al., 2013](#); [Ma et al., 2007](#); [Peeters et al., 2000](#); [Raabe, 1995a,b](#); [Raabe et al., 1994](#); [Raphael & Van Houtte, 1985](#); [Stainier et al., 2002](#)). Of particular interest are some recent simulations where the flow rule is directly formulated on the basis of screw dislocation properties in Fe ([Alankar et al., 2014](#); [Koester et al., 2012](#); [Lim et al., 2015b](#); [Narayanan et al., 2014b](#); [Patra et al., 2014](#)), Ta ([Knezevic et al., 2014](#); [Kuchnicki et al., 2008](#); [Lim et al., 2015a, 2013](#)), Mo ([Lim et al., 2015a, 2013](#); [Weinberger et al., 2012](#)), W ([Knezevic et al., 2014](#); [Lee et al., 1999](#); [Lim et al., 2015a, 2013](#); [Weinberger et al., 2012](#)), Nb ([Lim et al., 2015a](#)), and non-Schmid effects are captured in the sense proposed by Vitek

and Bassani ([Duesbery & Vitek, 1998](#); [Gröger et al., 2008a,b](#); [Qin & Bassani, 1992](#)). However, albeit very useful for certain applications, all these works resort to some kind or another of (i) parameter fitting with experimental data, which prevents their use in regions of the parameter space outside the range of fitting and does not link the effective (*macroscopic*) response to exclusively fundamental atomistic properties and features or (ii) incomplete formulation of non-Schmid effects.

In this work, we provide a unified computational methodology consisting of rate-dependent crystal plasticity calculations parameterized entirely and exclusively to atomistic calculations. We show that a full description of non-Schmid effects, together with the state of the art in terms of our understanding of thermally-activated screw dislocation motion, suffices to capture the experimentally measured temperature dependence of the flow stress in tungsten (W). This is achieved in a fully classical framework, without the need for quantum effects recently invoked to explain the long standing discrepancy observed between the experimentally-measured flow stress below 25 K and calculated values of the Peierls stress ([Provile et al., 2012](#)). Our methodology also captures the athermal limit of W to within 5% of the experimental value. We emphasize that this agreement is reached without fitting to any experimental data, all the parameterization is done from first principles atomistic calculations.

This chapter is organized as follows. After this introduction, we provide a detailed description of the parameterization procedure, including the formulation of the dislocation mobility law. The main results achieved are presented in Section 6.3 and they include: (i) the validation exercise with experimental data, with special focus on uniaxial tests as a function of temperature for several loading orientations; (ii) the calculation of temperature and strain rate dependent quantities such as material strength and yield surfaces for selected orientations in the stereographic standard triangle.

6.2 Computational methods

The CP method, the integration scheme and the dislocation density model used were already described in Sections 5.2, 5.3 and 5.2.2, respectively. The characterization of non-Schmid effects was also explained in Chapter 4. Therefore, in this section we only describe the formulation of the dislocation mobility law to complete our dislocation-based CP model.

6.2.1 Screw dislocation mobility law

Except at high homologous temperatures and strain rates, screw dislocation motion is the rate-limiting step in bcc crystal deformation (Tang & Marian, 2014). This is certainly true at quasi-static deformation rates ($\approx 10^{-4}$ s $^{-1}$), which is the regime of concern in this work. In the thermally activated regime, screw dislocation motion proceeds via the nucleation of kink-pairs and their subsequent lateral relaxation. At strain rates $\leq 10^{-4}$, kink relaxation is significantly faster than kink-pair nucleation and it can thus be assumed that no new kink-pairs will be nucleated while lateral kink motion is underway. Such assumption leads to the following expression for the total time required for a kink pair to form and sweep a rectilinear screw dislocation segment of length λ^α lying on a given slip plane:

$$t_t = t_n + t_k = J(\tau^\alpha, T)^{-1} + \frac{\lambda^\alpha}{2v_k(\tau^\alpha, T)} \quad (6.1)$$

where t_n is the mean time to nucleate a kink pair, t_k is the time needed for a kink to sweep half a segment length, J is the kink-pair nucleation rate, and v_k is the kink velocity. The kink-pair nucleation rate follows an Arrhenius formulation (Stukowski et al., 2015):

$$J(\tau^\alpha, T) = \frac{\nu_0(\lambda^\alpha - w)}{b} \exp\left(-\frac{\Delta H_{kp}(\tau^\alpha)}{kT}\right) \quad (6.2)$$

where ν_0 is an attempt frequency, w is the width of a kink pair, ΔH_{kp} is the activation enthalpy of a kink pair at stress τ^α , and k is Boltzmann's constant. For its part, the kink velocity can be expressed as (Dorn & Rajnak, 1964; Kocks et al., 1975):

$$v_k(\tau^\alpha, T) = \frac{b\tau^\alpha}{B(T)} \quad (6.3)$$

where B is friction coefficient typically assumed to be linearly dependent on temperature. The dislocation velocity can be obtained after operating with eqs. (6.2) and (6.3) as:

$$v_s = \frac{h}{t_t} = \frac{h}{t_n + t_k} = \frac{2bh\tau^\alpha\nu_0(\lambda^\alpha - w)\exp\left(-\frac{\Delta H_{kp}}{kT}\right)}{2b^2\tau^\alpha + \nu_0B(\lambda^\alpha - w)^2\exp\left(-\frac{\Delta H_{kp}}{kT}\right)} \quad (6.4)$$

where $h = a_0\sqrt{6}/3$ is the distance between Peierls valleys. We note that at low temperatures, or when $t_k \ll t_n$, the second term in the denominator vanishes and one recovers the standard diffusive velocity expression so commonly used in crystal plasticity and

dislocation dynamics:

$$v_s = \nu_0 h \frac{(\lambda^\alpha - w)}{b} \exp\left(-\frac{\Delta H_{kp}(\tau^\alpha)}{kT}\right)$$

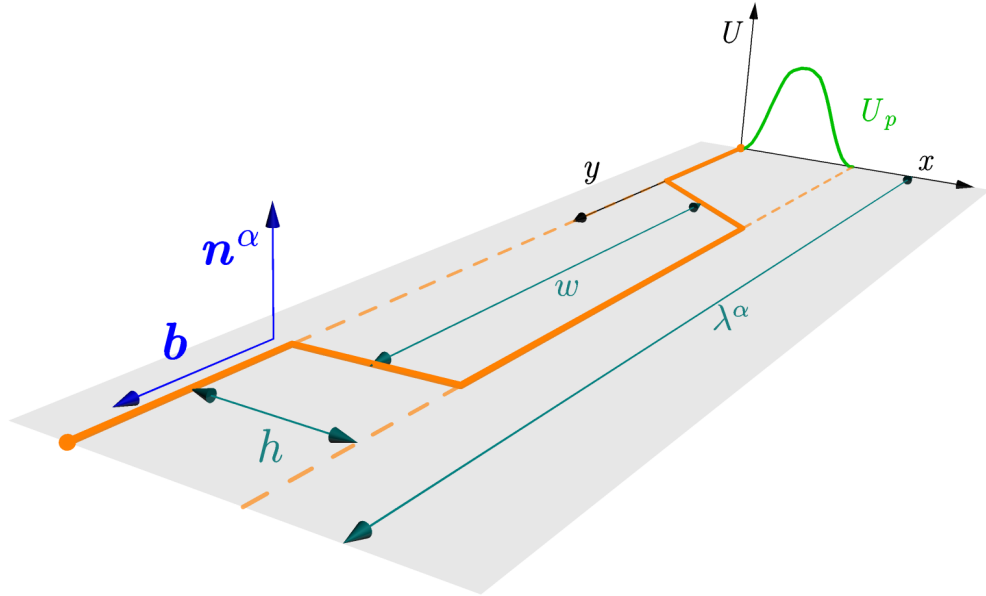


FIGURE 6.1: Schematic depiction of a kink pair on a screw segment of length λ lying on a slip plane n^α (of the $\{110\}$ family). The vertical axis represents the potential energy, with the Peierls potential clearly marked. The dashed line represents the initial equilibrium line position.

The parameterization of eq. (6.4) is a critical step that establishes a physical connection with the scales where kink-pairs are resolved as atomistic entities. This is the first essential piece of physics required to achieve predictive capabilities. We have devoted much effort in past works to calculate the necessary parameters from fundamental models based on semiempirical interatomic potentials (Cereceda et al., 2013; Stukowski et al., 2015). The list of parameters employed in this work and their associated values and units are given in Table 6.1. The physical meaning of some of these parameters is best expressed in pictorial form. Figure 6.1 shows a schematic diagram of the topology of a kink pair lying on the Peierls energy substrate. The figure highlights the physical meaning of each parameter listed in Table 6.1.

At this stage, it is worth to introduce a note about the available slip systems (which establish the running indices of α). Stukowski et al. (2015) have shown that an elementary glide on a $\{112\}$ plane is a composite of two elementary steps on alternate $\{110\}$ planes. Judging by these results, we conclude that glide on any given plane is achieved by way

TABLE 6.1: List of parameters and functional dependences for fitting the CP model. All of these parameters have been obtained using dedicated atomistic calculations. The parameter s represents the normalized shear stress: $s = \frac{\tau'^\alpha}{\sigma_P}$.

parameter	value or function	units
a_0	3.143	Å
b	2.72	Å
h	$a_0\sqrt{6}/3$	Å
C_{11}	523	GPa
C_{12}	202	GPa
C_{44}	161	GPa
ω	9.1×10^{11}	s^{-1}
σ_P	2.03	GPa
B	8.3×10^{-5}	Pa·s
$\Delta H(s; T)$	$\Delta H_0(1 - s^p)^q$	eV
ΔH_0	1.63	eV
p	0.86	-
q	1.69	-
w	11	b
σ_c^χ	$\frac{\tau_c^* + \sigma(a_2 \sin \chi + a_3 \sin(2\chi + \pi/6))}{\cos \chi + a_1 \cos(\pi/3 + \chi)}$	GPa
a_1	0.94	-
a_2	0.71	-
a_3	4.43	-
τ_c^*	2.92	GPa
c	1	-
d_g	2.72	Å
d_{edge}	2.72	Å

of sequential {110} jumps, which constitutes the basis to simulate plastic yielding in the foregoing Sections. This is consistent with recent atomistic simulations ([Cereceda et al., 2013](#)) and experiments ([Caillard, 2010a,b](#); [Marichal et al., 2013](#)) and limits the number of available slip systems to 12.

6.3 Results

In this Section we present results of uniaxial tensile test simulations to explore the dependence of the yield strength on loading direction, temperature and strain rate. First, however, a robust and consistent yield criterion must be defined to extract the yield stress from the raw output data from DAMASK.

6.3.1 Yield criterion

Modern continuum mechanics does not offer any special insight on how to define the yield point¹ nor does traditional mechanics of materials. In fact, it is generally accepted that the definition of yield is not unique, particularly in metals, where dislocation flow is not a singular event but a diffuse process. Perhaps as the result of these conceptual difficulties, modern usage has evolved into that of an arbitrary rule, the 0.2% strain offset rule for determining the yield stress of metals. For other materials there are not even arbitrary rules, there are only individual preferences and proclivities. It is quite apparent then that to define robust yield criteria it is necessary that they be implemented and supported by consistent and meaningful definitions in terms of the stress-strain behavior. This is often difficult when the transition from the elastic to the inelastic regimes is obscured in the global picture of deformation. However, in the present calculations we effectively possess an arbitrary degree of data resolution and can define an unambiguous mathematical criterion.

The preferred method for defining the elastic limit of a ductile material is to compute the second derivative of the stress-strain curve, referred to here generically as $\sigma(\varepsilon)$, and identify the location of the inflection point (Christensen, 2008). The yield point then corresponds to the strain, ε_y , for which $\left| \frac{d^2\sigma}{d\varepsilon^2} \right|$ is maximum. Mathematically:

$$\sigma_y = \sigma(\varepsilon_y), \quad \varepsilon_y := \varepsilon \mid \max \left| \frac{d^2\sigma}{d\varepsilon^2} \right| \quad (6.5)$$

For ductile metals, the location of the maximum of the second derivative represents the point at which dislocation-mediated flow is the major contribution to L (cf. Section 5.2). However, this condition works surprisingly well for other materials such as glassy polymers, where flow might be caused by molecular rearrangement and damage at both the molecular and macroscopic scales (Bowden & Jukes, 1972).

To illustrate the accuracy of the second-derivative method, we plot in Figure 6.2 the first and second derivative of a stress-strain curve corresponding to a [101] uniaxial tensile test of a W single crystal under representative initial conditions. Recall from Section ?? that the stress and strain metrics of choice are P and B , and so we plot $\frac{dP_{zz}}{dB_{zz}}$ and $\frac{d^2P_{zz}}{dB_{zz}^2}$ specifically.

The inflection point –marked by a vertical dashed line in the figure– occurs for $\varepsilon_y = 0.1105\%$, for which a value of $\sigma_y = 0.452$ GPa is obtained. The figure also shows the

¹Also referred to as elastic limit, proportionality limit, yield stress, etc.

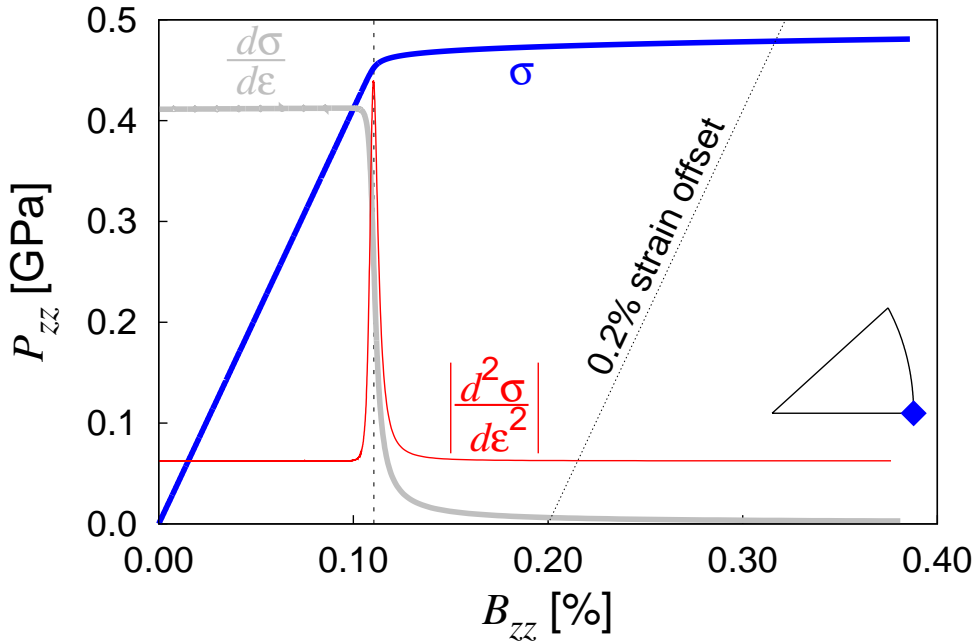


FIGURE 6.2: Evolution of the stress P_{zz} with deformation B_{zz} during a CP simulation of a uniaxial tensile test with [101] loading orientation (as depicted in the standard triangle). The first and second derivatives of the stress w.r.t. to the strain are also plotted to illustrate the method of identification of the yield point according to this criterion.

Also shown is the intercept of the curve with the 0.2% strain offset criterion line.

0.2% strain offset criterion, which –by contrast– gives $\varepsilon_y = 0.3167\%$ and $\sigma_y = 0.479$ GPa, *i.e.* approximately a 6% difference between values obtained applying each criteria.

However, determining the first and second derivatives of the stress-strain relation can become numerically intensive, especially when evaluating thousands of curves as is the case in this work. An approximation to this method that works particularly well for linear-elastic materials that display a clear elastic-to-plastic transition is to take the yield point as the first point in the $\sigma(\varepsilon)$ function that satisfies:

$$\frac{\sigma}{\varepsilon} > E(1 - \delta)$$

i.e. σ_y is measured as the stress for which a departure from linearity (as set by the elastic regime) larger than some small value δ is observed in the stress-strain relation. We have found that a value of $\delta \approx 0.01$ is sufficient to predict the value of σ_y within a small error relative to the value furnished by the second-derivative method. By way of example, for the curve shown in Fig. 6.2 and $\delta = 0.01$, we find a values of $\varepsilon_y = 0.1055\%$ and $\sigma_y = 0.435$ GPa, or less than a 4% difference with the numbers according to the second-derivative criterion. With this reasonable accuracy and the computational advantages

alluded to above, we then use the $\delta = 0.01$ criterion in the remainder of this paper.

6.3.2 Model validation and initial results

Prior to deploying our fully-parameterized CP method for numerically-intensive calculations, it is essential to undergo a thorough exercise of validation. Experimental data from uniaxial tensile tests in W at low strain rates are scant and sporadic, with the main sources listed below:

1. [Argon & Maloof \(1966a\)](#) performed some early experiments at a strain rate of 10^{-4} s^{-1} and temperatures of 77, 199, 293, 373, and 450 K. These authors measured the yield strength for the three vertices of the stereographic triangle [001], [110], and [111] with an initial dislocation density of $\rho_0 \approx 10^{10} \text{ m}^{-2}$.
2. [Raffo \(1969\)](#) analyzed the yielding behavior of arc-melted W between 77 and 680 K at $\dot{\varepsilon} = 8.3 \times 10^{-4} \text{ s}^{-1}$. However, the loading orientation is not given and most of the test were done in compression.
3. [Stephens \(1970\)](#) has carried out compression tests at 150, 300, and 590 K. This researcher focuses on dislocation density evolution and dislocation substructures, however, with a value of $\rho_0 \approx 1.4 \times 10^{14} \text{ m}^{-2}$, notably larger than in other tests.
4. [Brunner \(2000, 2010\)](#) has performed a series of experiments more recently at temperatures between 77 and 800 K. They employed a value of $\dot{\varepsilon} = 8.5 \times 10^{-4} \text{ s}^{-1}$ and loaded the system uniaxially along the [14 9] direction with a starting dislocation density of $5.5 \times 10^9 \text{ m}^{-2}$.

As pointed out in Chapter 4, our CP model is parameterized for tensile tests only and so for validation we focus on the works by [Argon & Maloof \(1966a\)](#) and [Brunner \(2000, 2010\)](#). [Argon & Maloof \(1966a\)](#) focus on multislip by considering mainly loading orientations coincident with the vertices of the standard triangle. Consequently, we replicate their test conditions in our CP model and compare the results obtained by taking account the different elements of the projection tensor (cf. Section 4.2.3). The results are shown in Figure 6.3 for the [111] and the [101] loading orientations, with the insets in both figures showing the relative importance of considering each of the non-Schmid contribution to the projection tensor incrementally. While our calculations are in general good agreement with the [111] test data, they deviate from the experimental

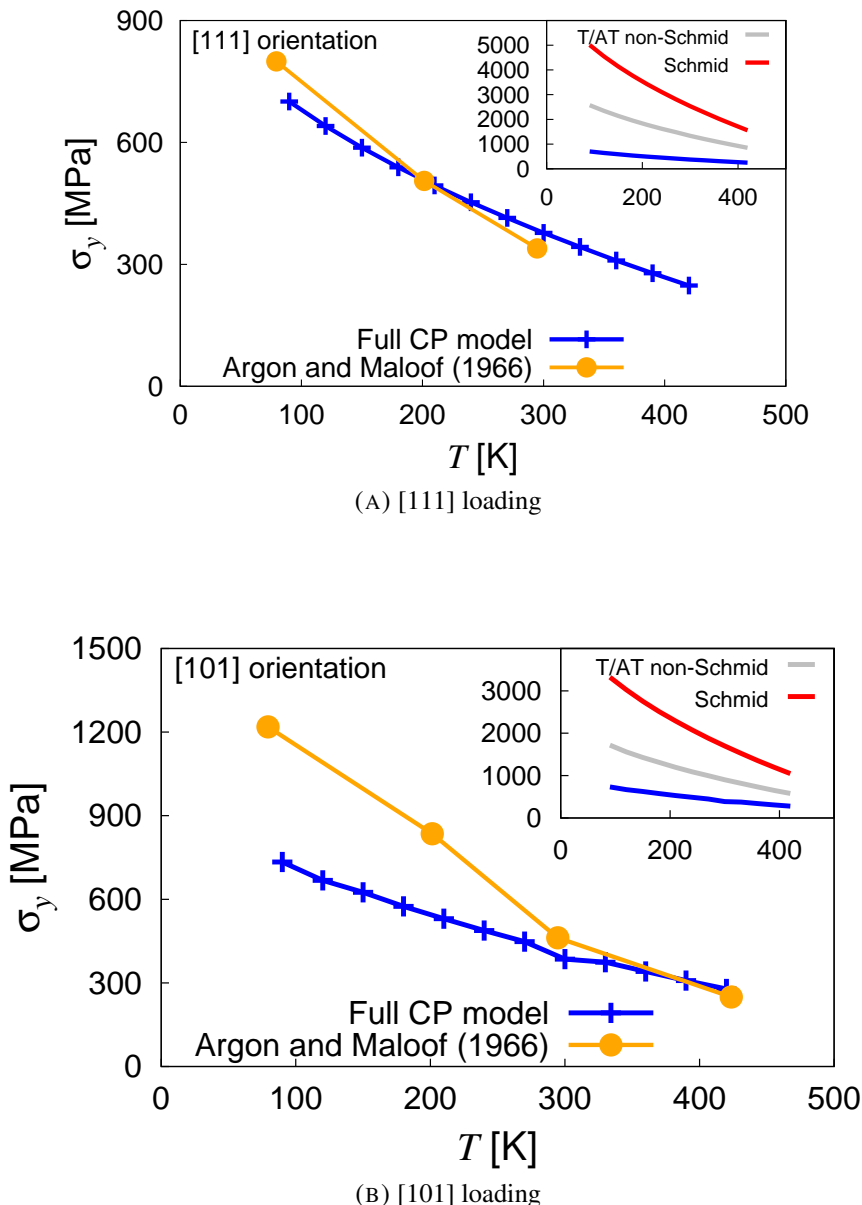


FIGURE 6.3: Yield strength of W single crystals at the conditions used by Argon & Maloof (1966a) in tensile deformation tests under two different loading orientations. The experimental data is shown for comparison. The inset shows the results of CP calculations with different contributions of the projection tensor activated.

results at the two lower temperature points for the [101] orientation. Argon & Maloof (1966a) point out that, at low temperatures, deformation by twinning may play a larger role when loading along [101] relative to other orientations. This may be at the origin of the discrepancy, as twinning is not part of the catalog of deformation mechanisms included in this model.

Next we simulate uniaxial tensile tests under single slip conditions, *i.e.* along crystal orientations near the center of the standard triangle. This corresponds to the experiments by Brunner (2000, 2010) referred to above, which were done more recently with more advanced instrumentation. The results are shown in Figure 6.4, where we also show the curves using the different elements of eq. (4.12). This time, the agreement is striking, particularly again at temperatures above 400 K. Specifically, the *athermal* limit (≈ 710 K) is particularly well reproduced, as is the extrapolated critical stress at 0 K (Peierls stress), which is within 10% of the experimental values.

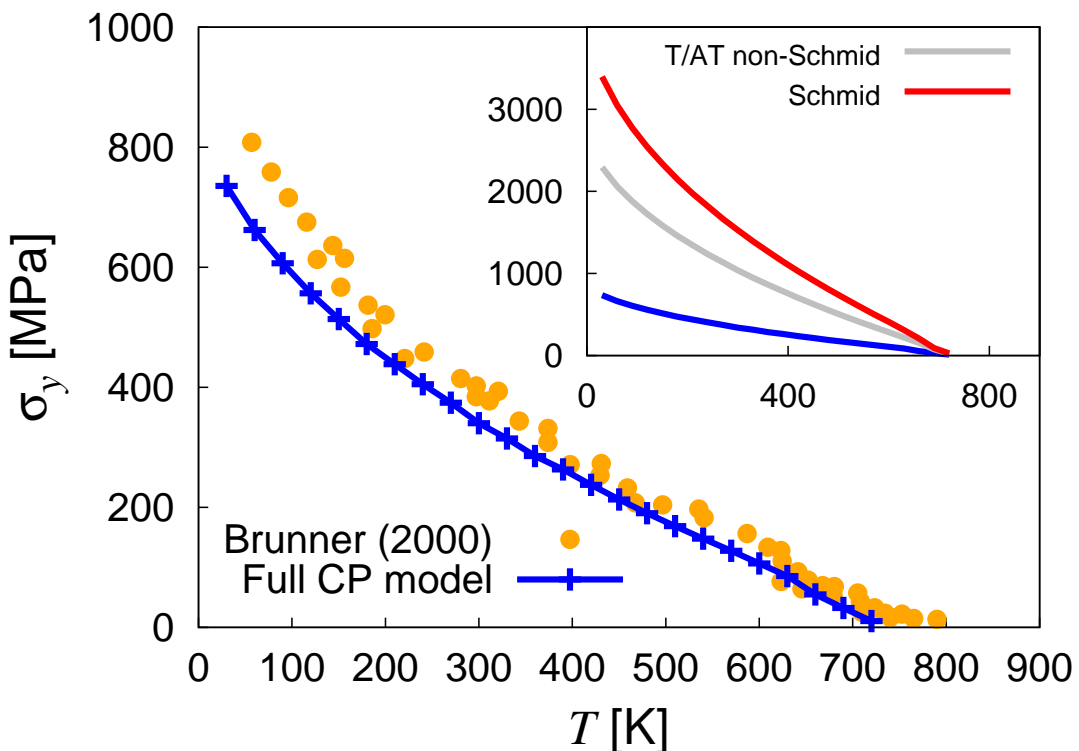


FIGURE 6.4: Yield strength of W single crystals under the conditions used by Brunner (2010) in uniaxial tensile tests. The experimental data is shown for comparison. The inset shows the results of CP calculations with different contributions of the projection tensor activated.

With the confidence conferred on our CP model by the validation procedure, next we proceed to calculate the yield strength for a number of numerically-intensive scenarios. This is the object of the following sections.

6.3.3 Uniaxial tensile tests

6.3.3.1 Dependence on temperature

For these calculations, we have discretized the area of the standard triangle into a uniform grid consisting of 231 nodes, each representing a loading orientation. We begin with calculations at a prescribed strain rate of $\dot{\varepsilon} = 10^{-3}$ s⁻¹. Figure 6.5 shows colored contour plots of the yield stress in the 100-to-600 K temperature range. Areas of high relative yield strength can be seen to concentrate around the vertices of the standard triangle, representing multislip conditions, whereas soft regions develop in two distinct locations of the triangle, one not far from the [112] zonal axis and another near [102]. Note that, to accentuate the differences between hard and soft regions, each contour plot has its own specific numerical scale.

We have extracted the specific location of the global extrema in the standard triangle and plot it as a function of temperature in Figure 6.6a. The hardest direction is consistently the [101], while the softest is seen to revolve around the vicinity of the [112] axis, first along [30 18 41] at 100 K, then along [180 131 271] between 200 and 500 K, and finally rotating towards [9 9 34] for $T > 500$ K. Next, we plot the detailed temperature dependence of the yield strength corresponding to the hardest and softest directions –as given by Fig. 6.6a– for this strain rate in Figure 6.7. As the calculated data show, there is approximately a 30% difference in yield stress between the hardest and softest directions. Interestingly, this gap appears to be fairly independent of temperature. Above 650 K, the curves begin to level off, signaling the onset of the athermal regime.

6.3.3.2 Dependence on strain rate and strain rate sensitivity

In this Section we expand the analysis presented in the previous Section to strain rates of 10^{-4} and 10^{-5} s⁻¹. To avoid redundancies, here we show only the temperature trajectory of the softest and hardest loading orientations in Figs. 6.6b and 6.6c, which emanate from calculations as those presented in Fig. 6.5. The results are quantitative similar to the case of $\dot{\varepsilon} = 10^{-3}$, with the only appreciable deviations occurring at temperatures above 450 K. At these high temperatures, the softest orientation rotates clearly towards the vicinity of the [113] zonal axis, without excursions near [103] as was the case for the $\dot{\varepsilon} = 10^{-3}$ calculations.

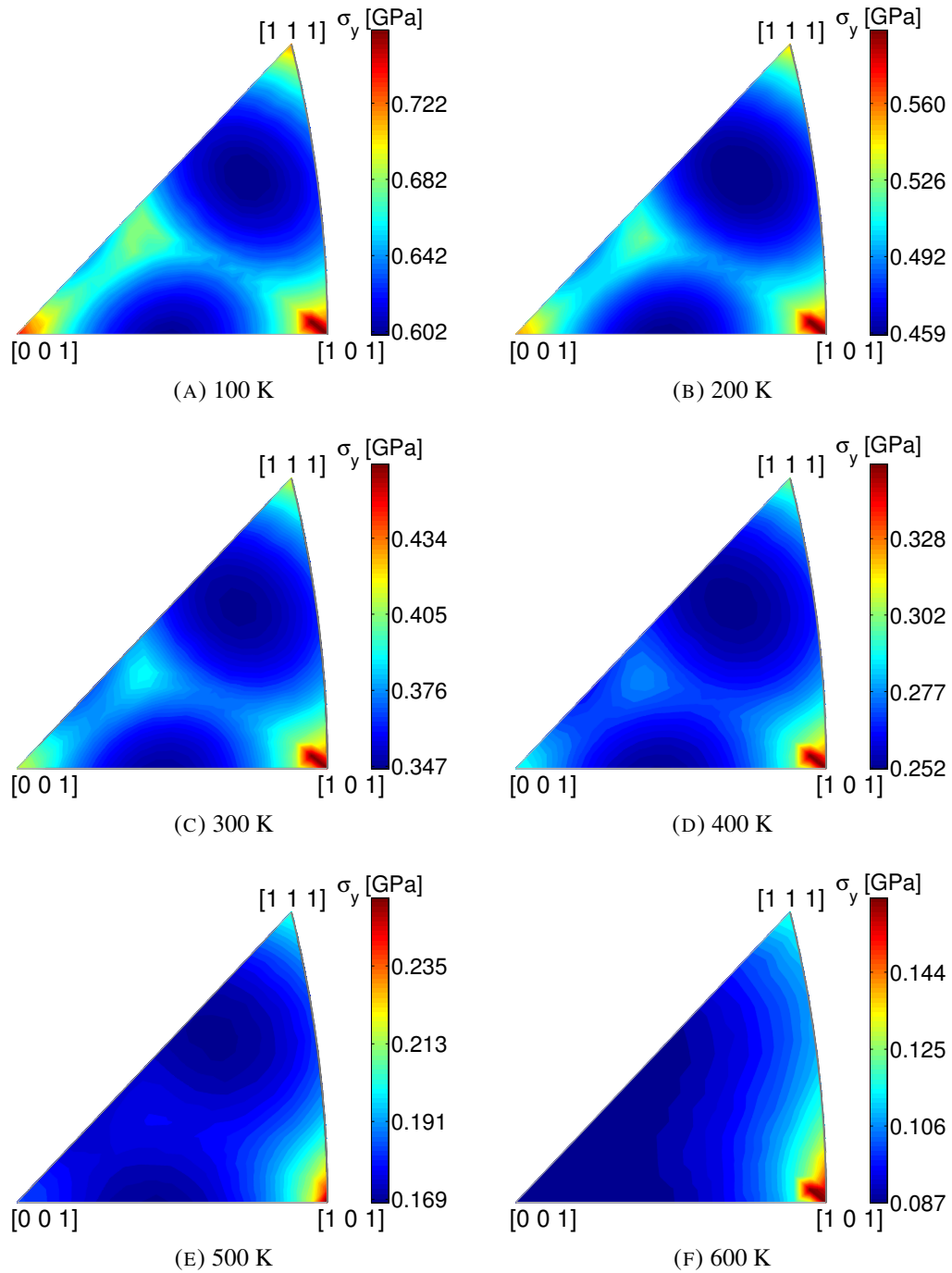


FIGURE 6.5: Contour maps of the yield strength from uniaxial tensile test simulations for 231 uniformly distributed crystallographic orientations in the standard triangle at different temperatures. Note that each map has its own distinct numerical scale to aid in the visualization of hard and soft regions.

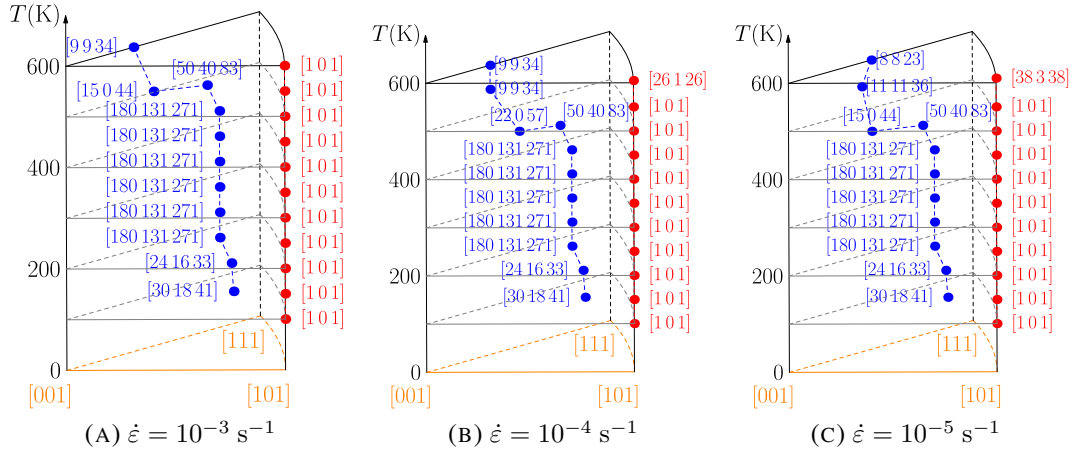


FIGURE 6.6: Temperature path of the softest and hardest yield directions on the standard triangle as a function of strain rate.

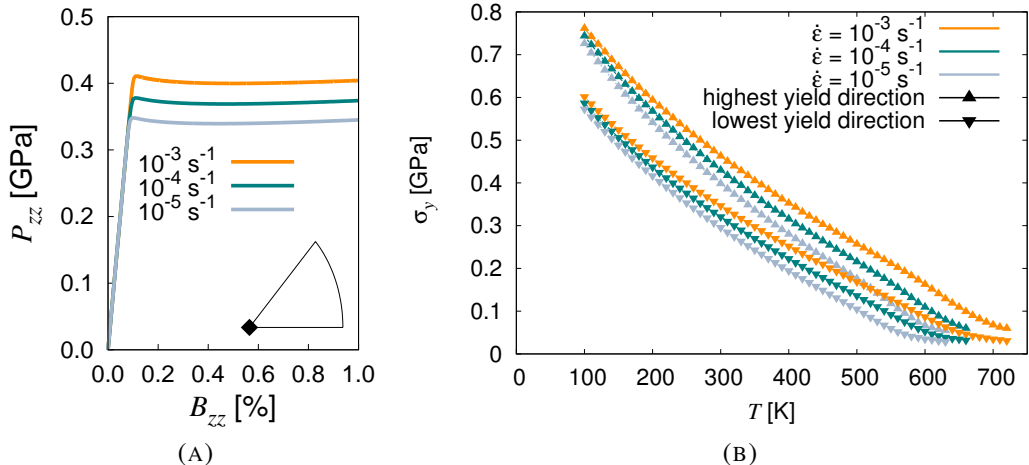


FIGURE 6.7: (a) Stress-strain relations at three different strain rates and $T = 300$ K for a [101] loading orientation. (b) Temperature dependence of the yield strength for the softest and hardest directions as a function of strain rate.

As above, we add the temperature dependence of the yield stress for the hardest and softest directions at these strain rates to Figure 6.7. The data show the same qualitative trend for all strain rates, with the same approximate 30% difference between the hard and soft orientations. However, useful information can be extracted if the strain-rate dependence of the yield stress is plotted for selected orientations. Then, one can calculate the degree of *strain rate sensitivity*, characterized by the strain rate sensitivity exponent m , of the material as a function of temperature. Strain rate sensitivity is exceedingly important to delay the onset of inhomogeneous deformation (Hutchinson & Neale, 1977), e.g. necking, and is used as a criterion to assess the possibility of superplastic behavior in certain kinds of materials (Arieli & Rosen, 1976; Hedworth & Stowell, 1971). This

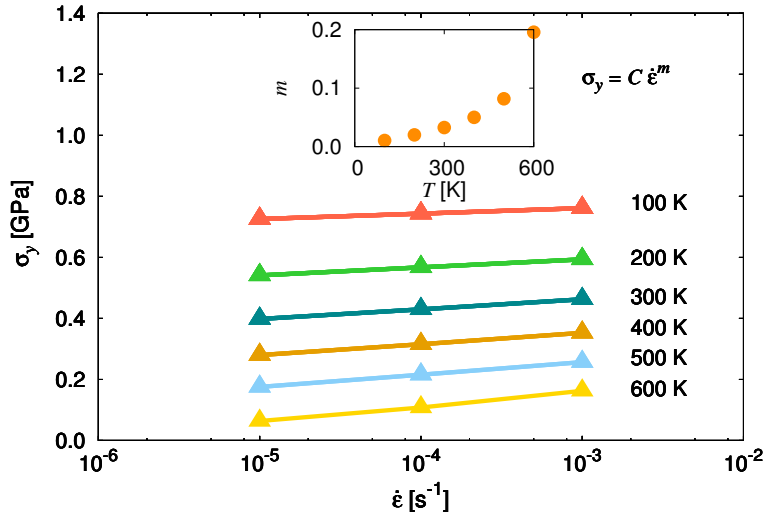


FIGURE 6.8: Dependence of yield strength with strain rate for loading along direction [1 0 1] as a function of temperature. The inset represents the dependence of the strain rate sensitivity exponent m with temperature.

belongs more in the realm of failure and is thus outside the scope of this paper. However, it is of interest to calculate the strain rate sensitivity of the yield stress and relate our findings to the larger failure picture if possible.

This precisely what is done in Figure 6.8 for [101] loading tests. The figure shows the variation of the yield strength at the three strain rates considered here, again in the range $100 < T < 600$ K. The data can then be fitted to the following expression:

$$\sigma_y = C \dot{\varepsilon}^m \quad (6.6)$$

where C is a fitting constant. The strain rate sensitivity exponent is formally defined as:

$$m = \frac{\partial \log \sigma}{\partial \log \dot{\varepsilon}} \quad (6.7)$$

m is plotted in the inset to Fig. 6.8, where it can be seen that it increases monotonically with temperature from a value of $m = 0.01$ at 100 K to ≈ 0.2 at 600 K.

6.3.4 Biaxial loading tests and yield surfaces

For non-associated CP formulations such as the present one, yielding is not a separate and independent criterion, but a consequence of the constitutive law of the material behavior (Bodner, 1968). Even then, a sufficiently low rates the resulting stress-strain

curves may resemble those of materials with predefined yield stresses ([Lubliner, 2008](#)). In fact, with yield based on the identification criterion introduced in Section 6.3.1, yield surfaces can be *predicted* as an outcome of the CP calculations. In this Section we calculate the yield curves under biaxial stress conditions for selected orthogonal loading directions \mathbf{l}_y and \mathbf{l}_z . As noted in Chapter 4, the present implementation of the non-Schmid stress projection law is only valid for tensile conditions². Thus, our yield curves are only meaningful in the positive stress quadrant (or octant, for yield surfaces). The procedure to calculate each point of the yield surface consists of deforming the system simultaneously along the prescribed orientations until the material yields according to criterion (6.5). The stresses P_{zz} and P_{yy} are then measured along both directions and the resulting duple is added to the curve. Plain stress conditions are adopted along the remaining direction, *i.e.* $\sigma_{xx} = 0$. All the calculations are done at a nominal strain rate of $\dot{\varepsilon} = 10^{-4} \text{ s}^{-1}$.

First we calculate the yield curve for $\mathbf{l}_y = [111]$ and $\mathbf{l}_z = [11\bar{2}]$ as a function of temperature. Results are shown in Figure 6.9. The curves enclose domains that are everywhere convex, thus satisfying the *Drucker-Prager* criterion for stable plastic flow materials ([Drucker et al., 1952](#); [Prager, 1952](#)). The absolute values and the temperature sensitivity of the yield stresses for the end cases of $P_{zz} = 0$ and $P_{yy} = 0$ are consistent with the results shown in Section 6.3.3 for the \mathbf{l}_y and \mathbf{l}_z chosen here.

The next series of calculations involves determining the entire yield surface of the [111] zone, *i.e.* for a set of directions orthogonal to [111] in 10° intervals, at a fixed temperature of 300 K. Symmetry considerations limit the angular range to be explored to a 60° arc, which is shown in the figure. Yield surfaces such as this one are the culmination of crystal plasticity calculations, and can be used as constitutive input into continuum models to simulate mechanical treatments and processes, as well as for component design at the engineering scale.

²Although this is not a limitation in a strict sense as it is done simply for consistency with non-Schmid treatments.

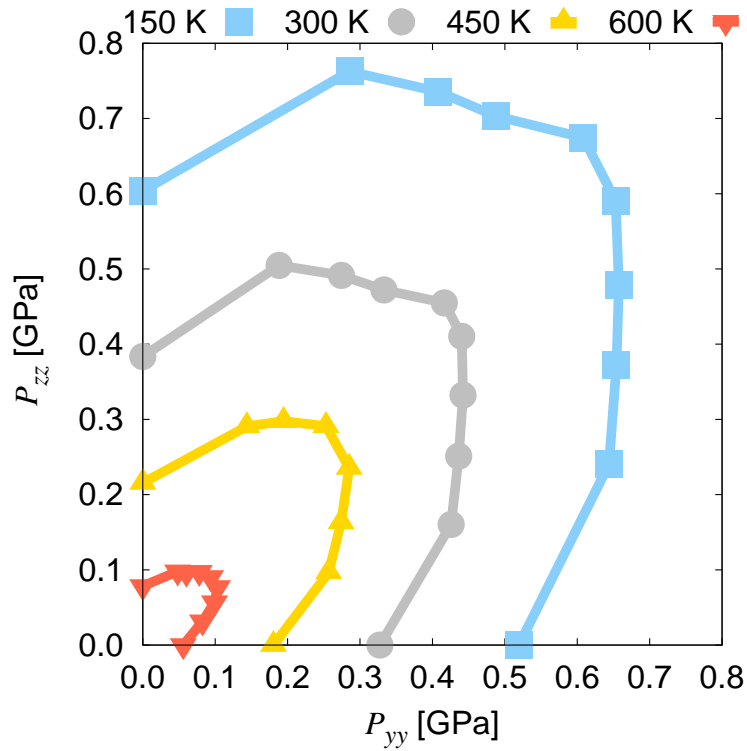


FIGURE 6.9: Yield curve for loading along directions $l_y = [111]$ and $l_z = [11\bar{2}]$ as a function of temperature.

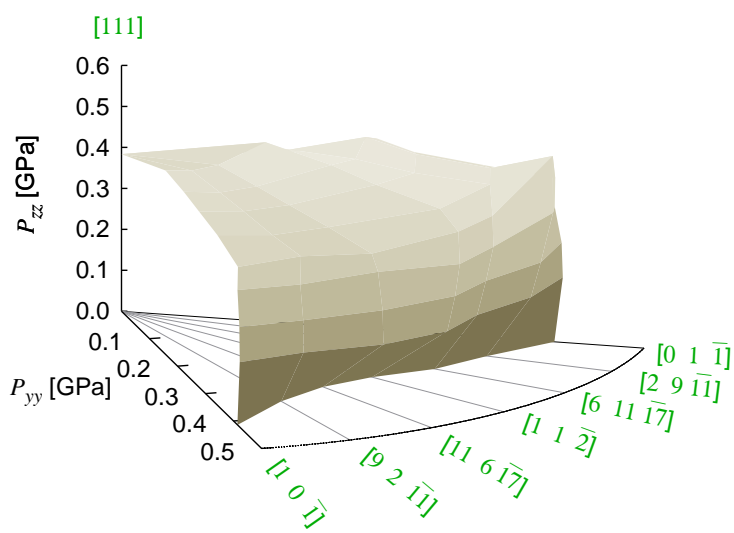


FIGURE 6.10: Yield surface at 300 K for biaxial loading along directions belonging to the $[111]$ zone. By symmetry, only the 60° -arc need be explored.

6.4 Summary

To summarize, the main findings of this chapter can be condensed into the following aspects:

- The main contribution of this chapter is the development of a crystal plasticity model parameterized solely to first-principles atomistic calculations that captures the uniqueness of bcc plastic flow. The model admits only dislocation slip as the operating deformation mechanism and includes the special characteristics of screw dislocation slip via suitably-constructed dislocation mobility functions and projection operators that capture anomalous slip according to state-of-the-art non-Schmid formulations. All model and material parameters are obtained using dedicated molecular statics calculations utilizing selected semiempirical interatomic potentials for tungsten.
- The fully-parameterized technique is validated with experimental uniaxial tensile test data with excellent agreement found for the temperature dependence of the yield stress under several loading orientations.
- After validation with experiments, the model is applied to calculate the yield strength of tungsten for 231 orientations within the standard triangle as a function of temperature and strain rate.
- The strain-rate sensitivity exponent is also calculated in the 10^{-5} -to- 10^{-3} s $^{-1}$ range and find once more very good agreement with experimental results.
- Finally, the validated model is employed to predict yield surfaces for tungsten that can be used in macroscopic deformation models.

Part III

CONCLUSIONS

Chapter 7

Conclusions

7.1 Conclusions of Part I

Part I of the dissertation describes the modeling of the plastic behavior in tungsten at the atomistic scale. At this level, the low mobility and non-planar core structure of screw dislocations with Burgers vector $\mathbf{b} = 1/2 \langle 111 \rangle$ usually make them the main carriers of plasticity in bcc metals like tungsten.

In Chapter 2 five different interatomic potentials (three EAM, one BOP and one MEAM) are compared and assessed by their performance in terms of static and dynamic screw dislocation properties. The dynamic behavior is evaluated in terms of screw dislocation mobility as a function of stress and temperature. Simple 'ramps' as short as 10 ps or 20 ps have been seen to reduce stress oscillations to a level that requires nearly 200 ps to reach when stress is applied as a sudden step. Applying these stress 'ramps' increases considerably the computational efficiency of the simulations that characterize the dynamic behavior of dislocations. Screw dislocation mobilities have been calculated for all potentials on a $\{112\}$ glide plane. The results obtained provide elements to judge the EAM ([Marinica et al., 2013](#)) and MEAM ([Park et al., 2012](#)) as the most suitable interatomic potentials for dislocation calculations. The temperature-induced dislocation core transformation –from compact to dissociated– has been observed for one of the potentials tested. It is not possible to confirm whether this corresponds to a real physical phenomenon or is an artifact, but the transformation is indeed seen to impact the dynamic properties of dislocations. The analysis of the five interatomic potentials suggests, first, that the atomistic nature of the dislocation core governs behavior at larger

scales and, second, a purely static treatment of the dislocation core is insufficient to predict and describe the dynamics of dislocations. Unfortunately, one of the most important difficulties associated with such dynamic studies is the scale-dependent nature of MD simulations, which require exceedingly high strain rates to drive the system over time scales accessible computationally, of the order of a few tens of ns. Because of these limitations, MD is incapable at present of properly capturing the thermally-activated motion of screw dislocations at low stresses. However, MD simulations can still provide valuable input in intermediate-to-high stress conditions and in situations where the deformation rates are high.

In Chapter 3 the enthalpy and energy barriers of single screw dislocations and kink-pair dislocations are studied. For reasons of computational efficiency, all calculations in this chapter are performed with the EAM potential ([Marinica et al., 2013](#)). As a preliminary step, the Peierls potential is calculated on a {110} and a {112} plane to ascertain whether direct glide on {112} type planes is a feasible phenomenon. This is done using the nudged-elastic band (NEB) method applied to a single screw dislocation in suitably constructed computational cells. It is shown that elementary glide on a {112} plane is a composite of two elementary steps on alternate {110} planes. Judging by these results, it is concluded that glide on any given plane is achieved by way of sequential {110} jumps. To compute the kink-pair enthalpy, a direct atomistic approach is taken by treating kink-pair configurations as activated states of long straight dislocation lines moving along the Peierls trajectory. NEB calculations are performed on screw dislocation lines of 100b in length going from one Peierls valley to the next as a function of stress. To break the translational symmetry along the $1/2 \langle 111 \rangle$ direction, intermediate replicas are created and seeded with kink-pair configurations. Then the maximum total energy is calculated along the NEB path and the kink separation at the activated state is also measured. The final trajectory is obtained as the lowest-energy superposition between the NEB energy path and the Peierls energy for the straight screw dislocation. The activated state is chosen as the maximum energy point along the relaxed final path. Kink-pair activation enthalpy and kink-pair width are evaluated as a function of stress. The stress-dependent formation enthalpy of a kink-pair is fitted to the standard Kocks–Argon–Ashby expression that equals the energy of a pair of isolated kinks at zero stress and vanishes at the Peierls stress.

In Chapter 4 the breakdown of Schmid’s law characteristic in bcc metals is studied using the EAM interatomic potential for tungsten ([Marinica et al., 2013](#)). NEB calculations of

single screw dislocation lines are performed to include non-Schmid effects in the formulation of the resolved shear stress (RSS) when a combination of shear stresses and non glide stresses are applied on different maximum resolved shear stress planes (MRSSP). Both twinning-antitwinning asymmetry (T/AT) and non glide stresses are considered. The critical resolved shear stress (CRSS) is calculated as a function of (i) the angle χ between the primary glide plane and the MRSSP and (ii) the non glide stress σ . This dependence of CRSS with χ and σ is initially fitted used the standard procedure to capture the non-Schmid effects suggested by Vitek and co-workers ([Gröger et al., 2008a,b](#)). In addition to this procedure, which only takes into account the lineal dependence of the CRSS with the non glide stress, two additional approaches are presented. First, the contribution of the non glide stresses is computed using a parabolic dependence of CRSS with the non glide stress σ . Second, a multiparametric fitting surface with no contrains that captures the dependence of CRSS with χ and σ simultaneously is suggested.

7.2 Conclusions of Part II

Part II of the dissertation describes the modeling of the plastic behavior in single crystal tungsten at the continuum-level scale. Crystal Plasticity (CP) simulations are performed using two different approaches, depending on the origin of the dislocation mobility function and non-Schmid effects.

In Chapter 5 the main source of constitutive information in the formulation of the CP model comes from the dislocation mobility functions obtained via kinetic Monte Carlo (kMC) simulations ([Stukowski et al., 2015](#)). The kMC model that simulates the motion of dislocations in their thermally-activated regime has been fully parameterized using the atomistic calculations described in Part I and it includes the T-AT asymmetry of non-Schmid effects. Dislocation mobility functions depends on the temperature, applied stress and activated slip systems. The results obtained when activating only $\langle 111 \rangle\{110\}$ slip systems and a combination of both $\langle 111 \rangle\{110\}$ and $\langle 111 \rangle\{112\}$ slip systems confirm that slip of screw dislocations takes place primarily on $\{110\}$ planes, as it was already suggested by the atomistic calculations from Chapter 3. The uniaxial tensile tests simulated along 231 uniformly-distributed crystallographic orientations in the standard triangle reveal that yield strength decreases very fast with temperature and it also depends strongly on the loading orientation of the tensile test.

In Chapter 6 the main source of constitutive information in the CP model comes from a dislocation mobility function formulated analytically. This novel mobility function is based on two assumptions: first, the total time needed to move a screw dislocation line from one Peierls valley to the next one can be defined by the contribution of the time of nucleation required to nucleate kink pair and the time of propagation required to expand the kink pair; second, a kink-pair propagates before a new kink-pair is nucleated. These two assumptions are known to be true for the temperature range studied here (up to 700 K). The formulation of the RSS in the CP model includes the contribution of non-Schmid effects calculated in Chapter 4. Only $\{1\bar{1}0\}$ planes are considered active during slip. The predictions of the model, fully parameterized with atomistic calculations, are compared with experimental uniaxial tests and the agreement is very accurate for the entire temperature range when both T/AT and non glide stresses are included. Material point simulations are performed and the yield strength in single crystal tungsten is computed under different uniaxial crystallographic loading orientations in the standard triangle, different temperatures and strain rates. The main conclusions of these material point simulations are that yield strength decreases rapidly with temperature and moderately with strain rate. Moreover, the loading orientation of minimum yield strength at each temperature depends on the temperature of the sample while the loading orientations of maximum yield strength are always around the $[1\bar{1}0]$ corner of the standard triangle for the entire temperature range.

Chapter 8

Publications and research activities

Publications

2015

- David Cereceda, Martin Diehl, Franz Roters, Dierk Raabe, J. M. Perlado and Jaime Marian. "Unraveling the temperature dependence of the yield strength in single crystal tungsten using atomistically-informed Crystal Plasticity simulations". *Under review*.
- David Cereceda, Martin Diehl, Franz Roters, Pratheek Shanthraj, Dierk Raabe, J. M. Perlado and Jaime Marian. "Linking atomistic, kinetic Monte Carlo and crystal plasticity simulations of single-crystal Tungsten strength". *Under review*.
- Alexander Stukowski, David Cereceda, Thomas D. Swinburne, and Jaime Marian. "Thermally-activated non-Schmid glide of screw dislocations in W using atomistically-informed kinetic Monte Carlo simulations". *International Journal of Plasticity* 65 (2015): 108-130.

2013

- David Cereceda, A. Stukowski, M. R. Gilbert, Sylvain Queyreau, Lisa Ventelon, M. C. Marinica, J. M. Perlado, and J. Marian. "Assessment of interatomic potentials for atomistic analysis of static and dynamic properties of screw dislocations in W". *Journal of Physics: Condensed Matter* 25, no. 8 (2013): 085702.

2012

- David Cereceda, J. Manuel Perlado, and Jaime Marian. "Techniques to accelerate convergence of stress-controlled molecular dynamics simulations of dislocation motion". Computational Materials Science 62 (2012): 272-275.
- Perlado, J. M., J. Alvarez, D. Garoz, R. Gonzalez-Arrabal, N. Gordillo, C. Guerrero, O. Pena et al. "Approach to Power Plant Physics and Technology in Laser Fusion Energy Systems under Repetitive Operation". LIFE 4 (2012): 5.

2011

- Perlado, J. M., J. Sanz, J. Alvarez, D. Cereceda, S. Cuesta, Sergio Courtin, E. Del Rio et al. "IFE Plant Technology Overview and contribution to HiPER proposal". In SPIE Optics+ Optoelectronics, pp. 80801Z-80801Z. International Society for Optics and Photonics, 2011.

Conferences and workshops

2015

- **USNCCM13.** 13th U.S. National Congress on Computational Mechanics. San Diego, United States. Title: "Multiscale model of strength in single crystal tungsten under uniaxial and biaxial loading". *Oral presentation*.
- **ICSMA-17.** 17th International Conference on the Strength of Materials. Brno, Czech Republic. Title: "Multiscale model of strength in single crystal tungsten under uniaxial and biaxial loading". *Oral presentation*.
- **PANACM 2015.** 1st Pan-American Congress on Computational Mechanics. Buenos Aires, Argentina. Title: "Multiscale model of strength in single crystal tungsten under uniaxial and biaxial loading". *Oral presentation*.
- **TMS 2015.** The Minerals, Metals and Materials Society meeting, Orlando, United States. Title: "Multiscale model of strength in single crystal tungsten under uniaxial and biaxial loading". *Oral presentation*.

2014

- **MMM 2014.** 7th International Conference on Multiscale Materials Modeling. Berkeley, California. Title: "Linking atomistic, kinetic Monte Carlo and crystal plasticity simulations of single-crystal Tungsten strength". *Oral presentation.*

2013

- **Tungsten for Nuclear Applications.** Oxford, UK. Title: "Energetics of thermally activated screw dislocation motion in Tungsten using atomistic simulations". *Poster presentation.*
- **SOFE 2013.** 25th Symposium on Fusion Engineering. San Francisco, United States. Title: "Parameterization of Kinetic Monte Carlo simulations of dislocation motion in Tungsten". *Poster presentation.*

2012

- **TOFE 2012.** ANS 20th Topical Meeting on the Technology of Fusion Energy. Title: "Power Plant Physics and Technology in HiPER IFE Project under Repetitive Operation". *Oral presentation.*
- **2nd HiPER Fellow Meeting.** Bourdeaux, France. Title: "A study of Screw Dislocation Mobilities in Tungsten obtained by Molecular Dynamics Simulation". *Poster presentation.*

2011

- **ICENES 2011.** 15th International Conference on Emerging Nuclear Energy Systems. Title: "Molecular Dynamics Simulations of Screw Dislocation Mobility in Tungsten". *Poster presentation. 2nd Prize Best Student Poster.*

Courses

2013

- **Modeling Materials Short Course.** Argonne National Laboratory, United States.

2012

- **Hermes 2012 Summer School on Materials Modelling.** Imperial College London, UK.

- **Formación Inicial del Profesorado en el Marco del Espacio Europeo de Educación Superior (18 ECTS). ICE UPM, Madrid.**

2011

- **5th Karlsruhe International School on Fusion Technologies.** *Karlsruhe Institute of Technology, Germany.*

Stays abroad

2015

- **University of California Los Angeles,** United States.

Duration: 2 months (January - February)

Supervisor: Prof. Jaime Marian.

Support: CONVOCATORIA DE ESTANCIAS BREVES DE LA UPM PARA LOS BENEFICIARIOS DE PROGRAMAS PREDOCTORALES.

2014

- **Lawrence Livermore National Laboratory,** United States.

Duration: 6 months (April - October).

Supervisor: Dr. Jaime Marian.

Support: XII CONVOCATORIA DE AYUDAS DEL CONSEJO SOCIAL PARA EL FOMENTO DE LA FORMACIÓN Y LA INTERNACIONALIZACIÓN DE DOCTORANDOS PARA EL CURSO 2014-2015.

- **Lawrence Livermore National Laboratory,** United States.

Duration: 3 months (January - April).

Supervisor: Dr. Jaime Marian.

Support: CONVOCATORIA DE ESTANCIAS BREVES DE LA UPM PARA LOS BENEFICIARIOS DE PROGRAMAS PREDOCTORALES.

2013

- **Lawrence Livermore National Laboratory, United States.**

Duration: 6 months (March - September).

Supervisor: Dr. Jaime Marian.

Support: XI CONVOCATORIA DE AYUDAS DEL CONSEJO SOCIAL PARA
EL FOMENTO DE LA FORMACIÓN Y LA INTERNACIONALIZACIÓN
DE DOCTORANDOS PARA EL CURSO 2013-2014.

Bibliography

- Ackermann, F., Mughrabi, H., & Seeger, A. (1983). Temperature-and strain-rate dependence of the flow stress of ultrapure niobium single crystals in cyclic deformation. *Acta metallurgica*, 31, 1353–1366.
- Ackland, G., & Thetford, R. (1987). An improved n-body semi-empirical model for body-centred cubic transition metals. *Philosophical Magazine A*, 56, 15–30.
- Alankar, A., Field, D., & Zbib, H. (2012). Explicit incorporation of cross-slip in a dislocation density-based crystal plasticity model. *Philosophical Magazine*, 92, 3084–3100.
- Alankar, A., Field, D. P., & Raabe, D. (2014). Plastic anisotropy of electro-deposited pure α -iron with sharp crystallographic // texture in normal direction: Analysis by an explicitly dislocation-based crystal plasticity model. *International Journal of Plasticity*, 52, 18 – 32. In Honor of Hussein Zbib.
- Argon, A., & Maloof, S. (1966a). Plastic deformation of tungsten single crystals at low temperatures. *Acta metallurgica*, 14, 1449–1462.
- Argon, A., & Maloof, S. (1966b). Plastic deformation of tungsten single crystals at low temperatures. *Acta metallurgica*, 14, 1449–1462.
- Arieli, A., & Rosen, A. (1976). Measurements of the strain rate sensitivity coefficient in superplastic ti? 6al? 4v alloy. *Scripta Metallurgica*, 10, 471–475.
- Arsenlis, A., & Parks, D. (1999). Crystallographic aspects of geometrically-necessary and statistically-stored dislocation density. *Acta Materialia*, 47, 1597 – 1611.
- Arsenlis, A., & Parks, D. M. (2002). Modeling the evolution of crystallographic dislocation density in crystal plasticity. *Journal of the Mechanics and Physics of Solids*, 50, 1979 – 2009.

- Arsenlis, A., Parks, D. M., Becker, R., & Bulatov, V. V. (2004). On the evolution of crystallographic dislocation density in non-homogeneously deforming crystals. *Journal of the Mechanics and Physics of Solids*, 52, 1213 – 1246.
- Barrett, C. S., & Massalski, T. B. (1966). *Structure of metals* volume 631. McGraw-Hill New York.
- Bishop, J., & Hill, R. (1951a). A theoretical derivation of the plastic properties of a polycrystalline face-centred metal. *The London, Edinburgh, and Dublin Philosophical Magazine and Journal of Science*, 42, 1298–1307.
- Bishop, J., & Hill, R. (1951b). A theory of the plastic distortion of a polycrystalline aggregate under combined stresses. *The London, Edinburgh, and Dublin Philosophical Magazine and Journal of Science*, 42, 414–427.
- Bodner, S. (1968). *Constitutive equations for dynamic material behavior*. Springer.
- Bolt, H., Barabash, V., Federici, G., Linke, J., Loarte, A., Roth, J., & Sato, K. (2002). Plasma facing and high heat flux materials–needs for iter and beyond. *Journal of Nuclear Materials*, 307, 43–52.
- Bolt, H., Barabash, V., Krauss, W., Linke, J., Neu, R., Suzuki, S., Yoshida, N., & Team, A. U. (2004). Materials for the plasma-facing components of fusion reactors. *Journal of nuclear materials*, 329, 66–73.
- Born, M. (1927). Born-oppenheimer approximation. *Quantum*, 2, 4.
- Bowden, P., & Jukes, J. (1972). The plastic flow of isotropic polymers. *Journal of Materials Science*, 7, 52–63.
- Brinckmann, S., Kim, J.-Y., & Greer, J. R. (2008). Fundamental differences in mechanical behavior between two types of crystals at the nanoscale. *Physical review letters*, 100, 155502.
- Brünig, M. (1997). Numerical modelling of finite elastic-plastic deformations of crystalline solids including non-schmid effects. In *Computational plasticity* (pp. 907–912). volume 5.
- Brunner, D. (2000). Comparison of flow-stress measurements on high-purity tungsten single crystals with the kink-pair theory. *Materials Transactions, JIM(Japan)*, 41, 152–160.

- Brunner, D. (2000). Comparison of flow-stress measurements on high-purity tungsten single crystals with the kink-pair theory. *Materials Transactions JIM*, 41, 152–160.
- Brunner, D. (2010). Temperature dependence of the plastic flow of high-purity tungsten single crystals: Dedicated to professor dr. dr. hc alfred seeger on the occasion of his birthday. *International Journal of Materials Research*, 101, 1003–1013.
- Brunner, D., & Diehl, J. (1991). Strain-rate and temperature dependence of the tensile flow stress of high-purity α -iron above 250 k (regime i) studied by means of stress-relaxation tests. *Physica Status Solidi (A) Applied Research*, 124, 155–170.
- Bulatov, V., & Cai, W. (2006). *Computer simulations of dislocations* volume 3. Oxford University Press.
- Bulatov, V., Richmond, O., & Glazov, M. (1999). An atomistic dislocation mechanism of pressure-dependent plastic flow in aluminum. *Acta materialia*, 47, 3507–3514.
- Cai, W., Bulatov, V. V., Chang, J., Li, J., & Yip, S. (2004a). Dislocation core effects on mobility. *Dislocations in solids*, 12, 1–80.
- Cai, W., Bulatov, V. V., Chang, J., Li, J., Yip, S., Nabarro, F., & Hirth, J. (2004b). *Dislocation core effects on mobility in: Dislocations in Solids* volume 64. Elsevier.
- Cai, W., Bulatov, V. V., Justo, J. F., Argon, A. S., & Yip, S. (2002). Kinetic monte carlo approach to modeling dislocation mobility. *Computational materials science*, 23, 124–130.
- Caillard, D. (2010a). Kinetics of dislocations in pure fe. part i. in situ straining experiments at room temperature. *Acta Materialia*, 58, 3493–3503.
- Caillard, D. (2010b). Kinetics of dislocations in pure fe. part ii. in situ straining experiments at low temperature. *Acta Materialia*, 58, 3504–3515.
- Callister, W., & Rethwisch, D. (2009). *Materials Science and Engineering: An Introduction*. John Wiley & Sons Canada, Limited.
- Cereceda, D., Stukowski, A., Gilbert, M., Queyreau, S., Ventelon, L., Marinica, M., Perlado, J., & Marian, J. (2013). Assessment of interatomic potentials for atomistic analysis of static and dynamic properties of screw dislocations in w. *Journal of Physics: Condensed Matter*, 25, 085702.
- Chang, J., Cai, W., Bulatov, V. V., & Yip, S. (2001). Dislocation motion in bcc metals by molecular dynamics. *Materials Science and Engineering: A*, 309, 160–163.

- Chaussidon, J., Fivel, M., & Rodney, D. (2006). The glide of screw dislocations in bcc fe: Atomistic static and dynamic simulations. *Acta materialia*, 54, 3407–3416.
- Cheong, K.-S., & Busso, E. P. (2004). Discrete dislocation density modelling of single phase {FCC} polycrystal aggregates. *Acta Materialia*, 52, 5665 – 5675.
- Christensen, R. M. (2008). Observations on the definition of yield stress. *Acta Mechanica*, 196, 239–244.
- Christian, J. (1983). Some surprising features of the plastic deformation of body-centered cubic metals and alloys. *Metallurgical Transactions A*, 14, 1237–1256.
- Dao, M., & Asaro, R. (1993). Non-schmid effects and localized plastic flow in intermetallic alloys. *Materials Science and Engineering: A*, 170, 143–160.
- Deo, C., & Srolovitz, D. J. (2002). First passage time markov chain analysis of rare events for kinetic monte carlo: double kink nucleation during dislocation glide. *Modelling and Simulation in Materials Science and Engineering*, 10, 581.
- Deo, C. S., Srolovitz, D. J., Cai, W., & Bulatov, V. V. (2005). Kinetic monte carlo method for dislocation migration in the presence of solute. *Phys. Rev. B*, 71, 014106.
- Dezerald, L., Proville, L., Ventelon, L., Willaime, F., & Rodney, D. (2015). First-principles prediction of kink-pair activation enthalpy on screw dislocations in bcc transition metals: V, nb, ta, mo, w, and fe. *Physical Review B*, 91, 094105.
- Dezerald, L., Ventelon, L., Clouet, E., Denoual, C., Rodney, D., & Willaime, F. (2014). Ab initio modeling of the two-dimensional energy landscape of screw dislocations in bcc transition metals. *Physical Review B*, 89, 024104.
- Dorn, J. E., & Rajnak, S. (1964). Nucleation of kink pairs and the peierls' mechanism of plastic deformation. *Trans. Aime*, 230, 1052–1064.
- Drucker, D., Prager, W., & Greenberg, H. (1952). Extended limit design theorems for continuous media, .
- Duesbery, M. (1969). The influence of core structure on dislocation mobility. *Philosophical Magazine*, 19, 501–526.
- Duesbery, M., & Foxall, R. (1969). A detailed study of the deformation of high purity niobium single crystals. *Philosophical Magazine*, 20, 719–751.

- Duesbery, M. a.-S., & Vitek, V. (1998). Plastic anisotropy in bcc transition metals. *Acta Materialia*, 46, 1481–1492.
- Eisenlohr, P., Diehl, M., Lebensohn, R., & Roters, F. (2013). A spectral method solution to crystal elasto-viscoplasticity at finite strains. *International Journal of Plasticity*, 46, 37 – 53. Microstructure-based Models of Plastic Deformation.
- Erieau, P., & Rey, C. (2004). Modeling of deformation and rotation bands and of deformation induced grain boundaries in if steel aggregate during large plane strain compression. *International Journal of Plasticity*, 20, 1763–1788.
- Escaig, B. (1968). *Le Journal de Physique Colloques*, 29.
- Escaig, B. (1974). Dissociation and mechanical properties. dislocation splitting and the plastic glide process in crystals. *Le Journal de Physique Colloques*, 35, C7–151.
- Faken, D., & Jónsson, H. (1994). Systematic analysis of local atomic structure combined with 3d computer graphics. *Computational Materials Science*, 2, 279 – 286.
- Fikar, J., Schäublin, R., & Björkas, C. (2009). Atomistic simulation of $1/2\lvert 111\rvert$ screw dislocations in bcc tungsten. *Advanced Materials Research*, 59, 247–252.
- Finnis, M., & Sinclair, J. (1984). A simple empirical n-body potential for transition metals. *Philosophical Magazine A*, 50, 45–55.
- Franciosi, P., Le, L., Monnet, G., Kahloun, C., & Chavanne, M.-H. (2015). Investigation of slip system activity in iron at room temperature by sem and afm in-situ tensile and compression tests of iron single crystals. *International Journal of Plasticity*, 65, 226–249.
- Frank, F., & van der Merwe, J. H. (1949). One-dimensional dislocations. i. static theory. *Proceedings of the Royal Society of London. Series A. Mathematical and Physical Sciences*, 198, 205–216.
- Frenkel, D., & Smit, B. (2001). *Understanding molecular simulation: from algorithms to applications* volume 1. Academic press.
- Frenkel, J. (1926). Zur theorie der elastizitätsgrenze und der festigkeit kristallinischer körper. *Zeitschrift für Physik*, 37, 572–609.
- Giannattasio, A., Tanaka, M., Joseph, T., & Roberts, S. (2007). An empirical correlation between temperature and activation energy for brittle-to-ductile transitions in single-phase materials. *Physica Scripta*, 2007, 87.

- Gilbert, M., Queyreau, S., & Marian, J. (2011). Stress and temperature dependence of screw dislocation mobility in α -fe by molecular dynamics. *Physical Review B*, 84, 174103.
- Gilbert, M. R., & Dudarev, S. L. (2010). Ab initio multi-string frenkel–kontorova model for ab= $a/2 [111]$ screw dislocation in bcc iron. *Philosophical Magazine*, 90, 1035–1061.
- Gordon, P., Neeraj, T., Li, Y., & Li, J. (2010). Screw dislocation mobility in bcc metals: the role of the compact core on double-kink nucleation. *Modelling and Simulation in Materials Science and Engineering*, 18, 085008.
- Gröger, R., Bailey, A., & Vitek, V. (2008a). Multiscale modeling of plastic deformation of molybdenum and tungsten: I. atomistic studies of the core structure and glide of $1/2 \langle 111 \rangle$ screw dislocations at 0k. *Acta Materialia*, 56, 5401–5411.
- Gröger, R., Racherla, V., Bassani, J., & Vitek, V. (2008b). Multiscale modeling of plastic deformation of molybdenum and tungsten: II. yield criterion for single crystals based on atomistic studies of glide of $1/2 \langle 111 \rangle$ screw dislocations. *Acta Materialia*, 56, 5412–5425.
- Gröger, R., & Vitek, V. (2005). Breakdown of the schmid law in bcc molybdenum related to the effect of shear stress perpendicular to the slip direction. In *Materials Science Forum* (pp. 123–126). Trans Tech Publ volume 482.
- Gröger, R., & Vitek, V. (2012). Constrained nudged elastic band calculation of the peierls barrier with atomic relaxations. *Modelling and Simulation in Materials Science and Engineering*, 20, 035019.
- Gumbsch, P., & Gao, H. (1999). Dislocations faster than the speed of sound. *Science*, 283, 965–968.
- Hamelin, C., Diak, B., & Pilkey, A. (2011). Multiscale modelling of the induced plastic anisotropy in bcc metals. *International Journal of Plasticity*, 27, 1185–1202.
- Hartmaier, A., & Gumbsch, P. (2005a). Thermal activation of crack-tip plasticity: The brittle or ductile response of a stationary crack loaded to failure. *Phys. Rev. B*, 71, 024108.
- Hartmaier, A., & Gumbsch, P. (2005b). Thermal activation of crack-tip plasticity: The brittle or ductile response of a stationary crack loaded to failure. *Physical Review B*, 71, 024108.

- Hedworth, J., & Stowell, M. (1971). The measurement of strain-rate sensitivity in superplastic alloys. *Journal of Materials Science*, 6, 1061–1069.
- Henkelman, G., & Jonsson, H. (2000). Improved tangent estimate in the nudged elastic band method for finding minimum energy paths and saddle points. *Journal Of Chemical Physics*, 113, 9978–9985.
- Henkelman, G., & Jónsson, H. (2001). Long time scale kinetic monte carlo simulations without lattice approximation and predefined event table. *The Journal of Chemical Physics*, 115, 9657–9666.
- Henkelman, G., Jóhannesson, G., & Jonsson, H. (2000). *Methods for Finding Saddle Points and Minimum Energy Paths*. Kluwer Academic Publishers.
- Henkelman, G., Uberuaga, B., & Jonsson, H. (2000). A climbing image nudged elastic band method for finding saddle points and minimum energy paths. *Journal Of Chemical Physics*, 113, 9901–9904.
- Hirai, T., Pintsuk, G., Linke, J., & Batilliot, M. (2009). Cracking failure study of iter-reference tungsten grade under single pulse thermal shock loads at elevated temperatures. *Journal of Nuclear Materials*, 390–391, 751 – 754. Proceedings of the 18th International Conference on Plasma-Surface Interactions in Controlled Fusion Device Proceedings of the 18th International Conference on Plasma-Surface Interactions in Controlled Fusion Device.
- Hirth, J. P., & Lothe, J. (1982). *Theory of dislocations*. John Wiley & Sons.
- Hölscher, M., Raabe, D., & Lücke, K. (1991). Rolling and recrystallization textures of bcc steels. *Steel Research International*, (pp. 567–575).
- Hölscher, M., Raabe, D., & Lücke, K. (1994). Relationship between rolling textures and shear textures in fcc and bcc metals. *Acta metallurgica et materialia*, 42, 879–886.
- Honeycutt, J. D., & Andersen, H. C. (1987). Molecular dynamics study of melting and freezing of small lennard-jones clusters. *The Journal of Physical Chemistry*, 91, 4950–4963.
- Hull, D., & Bacon, D. J. (1984). *Introduction to dislocations* volume 257. Pergamon Press Oxford.
- Hull, D., Byron, J., & Noble, F. (1967). Orientation dependence of yield in body-centered cubic metals. *Canadian Journal of Physics*, 45, 1091–1099.

- Hutchinson, J. (1976). Bounds and self-consistent estimates for creep of polycrystalline materials. *Proceedings of the Royal Society of London. A. Mathematical and Physical Sciences*, 348, 101–127.
- Hutchinson, J., & Neale, K. (1977). Influence of strain-rate sensitivity on necking under uniaxial tension. *Acta Metallurgica*, 25, 839–846.
- Ismail-Beigi, S., & Arias, T. (2000). Ab initio study of screw dislocations in mo and ta: a new picture of plasticity in bcc transition metals. *Physical Review Letters*, 84, 1499.
- Ito, K., & Vitek, V. (2001). Atomistic study of non-schmid effects in the plastic yielding of bcc metals. *Philosophical Magazine A*, 81, 1387–1407.
- Juslin, N., Erhart, P., Träskelin, P., Nord, J., Henriksson, K. O., Nordlund, K., Salonen, E., & Albe, K. (2005). Analytical interatomic potential for modeling nonequilibrium processes in the w–c–h system. *Journal of applied physics*, 98, 123520.
- Keh, A. S. (1965). Work hardening and deformation sub-structure in iron single crystals deformed in tension at 298 k. *Philosophical Magazine*, 12, 9–30.
- Kitayama, K., Tomé, C., Rauch, E., Gracio, J., & Barlat, F. (2013). A crystallographic dislocation model for describing hardening of polycrystals during strain path changes. application to low carbon steels. *International Journal of Plasticity*, 46, 54–69.
- Knezevic, M., Beyerlein, I. J., Lovato, M. L., Tomé, C. N., Richards, A. W., & McCabe, R. J. (2014). A strain-rate and temperature dependent constitutive model for bcc metals incorporating non-schmid effects: Application to tantalum–tungsten alloys. *International Journal of Plasticity*, 62, 93–104.
- Knibbs, R. (1969). The measurement of thermal expansion coefficient of tungsten at elevated temperatures. *Journal of Physics E: Scientific Instruments*, 2, 515.
- Kocks, U., Argon, A., & Ashby, M. (1975). Progress in materials science. *Thermodynamics and Kinetics of Slip*, 19, 110–170.
- Koester, A., Ma, A., & Hartmaier, A. (2012). Atomistically informed crystal plasticity model for body-centered cubic iron. *Acta Materialia*, 60, 3894–3901.

- Komanduri, R., Chandrasekaran, N., & Raff, L. (2001). Molecular dynamics (md) simulation of uniaxial tension of some single-crystal cubic metals at nanolevel. *International Journal of Mechanical Sciences*, 43, 2237–2260.
- Kords, C., & Raabe, D. (2013). *On the role of dislocation transport in the constitutive description of crystal plasticity*. Ph.D. thesis Berlin.
- Kroner, E. (1961). On the plastic deformation of polycrystals. *acta metallurgica*, 9, 155–161.
- Kuchnicki, S., Radovitzky, R., & Cuitiño, A. (2008). An explicit formulation for multiscale modeling of bcc metals. *International Journal of Plasticity*, 24, 2173–2191.
- Kuramoto, E., Aono, Y., & Kitajima, K. (1979). Thermally activated slip deformation of high purity iron single crystals between 4.2 k and 300 k. *Scripta Metallurgica*, 13, 1039–1042.
- Lassner, E., & Schubert, W.-D. (1999). *Tungsten: Properties, Chemistry, Technology of the Element, Alloys, and Chemical Compounds..* Springer US.
- Lebensohn, R. (2001). N-site modeling of a 3d viscoplastic polycrystal using fast fourier transform. *Acta Materialia*, 49, 2723–2737.
- Lebensohn, R. A., Kanjarla, A. K., & Eisenlohr, P. (2012). An elasto-viscoplastic formulation based on fast fourier transforms for the prediction of micromechanical fields in polycrystalline materials. *International Journal of Plasticity*, 32, 59–69.
- Lee, Y. J., Subhash, G., & Ravichandran, G. (1999). Constitutive modeling of textured body-centered-cubic (bcc) polycrystals. *International Journal of Plasticity*, 15, 625–645.
- Li, H., Wurster, S., Motz, C., Romaner, L., Ambrosch-Draxl, C., & Pippan, R. (2012). Dislocation-core symmetry and slip planes in tungsten alloys: Ab initio calculations and microcantilever bending experiments. *Acta Materialia*, 60, 748–758.
- Li, Q., & Shi, S.-Q. (2002). Dislocation jumping over the sound barrier in tungsten. *Applied physics letters*, 80, 3069–3071.
- Lim, H., Battaile, C. C., Carroll, J. D., Boyce, B. L., & Weinberger, C. R. (2015a). A physically based model of temperature and strain rate dependent yield in bcc metals: Implementation into crystal plasticity. *Journal of the Mechanics and Physics of Solids*, 74, 80–96.

- Lim, H., Hale, L., Zimmerman, J., Battaile, C., & Weinberger, C. (2015b). A multi-scale model of dislocation plasticity in α -fe: Incorporating temperature, strain rate and non-schmid effects. *International Journal of Plasticity*, .
- Lim, H., Weinberger, C. R., Battaile, C. C., & Buchheit, T. E. (2013). Application of generalized non-schmid yield law to low-temperature plasticity in bcc transition metals. *Modelling and Simulation in Materials Science and Engineering*, 21, 045015.
- Lin, K., & Chrzan, D. (1999a). Kinetic monte carlo simulation of dislocation dynamics. *Physical Review B*, 60, 3799.
- Lin, K., & Chrzan, D. C. (1999b). Kinetic monte carlo simulation of dislocation dynamics. *Phys. Rev. B*, 60, 3799–3805.
- Lubliner, J. (2008). *Plasticity theory*. Courier Corporation.
- Ma, A., & Roters, F. (2004). A constitutive model for fcc single crystals based on dislocation densities and its application to uniaxial compression of aluminium single crystals. *Acta Materialia*, 52, 3603 – 3612.
- Ma, A., Roters, F., & Raabe, D. (2006). A dislocation density based constitutive model for crystal plasticity {FEM} including geometrically necessary dislocations. *Acta Materialia*, 54, 2169 – 2179.
- Ma, A., Roters, F., & Raabe, D. (2007). A dislocation density based constitutive law for {BCC} materials in crystal plasticity {FEM}. *Computational Materials Science*, 39, 91 – 95. Proceedings of the 15th International Workshop on Computational Mechanics of Materials The 15th International Workshop on Computational Mechanics of Materials.
- Madec, R., & Kubin, L. (2004). Dislocation interactions and symmetries in bcc crystals. In *IUTAM Symposium on Mesoscopic Dynamics of Fracture Process and Materials Strength* (pp. 69–78). Springer.
- Maisonnier, D., Campbell, D., Cook, I., Di Pace, L., Giancarli, L., Hayward, J., Puma, A. L., Medrano, M., Norajitra, P., Roccella, M. et al. (2007). Power plant conceptual studies in europe. *Nuclear Fusion*, 47, 1524.
- Marian, J., Cai, W., & Bulatov, V. V. (2004). Dynamic transitions from smooth to rough to twinning in dislocation motion. *Nature Materials*, 3, 158–163.

- Marichal, C., Van Swygenhoven, H., Van Petegem, S., & Borca, C. (2013). {110} slip with {112} slip traces in bcc tungsten. *Scientific reports*, 3.
- Marinica, M., Ventelon, L., Gilbert, M., Proville, L., Dudarev, S., Marian, J., Bencteux, G., & Willaime, F. (2013). Interatomic potentials for modelling radiation defects and dislocations in tungsten. *Journal of Physics: Condensed Matter*, 25, 395502.
- Moulinec, H., & Suquet, P. (1994). A fast numerical method for computing the linear and nonlinear mechanical properties of composites. *Comptes rendus de l'Académie des sciences. Série II, Mécanique, physique, chimie, astronomie*, 318, 1417–1423.
- Moulinec, H., & Suquet, P. (1998). A numerical method for computing the overall response of nonlinear composites with complex microstructure. *Computer methods in applied mechanics and engineering*, 157, 69–94.
- Mrovec, M., Gröger, R., Bailey, A. G., Nguyen-Manh, D., Elsässer, C., & Vitek, V. (2007). Bond-order potential for simulations of extended defects in tungsten. *Physical Review B*, 75, 104119.
- Mrovec, M., Nguyen-Manh, D., Elsässer, C., & Gumbsch, P. (2011). Magnetic bond-order potential for iron. *Physical review letters*, 106, 246402.
- Nakano, A. (2008). A space-time-ensemble parallel nudged elastic band algorithm for molecular kinetics simulation. *Computer Physics Communications*, 178, 280–289.
- Narayanan, S., McDowell, D. L., & Zhu, T. (2014a). Crystal plasticity model for {BCC} iron atomistically informed by kinetics of correlated kinkpair nucleation on screw dislocation. *Journal of the Mechanics and Physics of Solids*, 65, 54 – 68.
- Narayanan, S., McDowell, D. L., & Zhu, T. (2014b). Crystal plasticity model for {BCC} iron atomistically informed by kinetics of correlated kinkpair nucleation on screw dislocation. *Journal of the Mechanics and Physics of Solids*, 65, 54 – 68.
- Neumann, F. E., & Meyer, O. E. (1885). *Vorlesungen über die Theorie der Elastizität der festen Körper und des Lichtäthers: gehalten an der Universität Königsberg* volume 5. BG Teubner.
- Norajitra, P., Abdel-Khalik, S. I., Giancarli, L. M., Ihli, T., Janeschitz, G., Malang, S., Mazul, I. V., & Sardain, P. (2008). Divertor conceptual designs for a fusion power plant. *Fusion Engineering and Design*, 83, 893–902.

- Olmsted, D. L., Hector Jr, L. G., Curtin, W., & Clifton, R. (2005). Atomistic simulations of dislocation mobility in al, ni and al/mg alloys. *Modelling and Simulation in Materials Science and Engineering*, 13, 371.
- Orowan, E. (1934a). Zur kristallplastizität. i. *Zeitschrift für Physik*, 89, 605–613.
- Orowan, E. (1934b). Zur kristallplastizität. ii. *Zeitschrift für Physik*, 89, 614–633.
- Orowan, E. (1934c). Zur kristallplastizität. iii. *Zeitschrift für Physik*, 89, 634–659.
- Orowan, E. (1940). Problems of plastic gliding. *Proceedings of the Physical Society*, 52, 8.
- Orowan, E. (1944). Discussion on the significance of tensile and other mechanical test properties of metals. In *Proceedings of the Institute of Mechanical Engineers* (pp. 131–146). volume 151.
- Pamela, J., Bécoulet, A., Borba, D., Boutard, J.-L., Horton, L., & Maisonnier, D. (2009). Efficiency and availability driven r&d issues for demo. *Fusion Engineering and Design*, 84, 194–204.
- Park, H., Fellinger, M. R., Lenosky, T. J., Tipton, W. W., Trinkle, D. R., Rudin, S. P., Woodward, C., Wilkins, J. W., & Hennig, R. G. (2012). Ab initio based empirical potential used to study the mechanical properties of molybdenum. *Physical Review B*, 85, 214121.
- Patra, A., Zhu, T., & McDowell, D. L. (2014). Constitutive equations for modeling non-schmid effects in single crystal bcc-fe at low and ambient temperatures. *International Journal of Plasticity*, 59, 1 – 14.
- Peeters, B., Kalidindi, S., Van Houtte, P., & Aernoudt, E. (2000). A crystal plasticity based work-hardening/softening model for bcc metals under changing strain paths. *Acta materialia*, 48, 2123–2133.
- Peirce, D., Asaro, R., & Needleman, A. (1982). An analysis of nonuniform and localized deformation in ductile single crystals. *Acta metallurgica*, 30, 1087–1119.
- Peirce, D., Asaro, R. J., & Needleman, A. (1983). Material rate dependence and localized deformation in crystalline solids. *Acta metallurgica*, 31, 1951–1976.
- Pichl, W. (2002). Slip geometry and plastic anisotropy of body-centered cubic metals. *physica status solidi (a)*, 189, 5–25.

- Plimpton, S. (1995). Fast parallel algorithms for short-range molecular dynamics. *Journal of computational physics*, 117, 1–19.
- Polanyi, M. (1934). Über eine art gitterstörung, die einen kristall plastisch machen könnte. *Zeitschrift für Physik*, 89, 660–664.
- Prager, W. (1952). The general theory of limit design. In *Proceedings of the 8th International Congress on theoretical and Applied Mechanics, Istanbul* (pp. 65–72). volume 19.
- Proville, L., Rodney, D., & Marinica, M.-C. (2012). Quantum effect on thermally activated glide of dislocations. *Nature materials*, 11, 845–849.
- Proville, L., Ventelon, L., & Rodney, D. (2013). Prediction of the kink-pair formation enthalpy on screw dislocations in α -iron by a line tension model parametrized on empirical potentials and first-principles calculations. *Physical Review B*, 87.
- Qin, Q., & Bassani, J. L. (1992). Non-schmid yield behavior in single crystals. *Journal of the Mechanics and Physics of Solids*, 40, 813 – 833.
- Queyreau, S., Marian, J., Gilbert, M., & Wirth, B. (2011). Edge dislocation mobilities in bcc fe obtained by molecular dynamics. *Physical Review B*, 84, 064106.
- Queyreau, S., Monnet, G., & Devincre, B. (2009). Slip systems interactions in α -iron determined by dislocation dynamics simulations. *International Journal of Plasticity*, 25, 361 – 377.
- Raabe, D. (1995a). Investigation of contribution of {123} slip planes to development of rolling textures in bee metals by use of taylor models. *Materials science and technology*, 11, 455–460.
- Raabe, D. (1995b). Simulation of rolling textures of bcc metals considering grain interactions and crystallographic slip on {110}, {112} and {123} planes. *Materials Science and Engineering: A*, 197, 31–37.
- Raabe, D., Schlenkert, G., Weisshaupt, H., & Lücke, K. (1994). Texture and microstructure of rolled and annealed tantalum. *Materials science and technology*, 10, 299–305.
- Raffo, P. L. (1969). Yielding and fracture in tungsten and tungsten-rhenium alloys. *Journal of the Less Common Metals*, 17, 133–149.
- Raphanel, J., & Van Houtte, P. (1985). Simulation of the rolling textures of bcc metals by means of the relaxed taylor theory. *Acta Metallurgica*, 33, 1481–1488.

- Reina, C., & Conti, S. (2014). Kinematic description of crystal plasticity in the finite kinematic framework: A micromechanical understanding of $F=FeFp$. *Journal of the Mechanics and Physics of Solids*, 67, 40–61.
- Rice, J. (1971). Inelastic constitutive relations for solids: An internal-variable theory and its application to metal plasticity. *Journal of the Mechanics and Physics of Solids*, 19, 433–455.
- Rieth, M., Boutard, J., Dudarev, S., Ahlgren, T., Antusch, S., Baluc, N., Barthe, M.-F., Becquart, C., Ciupinski, L., Correia, J. et al. (2011). Review on the efda programme on tungsten materials technology and science. *Journal of Nuclear Materials*, 417, 463–467.
- Rieth, M., Dudarev, S., De Vicente, S. G., Aktaa, J., Ahlgren, T., Antusch, S., Armstrong, D., Balden, M., Baluc, N., Barthe, M.-F. et al. (2013a). Recent progress in research on tungsten materials for nuclear fusion applications in europe. *Journal of Nuclear Materials*, 432, 482–500.
- Rieth, M., Dudarev, S., de Vicente, S. G., Aktaa, J., Ahlgren, T., Antusch, S., Armstrong, D., Balden, M., Baluc, N., Barthe, M.-F. et al. (2013b). A brief summary of the progress on the efda tungsten materials program. *Journal of Nuclear Materials*, 442, S173–S180.
- Rodney, D., & Proville, L. (2009). Stress-dependent peierls potential: Influence on kink-pair activation. *Physical Review B*, 79, 094108.
- Romaner, L., Ambrosch-Draxl, C., & Pippan, R. (2010). Effect of rhenium on the dislocation core structure in tungsten. *Physical review letters*, 104, 195503.
- Roters, F. (2011). *Advanced material models for the crystal plasticity finite element method: development of a general CPFEM framework*. Universitätsbibliothek.
- Roters, F., Eisenlohr, P., Bieler, T. R., & Raabe, D. (2011). *Crystal Plasticity Finite Element Methods: In Materials Science and Engineering*. John Wiley & Sons.
- Roters, F., Eisenlohr, P., Hantcherli, L., Tjahjanto, D., Bieler, T., & Raabe, D. (2010). Overview of constitutive laws, kinematics, homogenization and multiscale methods in crystal plasticity finite-element modeling: Theory, experiments, applications. *Acta Materialia*, 58, 1152–1211.

- Roters, F., Eisenlohr, P., Kords, C., Tjahjanto, D., Diehl, M., & Raabe, D. (2012). DAMASK: the Dusseldorf Advanced MAterial Simulation Kit for studying crystal plasticity using an FE based or a spectral numerical solver. *Procedia IUTAM*, 3, 3 – 10. IUTAM Symposium on Linking Scales in Computations: From Microstructure to Macro-scale Properties.
- Roth, J., Tsitrone, E., Loarte, A., Loarer, T., Counsell, G., Neu, R., Philipps, V., Brezinsek, S., Lehnert, M., Coad, P. et al. (2009). Recent analysis of key plasma wall interactions issues for iter. *Journal of Nuclear Materials*, 390, 1–9.
- Sachs, G. (1928). Zur ableitung einer fließbedingung. *Verein Deutscher Ingenieure*, 72, 734–736.
- Samolyuk, G. D., Ossetsky, Y., & Stoller, R. (2013). The influence of transition metal solutes on the dislocation core structure and values of the peierls stress and barrier in tungsten. *Journal of Physics: Condensed Matter*, 25, 025403.
- Scarle, S., Ewels, C., Heggie, M., & Martsinovich, N. (2004). Linewise kinetic monte carlo study of silicon dislocation dynamics. *Physical Review B*, 69, 075209.
- Schadler, H. (1964). Mobility of edge dislocations on {110} planes in tungsten single crystals. *Acta metallurgica*, 12, 861–870.
- Schmid, E., & Boas, W. (1935). *Kristallplastizität: mit besonderer Berücksichtigung der Metalle* volume 17. J. Springer.
- Schmid, E., & Boas, W. (1950). Plasticity of crystals, . W. Kristallplastizität., Springer, Berlin (1935), translated in English.
- Schmid, E., Boas, W., & Rawlins, F. (1935). Kristallplastizität. *The Journal of Physical Chemistry*, 39, 1248–1248.
- Seeger, A. (1981). The temperature and strain-rate dependence of the flow stress of body-centred cubic metals: A theory based on kink–kink interactions. *Zeitschrift fur Metallkunde*, 72, 369–380.
- Sestak, B., & Seeger, A. (1978). Slip and work hardening in bcc metals and alloys - 1. [gleitung und verfestigung in kubisch-raumzentrierten metallen und legierungen - 1.]. *Zeitschrift fuer Metallkunde/Materials Research and Advanced Techniques*, 69, 195–202.

- Šesták, B., & Zárubová, N. (1965). Asymmetry of slip in fe-si alloy single crystals. *physica status solidi (b)*, 10, 239–250.
- Sethian, J., Colombant, D., Giuliani, J., Lehmberg, R., Myers, M., Obenschain, S., Schmitt, A., Weaver, J., Wolford, M., Hegeler, F. et al. (2010). The science and technologies for fusion energy with lasers and direct-drive targets. *Plasma Science, IEEE Transactions on*, 38, 690–703.
- Sethian, J. D., Raffray, A. R., Latkowski, J., Blanchard, J. P., Snead, L., Renk, T. J., & Sharafat, S. (2005). An overview of the development of the first wall and other principal components of a laser fusion power plant. *Journal of Nuclear Materials*, 347, 161 – 177. Laser Fusion Materials.
- Shantrag, P., Eisenlohr, P., Diehl, M., & Roters, F. (2014). Numerically robust spectral methods for crystal plasticity simulations of heterogeneous materials. *International Journal of Plasticity*, .
- Sherwood, P., Guiu, F., Kim, H.-C., & Pratt, P. L. (1967). Plastic anisotropy of tantalum, niobium, and molybdenum. *Canadian Journal of Physics*, 45, 1075–1089.
- Spitzig, W., & Keh, A. (1970). The effect of orientation and temperature on the plastic flow properties of iron single crystals. *Acta Metallurgica*, 18, 611 – 622.
- Stainier, L., Cuitiño, A. M., & Ortiz, M. (2002). A micromechanical model of hardening, rate sensitivity and thermal softening in bcc single crystals. *Journal of the Mechanics and Physics of Solids*, 50, 1511–1545.
- Stephens, J. R. (1970). Dislocation structures in single-crystal tungsten and tungsten alloys. *Metallurgical and Materials Transactions*, 1, 1293–1301.
- Stukowski, A. (2010). Visualization and analysis of atomistic simulation data with OVITO-the Open Visualization Tool. *MODELLING AND SIMULATION IN MATERIALS SCIENCE AND ENGINEERING*, 18.
- Stukowski, A., Cereceda, D., Swinburne, T. D., & Marian, J. (2015). Thermally-activated non-schmid glide of screw dislocations in w using atomistically-informed kinetic monte carlo simulations. *International Journal of Plasticity*, 65, 108–130.
- Tadmor, E. B., & Miller, R. E. (2011). *Modeling Materials, Atomistic and Multiscale Techniques*. Cambridge University Press.

- Takeuchi, S., Furubayashi, E., & Taoka, T. (1967). Orientation dependence of yield stress in 4.4% silicon iron single crystals. *Acta metallurgica*, 15, 1179–1191.
- Tang, M., & Marian, J. (2014). Temperature and high strain rate dependence of tensile deformation behavior in single-crystal iron from dislocation dynamics simulations. *Acta Materialia*, 70, 123–129.
- Tarleton, E., & Roberts, S. G. (2009). Dislocation dynamic modelling of the brittle–ductile transition in tungsten. *Philosophical Magazine*, 89, 2759–2769.
- Taylor, G. (1928). The deformation of crystals of β -brass. *Proceedings of the Royal Society of London. Series A*, 118, 1–24.
- Taylor, G. (1934a). The mechanism of plastic deformation of crystals. part ii. comparison with observations. *Proceedings of the Royal Society of London. Series A, Containing Papers of a Mathematical and Physical Character*, (pp. 388–404).
- Taylor, G. (1938). Plastic strain in metals. *Journal of the Institute of Metals*, 62, 307–324.
- Taylor, G. (1992). Thermally-activated deformation of bcc metals and alloys. *Progress in materials science*, 36, 29–61.
- Taylor, G. I. (1934b). The mechanism of plastic deformation of crystals. part i. theoretical. *Proceedings of the Royal Society of London. Series A, Containing Papers of a Mathematical and Physical Character*, (pp. 362–387).
- Terentyev, D. (2006). Study of radiation effects in fecr alloys for fusion applications using computer simulations. *183 University of Uppsala. PhD Thesis*, .
- Tian, X., & Woo, C. (2004). The movement of screw dislocations in tungsten. *Materials Science and Engineering: A*, 369, 210–214.
- Tsuzuki, H., Branicio, P. S., & Rino, J. P. (2007). Structural characterization of deformed crystals by analysis of common atomic neighborhood. *Computer Physics Communications*, 177, 518 – 523.
- Van Petegem, S., Van Swygenhoven, H., Borca, C., Marichal, C. et al. (2013). {110} slip with {112} slip traces in bcc tungsten. *Scientific Reports*, 3.
- Ventelon, L., & Willaime, F. (2007). Core structure and peierls potential of screw dislocations in α -fe from first principles: cluster versus dipole approaches. *Journal of Computer-Aided Materials Design*, 14, 85–94.

- Ventelon, L., Willaime, F., Clouet, E., & Rodney, D. (2013). Ab initio investigation of the peierls potential of screw dislocations in bcc fe and w. *Acta Materialia*, 61, 3973–3985.
- Ventelon, L., Willaime, F., & Leyronnas, P. (2009). Atomistic simulation of single kinks of screw dislocations in α -fe. *Journal of Nuclear Materials*, 386-388, 26–29.
- Vitek, V. (2004a). Core structure of screw dislocations in body-centred cubic metals: Relation to symmetry and interatomic bonding. *Philosophical Magazine*, 84, 415–428.
- Vitek, V. (2004b). Core structure of screw dislocations in body-centred cubic metals: relation to symmetry and interatomic bonding. *Philosophical Magazine*, 84, 415–428.
- Vitek, V., Perrin, R., & Bowen, D. (1970). The core structure of $1/2$ (111) screw dislocations in bcc crystals. *Philosophical Magazine*, 21, 1049–1073.
- Vitek, V., & Yamaguchi, M. (1973). Core structure of nonscrew $1/2$ (111) dislocations on (110) planes in bcc crystals. ii. peierls stress and the effect of an external shear stress on the cores. *Journal of Physics F: Metal Physics*, 3, 537.
- W. Cai, J.-P. C. J. L., V.V. Bulatov, & Yip, S. (2002). *Dislocation core effects on mobility in: Dislocation in Solids*. Elsevier.
- Weinberger, C. R., Battaile, C. C., Buchheit, T. E., & Holm, E. A. (2012). Incorporating atomistic data of lattice friction into bcc crystal plasticity models. *International Journal of Plasticity*, 37, 16–30.
- Weinberger, C. R., Tucker, G. J., & Foiles, S. M. (2013). Peierls potential of screw dislocations in bcc transition metals: Predictions from density functional theory. *PHYSICAL REVIEW B*, 87.
- Weinberger, C. R., Tucker, G. J., & Foiles, S. M. (2013). Peierls potential of screw dislocations in bcc transition metals: Predictions from density functional theory. *Physical Review B*, 87, 054114.
- Wittlich, K., Hirai, T., Compan, J., Klimov, N., Linke, J., Loarte, A., Merola, M., Pintsuk, G., Podkovyrov, V., Singheiser, L. et al. (2009). Damage structure in divertor armor materials exposed to multiple iter relevant elm loads. *Fusion Engineering and Design*, 84, 1982–1986.

- Woodward, C., & Rao, S. (2001). Ab-initio simulation of isolated screw dislocations in bcc mo and ta. *Philosophical Magazine A*, 81, 1305–1316.
- Wurster, S., Baluc, N., Battabyal, M., Crosby, T., Du, J., García-Rosales, C., Hasegawa, A., Hoffmann, A., Kimura, A., Kurishita, H. et al. (2013). Recent progress in r&d on tungsten alloys for divertor structural and plasma facing materials. *Journal of Nuclear Materials*, 442, S181–S189.
- Wurster, S., Gludovatz, B., & Pippan, R. (2010). High temperature fracture experiments on tungsten–rhenium alloys. *International Journal of Refractory Metals and Hard Materials*, 28, 692–697.
- Yalcinkaya, T., Brekelmans, W., & Geers, M. (2008). Bcc single crystal plasticity modeling and its experimental identification. *Modelling and Simulation in Materials Science and Engineering*, 16, 085007.
- Yang, L., Söderlind, P., & Moriarty, J. A. (2001). Accurate atomistic simulation of $(a/2)\langle 111 \rangle_c$ screw dislocations and other defects in bcc tantalum. *Philosophical Magazine A*, 81, 1355–1385.
- Zhou, X., Wadley, H., Johnson, R. A., Larson, D., Tabat, N., Cerezo, A., Petford-Long, A., Smith, G., Clifton, P., Martens, R. et al. (2001). Atomic scale structure of sputtered metal multilayers. *Acta materialia*, 49, 4005–4015.
- Zinkle, S. J., & Ghoniem, N. M. (2011). Prospects for accelerated development of high performance structural materials. *Journal of Nuclear Materials*, 417, 2–8.
- Zwiesele, S., & Diehl, J. (1979). Temperature and strain rate dependence of the macro-yield stress of high-purity iron single crystals. *Strength of Metals and Alloys*, 1, 59–64.

